PHOTON CONTROL IN NANO-STRUCTURED ORGANIC PHOTOVOLTAIC MATERIALS

RAFAEL BETANCUR

under the supervision of

PROFESSOR JORDI MARTORELL

submitted this thesis in partial fulfillment

of the requirements for the degree of

DOCTOR

by the

UNIVERSITAT POLITÉCNICA DE CATALUNYA

BARCELONA, 2013

To my family

Acknowledgements

Being at ICFO has allowed me to accomplish one of my dreams and I would like to thank all the people who contributed me during my PhD stay.

I wish above all to thank the ICFO administrative, technical and logistic personnel for giving me the opportunity of being part of this wonderful institute and allowed me to make my PhD a great personal experience.

I am truly indebted and thankful to Profesor Jordi Martorell for guiding my work as well as all the organic nanostructured photovoltaics team (Luis, Luat, David, Camila, Pablo, Alberto, Francisco, Francesco, Can, Roberto, Xavier, Marc, Marina and Paola) from whom I have learnt all that I know related to photovoltaics. Additionally, to the researchers I have had the opportunity to cooperate with (Professor Pruneri, Dhriti, Toni, Professor Quidant, Jan, Professor Míguez, Silvia, Professor Aernouts and David).

Finally, I am grateful to all the nice and amazing people that I have met in ICFO. Thanks a lot for being so warm and giving me so many good times and laughs. To my family, my girlfriend and Esneda, thank you very much for your permanent and unconditional help, and God for being always present.

Abstract

Organic photovoltaic (OPV) technology has emerged as a potential cost-effective solution to produce electrical energy. The foreseen low manufacturing costs combined with features as semi-transparency or mechanical flexibility give to OPV devices a strong potential for industrial applicability. However, the commercial implementation of this technology faces the challenge of increasing the relatively low power conversion efficiency of the current state-of-the-art OPV devices. This thesis presents an optical based approach to enhance the performance of OPV devices by effectively controlling sunlight photons. Such control is possible because of the coherent interaction between light and the multilayered structure constituting the OPV device.

Accordingly, we studied the dependence of the optical field distribution inside the solar cell relative to the optical properties of the different layers including their refractive index n, extinction coefficient k, and thickness. This optical study led to the prediction of optimal OPV device structures. The first implementation of a photon control was done by changing the relative thicknesses of the different layers in the device. An optimal combination of thicknesses was found and confirmed experimentally. A significant reduction of the energy lost in the device was demonstrated. As a consequence, the photon harvesting improved, which led to a close matching between the external and internal quantum efficiencies in a broad wavelength range. A second photon control strategy to enhance the performance of OPV cells was implemented by modifying the complex refractive index of the non-active device layers. Both n and k were changed in specific layers by considering new materials. Three different cases were considered: in the first example a BCP layer was

used to replace calcium as electron transporting layer. The parasitic absorption induced by the highly absorptive calcium layer was diminished almost to zero after replacing this layer with BCP, a material whose extinction coefficient is null for a broad wavelength range. A 19% performance enhancement was demonstrated. In the second example, an ultrathin nickel oxide layer was used to replace the commonly used PEDOT layer as hole transporting layer. Very thin layers of nickel oxide could be used for a better photon distribution and harvesting in the photoactive layer. In the last case, a metallic cupper/nickel semi-transparent electrode was used to replace an ITO electrode. This new metallic electrode in combination with the back aluminum electrode enabled the formation of an optical cavity which resulted in a stronger localization of the field in the active layer.

Finally, several of the concepts considered above to effectively localize the field in the active layer were used in conjunction with a photonic structure integrated in the OPV architecture to achieve an optically optimized semi-transparent OPV device. In particular, a one-dimensional non-periodic photonic crystal was designed and added to a semi-transparent OPV device in order to re-harvest UV and IR photons while keeping a high transmission for the visible photons. A power conversion efficiency enhancement larger than 56% was achieved while maintaining the device luminosity around 30%. An additional feature of the integration of such photonic crystal was the possibility of tuning the color transmitted by the device which was also demonstrated.

In summary, in this thesis we demonstrate experimentally and theoretically that optics plays a very relevant role for enhancing the power conversion efficiency of OPV devices. The methods presented are perfectly compatible with a more oriented material science approach to achieve the final objective of obtaining a performance-competitive OPV technology.

Resumen

La tecnología fotovoltaica orgánica (OPV) ha surgido como una solución potencial rentable para producir energía eléctrica. Los bajos costos de manufactura previstos combinados con propiedades como semi-transparencia o flexibilidad mecánica le dan a los dispositivos OPV un gran potencial de ser aplicados industrialmente. Sin embargo, la implementación comercial de esta tecnología se enfrenta al reto de incrementar la relativamente baja eficiencia de los dispositivos OPV del estado del arte. Esta tesis presenta una aproximación óptica para aumentar la eficiencia de los dispositivos OPV mediante un control efectivo de los fotones de la radiación solar. Tal control es posible debido a la interacción coherente entre la luz y la estructura de multi-capas que constituye el dispositivo OPV.

Consecuentemente, en esta tesis se estudia la dependencia de la distribución del campo óptico dentro de la celda solar con las propiedades ópticas de las diferentes capas. Entre esas propiedades se incluyen el índice de refracción n, el coeficiente de extinción k y espesor de cada una de las capas. Este estudio óptico ha permitido predecir estructuras óptimas para los dispositivos OPV. La primera implementación del control de fotones fue hecha al cambiar los espesores relativos de las diferentes capas en el dispositivo. Una combinación óptima fue encontrada y confirmada experimentalmente. Una reducción significativa de la energía perdida por reflexión especular fue demostrada y como consecuencia, la recolección de fotones fue mejorada lo cual condujo a la concordancia entre las eficiencias cuánticas externa e internas en un amplio rango de longitudes de onda. Una segunda estrategia de control de fotones para mejorar el desempeño de los dispositivos OPV fue implementada tras modificar las propiedades ópticas de las capas en el dispositivo distintas a la capa activa. Tanto n como k fueron cambiados en capas específicas tras considerar nuevos

materiales. Tres casos diferentes fueron considerados: en el primer caso, una capa de BCP fue usada para reemplazar el calcio como capa transportadora de electrones. La absorción parásita inducida por el elvevado coeficiente de extinción de la capa de calcio fue reducida casi hasta cero tras reemplazar esta capa con una de BCP, un material cuyo coeficiente de absorción es prácticamente cero para un amplio rango de longitudes de onda. Se demostró un aumento en el desempeño de los dispositivos de hasta el 19%. En el segundo ejemplo, una capa ultra-delgada de óxido de níquel fue usada para reemplazar la comúnmente empelada capa de PEDOT como capa transportadora de huecos. Estas capas de óxido de níquel permitieron una mejor distribución y recolección de fotones en la capa foto-activa. En el último caso, un electrodo semi-transparente hecho de cobre/níquel fue usado para reemplazar un electrodo de ITO. Este nuevo electrodo metálico en combinación con el electrodo de aluminio posterior del dispositivo permitió la formación de una cavidad óptica la cual resultó en una mayor localización del campo en la capa activa.

Finalmente, varios de los conceptos considerados anteriormente para localizar efectivamente el campo en la capa activa fueron usados en combinación con una estructura fotónica integrada en la estructura para obtener un dispositivo OPV semi-transparente ópticamente optimizado. Concretamente, un cristal fotónico uno-dimensional no-periódico fue diseñado y añadido al dispositivo OPV semi-trasparente con la intención de recolectar fotones UV e IR y al tiempo manteniendo una alta transmisión de los fotones visibles. Una mejora en el desempeño de los dispositivos superior al 56% fue obtenida preservando la luminosidad del dispositivo alrededor del 30%. Una propiedad adicional aportada por la integración de tales cristales fotónicos fue la posibilidad de modular el color transmitido por el dispositivo lo cual fue también demostrado.

En síntesis, en esta tesis se demostró experimental y teóricamente que la óptica juega un papel relevante para aumentar la eficiencia de los dispositivos OPV. Los métodos presentados son perfectamente compatibles con la aproximación que se realiza desde la perspectiva de la ciencia de los materiales al objetivo final de obtener una tecnología OPV competitiva.

Academic production

Publications

1. **R. Betancur**, P. Romero-Gomez, A. Martínez-Otero, X. Elias, M. Maymo, J. Martorell. *Near infrared light trapping in a layered photonic architecture for high performance transparent polymer solar cells.* Under review in Nature Photonics (2013).
2. A. Martínez-Otero, X. Elias, **R. Betancur**, J Martorell. *High Performance Polymer Solar Cells Using an Optically Enhanced Architecture.* Adv. Opt. Mat. 1, 1, 37-42 (2013).
3. **R. Betancur**, A. Martínez-Otero, P. Romero, S. Colodrero, H Mìguez, J. Martorell. *Optical interference for the matching of the External and Internal quantum efficiencies in Organic Photovoltaic cells.* Sol. Energy Mat. Sol. Cells 104 87-91 (2012).
4. T.L. Chen, **R. Betancur**, D. S. Ghosh, Jordi Martorell and V. Pruneri. *Efficient polymer solar cell employing an oxidized Ni capped Al:ZnO anode without the need of additional hole-transporting-layer.* Appl. Phys. Lett. **100**, 013310 (2012).
5. D.S. Ghosh, **R. Betancur**, T.L. Chen, V. Pruneri, Jordi Martorell. *Semi-transparent metal electrode of Cu–Ni as a replacement of an ITO in organic photovoltaic cells.* Sol. Energy Mat. Sol. Cells, Volume 95, Issue 4, 1228-1231 (2011).
6. **R. Betancur,** M. Maymó, X. Elias, L. T. Vuong, and J. Martorell**, *S**puttered NiO as electron blocking layer in P3HT:PCBM solar cells fabricated in ambient air*.** Sol. Energy Mat. Sol. Cells. Volume 95, Issue 2, 735-739 (2011).

7. L.T. Vuong, G. Kozyreff, **R. Betancur**, and Jordi Martorell, *Cavity-controlled radiative recombination of excitons in thin-film solar cells.* App. Phys. Lett. **95**, 233106 (2009).

Patents

1. J. Martorell, **R. Betancur**, P. Romero-Gómez, A. Martinez-Otero. Photoconversion semi-transparent device. In preparation (2013).
2. J. Martorell, **R. Betancur**, P. Romero-Gómez, L.T. Vuong. *Photoconversion device with enhanced photon absorption*. US Patent Application 13/358,687 (2012).

Contents

Acknowledgements ix
Abstract xi
Resumen xiii
Academic production xv
Contents xvii

1. Introduction 19
    1.1 Solar energy and organic solar cells 19
    1.2 Basics of the organic solar cells 22
    1.3 Sunlight harvesting 28
    1.3 Thesis summary 33

2. Sunlight localization by tuning of the device architecture 35
    2.1 Device multilayer stack optimization 36
    2.2 EQE and IQE matching 39
    2.3 Conclusions 44

3. The optical role of the non-active layers in an OPV cell 47
    3.1 Optical role of the electron transporting layer 48
    3.2 Optical role of the hole transporting layer 57
    3.3 Optical metal cavity in the OPV architecture 61
    3.4 Conclusions 65

4. Photonic control in semitransparent OPV devices 67

4.1 One-dimensional photonic structure integration 69
4.2 Color tunable organic photovoltaic devices 75
4.3 Conclusions 78

Conclusions 81

Appendix A. Materials and methods 83
A.1 Deposition methods 83
A.2 Materials 85
A.2.1 Active materials 85
A.2.2 Buffer layers 93
A.2.3 Electrodes 102
A.2.4 Other materials 109

Appendix B. Transparency and Color transmitted by a STOPV device 111
B.1 Luminosity 111
B.2 Estimation of the transmitted color 112

References 115

Chapter 1

Introduction

This chapter provides an overview of the state of the art of the organic photovoltaic technology in the framework of the need for renewable energy sources. Initially, a synopsis of the world energy consumption is presented making it apparent the current strong dependence on fossil fuels. Afterwards, different renewable energy sources are briefly reviewed with a particular attention given to solar power and more specifically to the potential and challenges for the organic photovoltaic (OPV) technology. The physical mechanisms of the organic photovoltaic devices and the most commonly used materials and characterization methods are described. Finally, a summary of the techniques employed to enhance the power conversion efficiency is discussed with special emphasis on the methods employed on this thesis which focuses on optically enhancing the performance for OPV devices.

1.1 Global energy consumption and solar energy

In 2012, the world energy consumption kept growing at a historical average rate of 2.5% arriving up to 12.275 Mtoe[i] [1]. A 33.1% of this energy came from oil, 30.3% from coal, 23.7% from natural gas, 4.9% from nuclear power, 6.4% from hydropower

[i] Million tons of oil equivalent. 1 Mtoe=4.187×10^{16} J = 1.163×10^{10} kWh

and 1.6% from other renewable sources. This outlook makes apparent the strong dependence on fossil fuels which carries the consequent environment impact because of CO_2 emissions that contribute to global warming. To minimize the impact on the environment from the global energy use, the development of sustainable renewable energy sources has been considered a priority by many governments.

The most widely used renewable energy source is hydropower. Last year from the total global energy consumption, 6.4% came from hydropower [1]. Its potential production of energy per year has been estimated around 1194 Mtoe [2]. However, this energy largely depends on the local natural resources and that makes it a very limited source for many countries. The region that employs this kind of energy at the largest scale is Latin America where 26% of the total energy consumption is supplied by hydropower [1]. On the other hand, this technology carries along some negative impact on the environment mostly because of the need to build dikes which imply deforestation. The other renewable energy sources, that is, solar, wind, geothermal and biomass last year provided 1.6% of the total global energy consumption [1]. A very positive fact during 2011 was that the entire renewable energy sector experienced a 17.7% annual growth rate, which was the largest one, followed by a 5.4% of the non-renewable energy based on coal. All these different alternative energy sources have an enormous potential for generation which has been estimated in 14.330 Mtoe for wind, 11.942 Mtoe for geothermal, 5.972 Mtoe for biomass and 38.215 Mtoe for solar per year [2].

Solar power is one of the most promising renewable energy sources and at the same time is one of the least exploited. As indicated above, this kind of energy alone has the potential to produce 38.215 Mtoe [2] per year, which is more than three times the global energy consumption in 2011. Additionally, its production and distribution is environmentally friendly. According to the figure 1.1 presented by the national renewable energy laboratory [3], the most efficient solar device to date exhibits a power conversion efficiency (PCE) of 44.0%. Such cell is based on a complex structure including several junctions and concentrators. On the other hand, from the emerging photovoltaic technologies, the top efficiency obtained for an organic

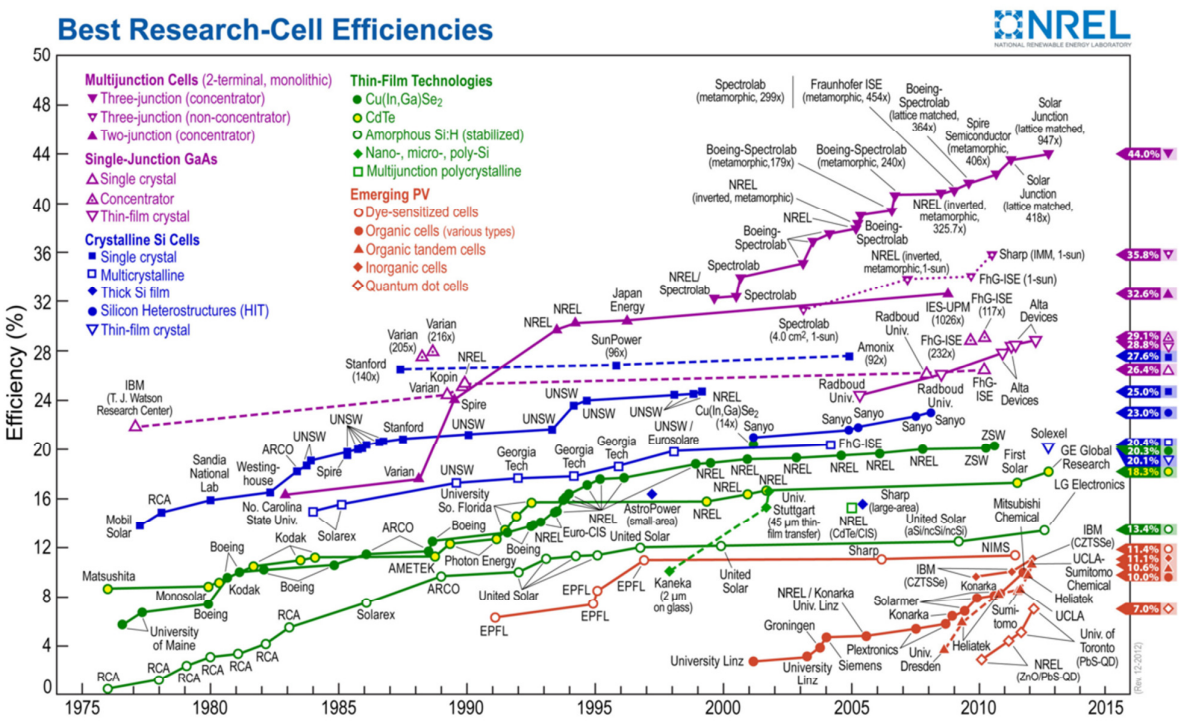

Figure 1.1 Best solar devices certified by NREL [3]

(tandem) solar cell is at 10.6%. This performance has shown a 16% average growing rate every year.

Organic solar devices have intrinsic features that make them very suitable for consumer electronic applications [4] and building-integrated photovoltaics (BIPV) [5]. These features include a high mechanical flexibility which is inherent to most polymers, the possibility of making the devices semi-transparent in the visible spectrum and light weight since a typical device has a total thickness less than 500nm. Additionally, low production costs are envisaged since manufacturing can be based on standard industrial printing processes [6]. This feature increases the potential applicability of the organic photovoltaic technology.

In the short/mid-term, the potential use of the organic solar devices includes off-grid applications like consumer electronics [7]; stand-alone systems for refrigeration or lightning in locations not connected to the grid [8]. In the long-term urban

architectonical applications, for instance BIPV [5], and in general on-grid applications for power generation in residential and industrial buildings are also foreseen.

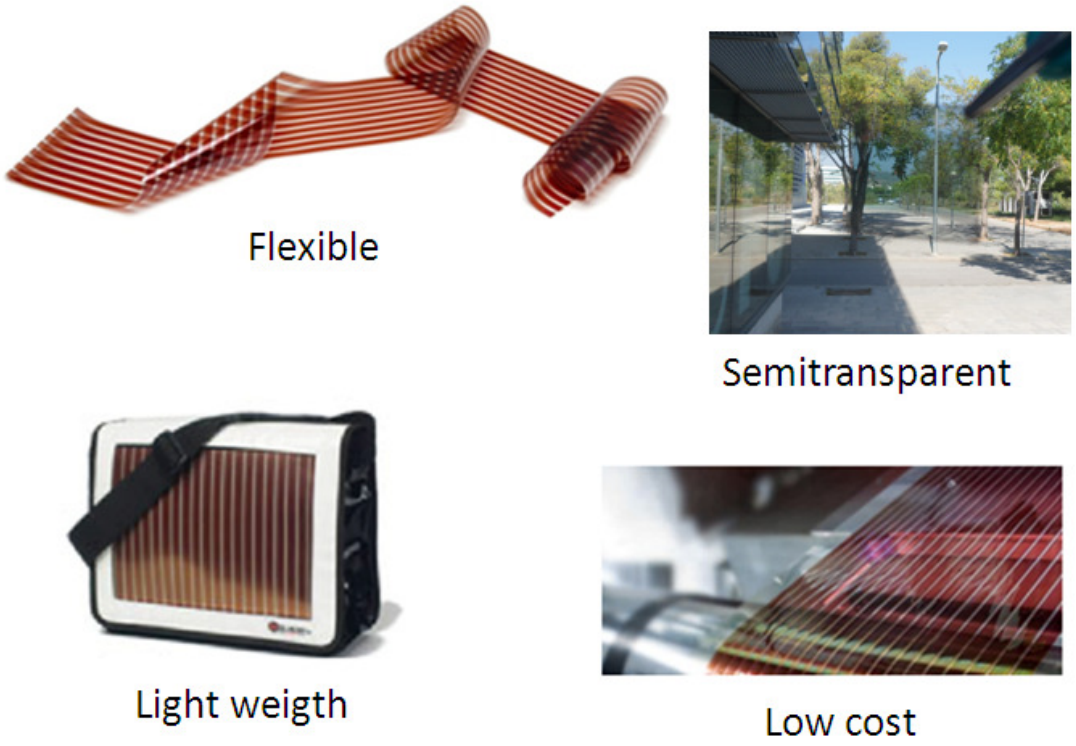

Figure 1.2. Special features of the organic solar devices

1.2 Basics of the organic solar cells

Currently it is well accepted that organic solar devices are excitonic solar cells [6,9,10]. In such cells, the physical processes for light to electricity conversion include: light absorption, exciton diffusion, charge separation, charge transport and charge collection as illustrated in figure 1.3. Initially, the photon absorption takes place in the active layer which is formed by a combination of a donor and an acceptor material [6]. A hole-electron pair, bounded by Coulombic forces [9,10], is formed after this absorption. One of the main limitations of the organic solar cell is the fact this exciton particle needs to be splitted into charges which requires an energy of around

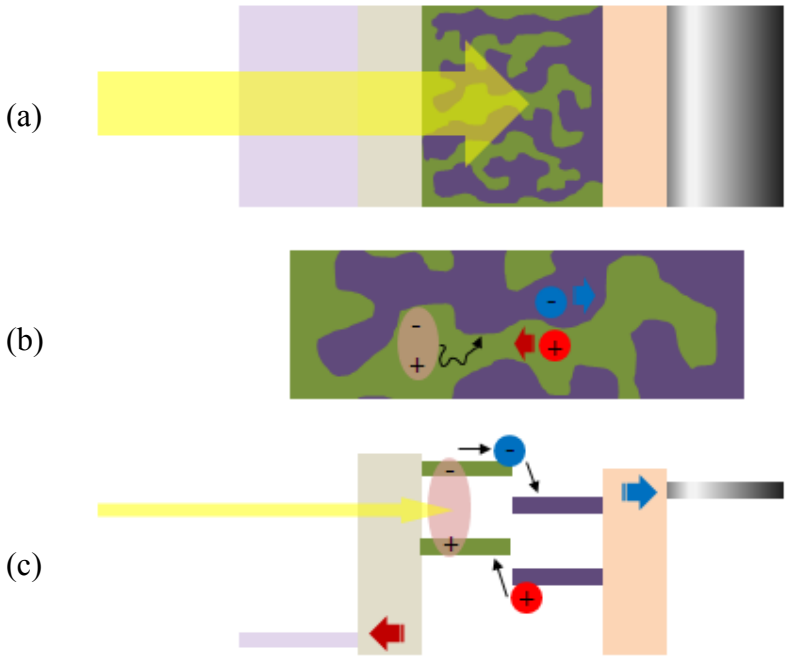

Figure 1.3. (a) Illustrated physical phenomena in an organic solar device, (b) schema of the exction diffusion and charge splitting and (c) energy level configurations.

0.4eV. After its generation, the exciton starts to diffuse in the active material. Its lifetime is about 0.5 ns [11] which is equivalent to a diffusion length around 20 nm [10]. During this period the exciton needs to split into charges otherwise a recombination process, radiative or non-radiative, would take place. The morphology of the active layer is fundamental for preventing this energy loss. In the early polymer solar cell architectures, the donor and acceptor materials were deposited in a bilayer configuration. The thickness of such individual layers was limited by the diffusion length of the excitons which has been estimated to be around 20 nm [12]. Such thin active layer conditioned the device to have low charge generation and consequently a poor performance. A major advance was achieved after mixing the donor and acceptor materials to form a bulk-heterojunction blend [10]. However, controlling the morphology of such blends is still a challenge.

The splitting into separated electron and hole charges takes place when the exciton

reaches the donor-acceptor interface. Afterwards, the charges travel in their corresponding semiconducting buffer layer named electron transporting layer (ETL), also known as hole blocking layer, and hole transporting layer (HTL), also known as electron blocking layer, which must also block excitons for preventing recombination. Finally, such buffer layers are connected to the electrodes (anode and cathode) to extract the charges. Such connection depends on the work function of the electrode and the corresponding valence or conduction band of the ETL or HTL, respectively.

To account for the likelihood of photon conversion to charges, one defines the external quantum efficiency (EQE) according to the equation [6]

$$EQE(\lambda) = \eta_{abs}(\lambda)\eta_{dif}\eta_{tc}\eta_{tr}\eta_{cc} = \eta_{abs}(\lambda) \cdot \phi \tag{1.1}$$

where $\eta_{abs}(\lambda)$ corresponds to the efficiency in photon absorption, η_{dif} the efficiency in exciton diffusion , η_{tc} the efficiency in charge separation, η_{tr} the efficiency in carriers transport and η_{cc} the efficiency in carriers collection. ϕ stands as the product of the wavelength independent efficiencies and can be denoted as the absorbed photon to current conversion efficiency.

The electrical characterization of a solar device is achieved with a Current density – Voltage curve commonly named JV or IV curve as the one shown in figure 1.4. From this graph the main characteristic parameters of an organic solar cell as the open-circuit voltage V_{oc} and the short-circuit current density J_{sc} can be extracted. The fill factor FF is defined as

$$FF = \frac{P_{max}}{J_{sc}\, V_{oc}} \tag{1.2}$$

and the power conversion efficiency as

$$PCE = \frac{P_{max}}{P_{sunlight}} = \frac{FF \cdot J_{sc} \cdot V_{oc}}{P_{sunlight}} \tag{1.3}$$

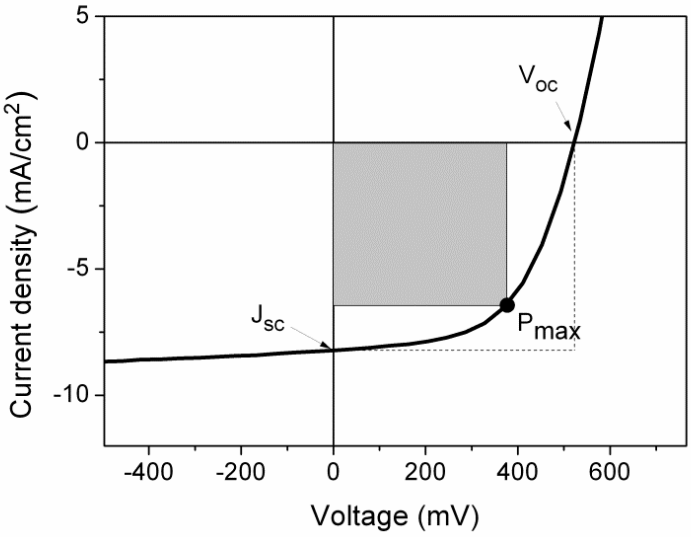

Figure 1.4. Typical characterization JV curve.

where P_{max} is the maximum power provided by the solar device and $P_{sunlight}$ the incoming light from the sun. Given that the power provided by the sun has a strong dependence on the geographical location and time of the day, 1000 Wm^{-2} of the AM1.5G illumination, whose spectrum is shown in figure 1.5(a), is commonly used as the standard reference [3].

The wavelength dependent photon to charge conversion efficiency is obtained by measuring the EQE defined by equation (1.1). An example of such curve is shown in figure 1.5(b) for a 150 nm thick P3HT:PCBM OPV device. The definition of the EQE is calculated based on all photons incident on a solar device including photons that may never reach the active material such as the ones reflected or scattered out from the device. In order to consider only photons that are absorbed by the active layer, the internal quantum efficiency (IQE) is defined as $EQE/(1-R(\lambda))$ being $R(\lambda)$ the reflection of the device. Therefore the IQE is always larger than the EQE as shown in figure 1.5(b) and a good matching between both EQE and IQE implies a proper photon harvesting in the device.

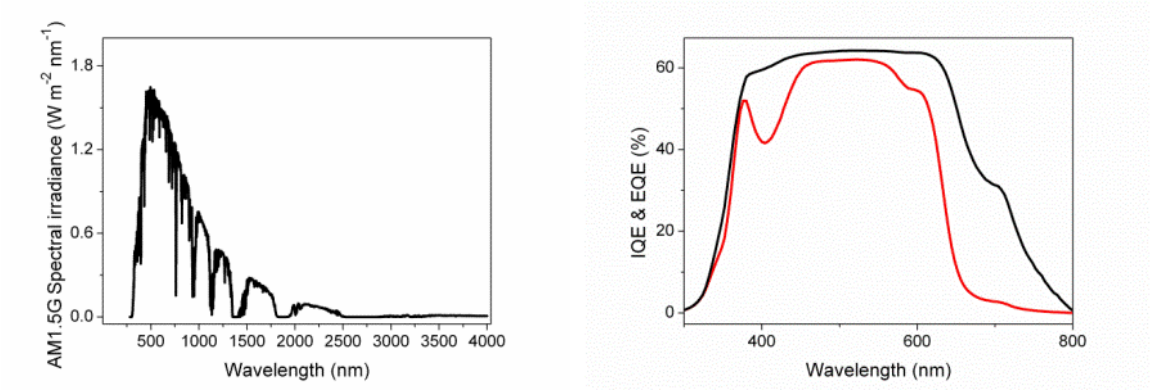

(a) (b)

Figure 1.5. (a) Spectral irradiance of the sunlight at ground level. (b) EQE (red) of a P3HT:PCBM device compared to its IQE (black).

Several materials and device architectures have been implemented in the OPV field. A single junction organic solar cell is basically a multilayered device where an active layer is sandwiched in between two electrodes. At least one of these electrodes needs to be semi-transparent. At both interfaces between the active material and electrodes, a buffer layer is placed in order to transport selectively a type of carrier and block the opposite one as well as excitons. As mentioned previously, the active material is formed by a donor and acceptor material in either a bilayer of bulk-heterojunction configuration. For the donor materials probably the most commonly used one is the Poly(3-hexylthiophene) (P3HT) which can be used to fabricate devices with efficiencies that are typically between 3 and 5%. Recently new low-bandgap donor materials have been developed such as for instance Poly[[9-(1-octylnonyl)-9H-carbazole-2,7-diyl] -2,5-thiophenediy l-2,1,3-benzothiadiazole-4,7-diyl-2,5-thiophenediyl] (PCDTBT), Poly[4,8-bis-substituted-benzo[1,2-b:4,5-b0]dithiophene-2,6-diyl-alt-4-substituted-thieno[3, 4-b]thiophene-2,6-diyl] (PBDTTT) and Poly[[4,8-bis[(2-ethylhexyl)oxy]-benzo[1,2-b:4,5-b'] dithiophene-2,6-diyl] [3-fluoro-2-[(2-ethylhexyl)carbonyl]thieno[3,4-b]thiophe-nediyl]] (PTB7) which has allowed to fabricate single junction OPV devices with efficiencies above 8% [6,13–15]. On the other hand, the most efficient known acceptor materials are the fullerene and fullerene derivatives particularly [6,6]-Phenyl-C61-butyric acid methyl ester $PC_{61}BM$ and [6,6]-Phenyl-C71-butyric acid methyl ester $PC_{71}BM$ [6,15]. At the interface between the active

layer and the electrodes the most commonly used hole transporting layer (HTL) is PEDOT. Several alternatives have been found such as molybdenum oxide (MoO_3), nickel oxide (NiO) and tungsten oxide (WO_3) [16–21]. For the complementary buffer layer, that is the electron transporting layer (ETL), several materials have also been developed, for instance lithium fluoride (LiF), Anatase titanium oxide (TiO_2) , zinc oxide ZnO, bathocuproine (BCP) and poly [(9,9-bis(3′-(*N*,*N*-dimethyla-mino) propyl)-2,7-fluorene)- *alt* -2,7-(9,9–dioctylfl uorene)] (PFN). Sometimes metals as calcium of ytterbium are also employed [6,14,19,22,23]. As transparent electrodes, the indium-tin oxide (ITO) is probably the most commonly used but there are other alternatives such as aluminium-doped zinc oxide (AZO), fluorinated-tin oxide (FTO) and thin metallic layers made of copper, nickel and silver [18,24–26]. Research is being performed by employing other kinds of electrodes based on metallic nanowires, carbon nanotubes and graphene [24,27–29]. On the other hand the opaque electrodes are usually made of aluminum, silver or gold.

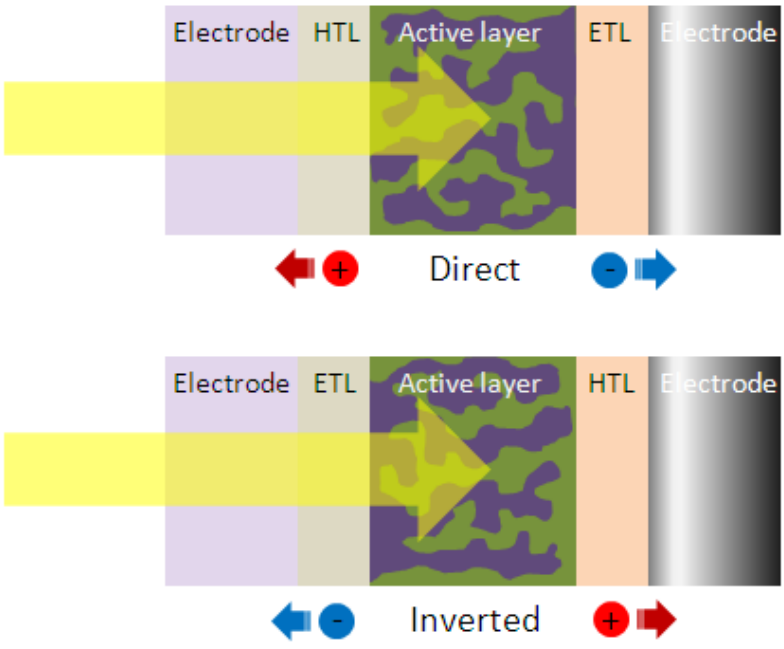

Figure 1.6. Architecture types depending on the charges collected by the semi-transparent electrode though which the sunlight enters the cell

Depending on the type of charges collected by the semi-transparent electrode through which the sunlight enters the device, two types of cell configurations can be defined: *direct* if the collected charges by such electrode are holes and *inverted* if those carriers are electrons. A scheme of such devices is shown in figure 1.6.

There are more complex architectures called tandem devices [30] which result from integrating a semi-transparent OPV (STOPV) device, which is achieved after replacing the usual opaque back electrode for a semi-transparent one, with an opaque device. In the case of *parallel* tandem devices a semi-transparent direct (inverted) device is integrated with an opaque inverted (direct) device. This device is also called three-terminal device because it requires extracting charges from the intermediate electrode connecting both single junction architectures. In the case of a *series* tandem device a direct (inverted) device is integrated with an opaque direct (inverted) device. In this configuration is not necessary to collect charges from the intermediate electrode. Therefore, this electrode is usually thinned down to just a few nanometers and it is better known as recombination layer.

1.3 Sunlight harvesting in organic thin film solar cells

Important challenges that the field of organic photovoltaics must face to become a viable alternative in the energy production at large scale include: enhancing its power conversion efficiency, developing adequate processes to up-scale the fabrication of cells to modules [31], implementing fabrication procedures that lead to a continuous production of modules [31–36], and finding materials and cell architectures that would result in devices with a larger degree of stability [37–39]. The first of these challenges is intimately related to an optimal sunlight harvesting which can be addressed from either a materials science or an optical perspective.

The material science approach has been mainly focused on the development of air stable low-bandgap materials [40]. However, material science research has also tried

to improve the properties of the rest of layers in the cell architecture. For the buffer layers, research has been guided to the development of new materials for both hole and electron transporting layers. Some of these materials came from the OLEDs industry [30,41] and the final target has been to provide higher carrier density and carrier mobility and, for some materials, a better stability in ambient condition has also been reached [21]. Finally, the research on semi-transparent electrodes has been focused in increasing their transmittance, particularly in the absorption band of the active material and, at the same time, keeping a low sheet resistance for favoring charge collection.

To reach the optimal photoconversion efficiency in organic photovoltaic cells it is rather important to optically enhance the photon harvesting provided the absorption band of the materials used is typically narrower when compared to other photovoltaic devices. In addition, OPV active materials suffer from a low mobility of charged carriers which prevents the use of thick materials for a more effective photon absorption [42]. For instance, for the PCDTBT:$PC_{71}BM$ bulk-heterojunction, the absorption length in the visible spectrum is around 250 nm. However, the active layer thickness is typically 90 nm because thicker layers would disrupt the morphology and finally affect negatively the electrical properties of the device due to the short-range molecular order of this particular material [43]. To reach an efficient photon absorption in such rather thin active polymer layers, one of the approaches is to disperse light more effectively within such active layer. Recently, special attention has been given to the inclusion of metal nano-particles to enhance absorption and scattering of light [11,44,45]. Some encouraging results have been reached, showing an increase of the EQE for a broad range of wavelengths [11].

Within the optical approach framework to enhance the OPV devices performance, in this thesis we explore the photon control in OPV devices by taking advantage of optical interference effects which to some extent allow to overcome the restriction of having to employ thin active layers. When considering light absorption, an OPV device can be treated as a stack of homogeneous layers where each layer is defined by its thickness and complex refractive index n and k.

Light propagation in such configuration can be described by solving within each layer the wave equation

$$\left(\nabla^2 - \mu_l \epsilon_l \frac{\partial^2}{\partial t^2}\right) \vec{E} = 0 \tag{1.4}$$

for the electric field $\vec{E}$ where ∇^2 is the Laplace operator. The permeability μ_l and the permittivity ϵ_l of a given layer l are associated to the speed of light in that layer according to $v_l = {1}/{\sqrt{\mu_l \epsilon_l}}$.

A general solution for eq. (1.4) can be written as a superposition of plane waves such as

$$\vec{E}(\vec{r}, t) = E\, \hat{u}\, e^{i(\vec{k}_l \vec{r} - \omega t)} \tag{1.5}$$

here E is the amplitude of the field, $\hat{u}$ is the unit vector in the direction of oscillation, $\vec{k}_l$ the wave vector, ω is the angular frequency, $\vec{r}$ corresponds to the position within a given layer and t denotes the time. For an electromagnetic plane wave, the electric and magnetic field are perpendicular to each other and their amplitudes related to each other by $E = v_l \cdot B$. In accordance, in the rest of this section we will just consider the solution for the electrical field.

As shown in figure 1.7, we will consider propagation in the z direction perpendicular to the multilayer stack. An incident wave, with wave vector $\vec{k}_a = k_a\, \hat{z}$ being $\hat{z}$ the unit vector in the z-direction, reaches the device from the right producing a transmitted and a reflected wave at each interface. In that event, at the l^{th} layer, the total electrical field corresponds to the addition of just two plane waves: one propagating towards $+z$, indicated by $\vec{E}_l^{+}(z,t)$, and other component propagating towards $-z$, indicated by $\vec{E}_l^{-}(z,t)$. Consequently, the superpositions of such two counter propagating waves results in:

$$\vec{E}_l(z,t) = \vec{E}_l^{+}(z,t) + \vec{E}_l^{-}(z,t) = (E_l^{+} e^{ik_l z - i\omega t} + E_l^{-} e^{-ik_l z - i\omega t})\, \hat{y} \tag{1.6}$$

where E_l^+ and E_l^- correspond to the amplitudes for the electrical fields propagating towards +z and -z, respectively and $k_l = \vec{k}_l \cdot \hat{z}$.

As shown in figure 1.7, in an OPV device there would be no field incident from the right of the device. In other words, the amplitude for the E_l^- when $l = L$, being L the index to identify the last layer, which commonly will be air, would be zero. Assuming that E_L^+ has a finite value and setting the appropriate boundary conditions at the interface between the L and $L-1$ layers, it is possible to determine the amplitudes E_{L-1}^+ and E_{L-1}^- in terms of E_L^+ and E_L^- by establishing the continuity of the tangential component of the electric and magnetic fields. The same procedure can be applied to the interface, localized at $z_{l-1} \equiv \sum_{l=1}^{l-1} d_l$, between the $(l-1)^{th}$ and the l^{th} layers, where l is any integer from 1 to L,

$$E_{l-1}^+ e^{ik_{l-1}z_{l-1}} + E_{l-1}^- e^{-ik_{l-1}z_{l-1}} = E_l^+ e^{ik_l z_{l-1}} + E_l^- e^{-ik_l z_{l-1}} \quad (1.7a)$$

$$ik_{l-1}E_{l-1}^+ e^{ik_{l-1}z_{l-1}} - ik_{l-1}E_{l-1}^- e^{-ik_{l-1}z_{l-1}} = ik_l E_l^+ e^{ik_l z_{l-1}} - ik_l E_l^- e^{-ik_l z_{l-1}} \quad (1.7b)$$

Typically the substrate is a 1 or 2 mm thick piece of glass. For such thick layer the superposition of $\vec{E}_o^+$ and $\vec{E}_o^-$ cannot be assumed to always be coherent. Considering the

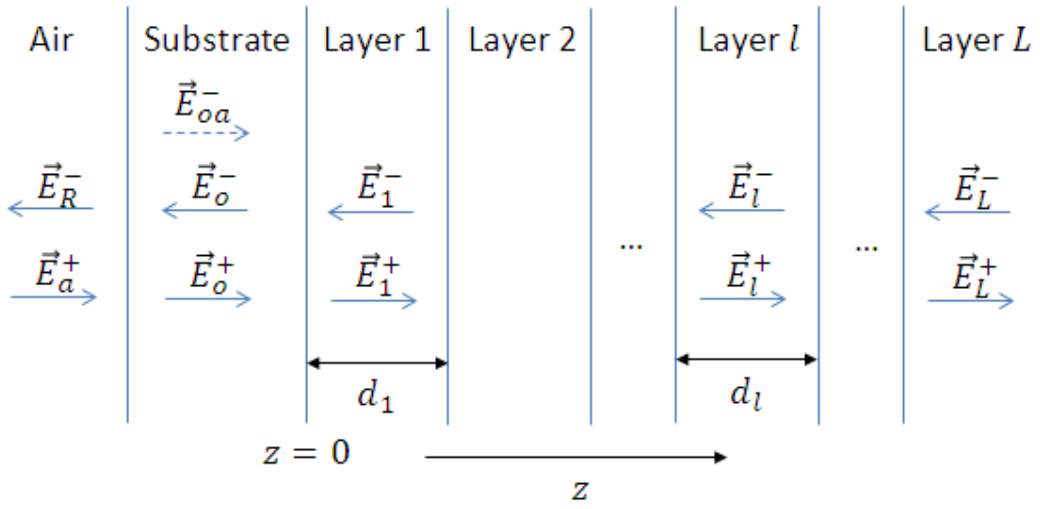

Figure 1.7. Schematic general optical approach to an organic solar cell.

bandwidth of the measuring equipment and inhomogeneities in the parallelism of the substrate opposite faces, it is reasonable to simply relate E_o^+ and E_o^- to the incoming field E_a^+ through the intensity Fresnel equations [46]. For energy conservation, at the interface between air and the substrate one must also add the field reflected back to the device, $\vec{E}_{oa}^-$, which is different from $\vec{E}_o^+$. With all such considerations in mind and by a simple matrix multiplication one may determine the device transmitted and reflected electric fields, E_L^+ and E_o^- respectively, in terms of the amplitude of the incident field E_a^+.

One may also determine E_l^+ and E_l^- for any given layer l in terms of the incoming light amplitude E_a^+. This can be used to calculate the energy dissipated in a given volume V (surrounded by the area s) of the device as [47]

$$Abs = Re\left\{-\frac{1}{2}\int \vec{E}(z,t)\cdot\vec{J}_d^*\, dV = \frac{1}{2}\int_s \vec{E}(z,t)\times\vec{H}^*\, d\vec{s}\right\} \tag{1.8}$$

Where $\vec{J}_d^*$ is the current density of the electric field that for harmonic waves can be written as $i\omega{\epsilon_l}^*\vec{E}^*(z,t)$. Provided that all layers in the cell are considered homogeneous and ϵ_l is independent of the position within each layer, eq. (1.8) can be simplified to

$$Abs_l = \frac{2\pi c n_l k_l \epsilon_o}{\lambda}\int\left|\vec{E}_l(z,t)\right|^2 dV \tag{1.9}$$

for any given layer l. In particular, applying eq. (1.9) for the active layer (AL), eq. (1.1) and the sunlight photon flux (under AM1.5G conditions) $F(\lambda)$, it is possible to predict the short-circuit current density produced by the device according to

$$J_{sc} = q\int EQE(\lambda)F(\lambda)d\lambda = \phi\, q\int\left[\frac{2\pi c n_{AL} k_{AL}\epsilon_o}{\lambda}\int\left|\vec{E}_{AL}(z,t)\right|^2 dV\right] F(\lambda)\, d\lambda \tag{1.10}$$

where q stands for the electron charge. As shown is eq. (1.10), a clear dependence of

the J_{sc} of the device with the distribution of the electrical field intensity $\left|\vec{E}_{AL}(z,t)\right|^2$ is apparent. Considering that such intensity is critically determined by the refractive index, transmittance and thicknesses of the different layers forming the device architecture, is clear that by implementing specific device architectures is possible to achieve a proper photon absorption in the active layer. Additionally, eq. (1.9) also allows calculating the absorption in other layers besides the active which is helpful in order to account for parasitic absorptions.

1.4 Thesis summary

The multilayered structure in an OPV device, where each material has a different complex refractive index and thickness, plays a determining role in the interaction of the active material with the sun photons. Indeed, the final optical field distribution and, eventually, the photon harvesting capability of the device are strongly linked to such layered architecture.

In the remaining chapters of the present thesis, different aspects of such layered architecture will be modified to obtain an optimal photon absorption in the different OPV cell configurations under study. First, in chapter 2, I consider the simplest way to modify and control the optical field distribution in the cell which is implemented by changing the relative thicknesses of the different layers in the device, including the active layer, the buffer layers and the electrodes. In chapter 3, the optical interference in such multilayer structure is controlled and optimized by considering the direct modification of the n and k of any given layer in the cell. This approach is evaluated for different cell configurations by introducing new materials that replace commonly used layers.

Finally, a photon management to cover the entire active material absorption wavelength range is investigated in chapter 4. More specifically, an optimal photon harvesting in a semi-transparent OPV device is found by integrating it to a one-

dimensional non-periodic dielectric layered structure that provides a wavelength control similar to the one achieved when using photonic crystals. The entire cell plus photonic crystal structure is designed to transmit visible light and to localize NIR and UVA photons enhancing considerably the final device performance. The same principle is applied for tuning the transmitted color of such semi-transparent device.

Chapter 2

Induced sunlight localization by tuning the device architecture

The basic architecture of an organic solar cell involves an active layer in between two electrodes and two buffer layers placed at the active layer / electrode interfaces. In the end, typically a minimum of five layers is involved, all of them with different thickness and optical constants which gives room for a fine device optical tuning intended to enhance the device performance. In this chapter, the main objective is to find the optimal device architecture by controlling the optical interference resulting in such five layered structure [19].

We show experimentally that by properly selecting the thicknesses of the different layers in an inverted Poly(3-hexylthiophene) (P3HT) : [6,6]-phenyl-C_{61}-butyric acid methyl ester (PCBM) cell, the optical interference is such that the EQE reaches 91% of the IQE. Additionally, we observe that the device reflectivity is minimized in a wavelength range of more than 100 nm. In that range the EQE closely matches the IQE. The experimental observation is confirmed by the EQE calculated numerically using the transfer matrix model described in section 1.3. At the same time we demonstrate that when the relative thicknesses of all layers are not combined properly, thicker cells may exhibit lower PCEs. As it has been shown in the past [48–52],

absorption within the active layer may be strongly affected by the relative thickness between the five layers that constitute the cell.

2.1 Device multilayer stack optimization

We consider an inverted bulk hetero-junction cell where TiO_2 nanoparticles (TiO_2-np) are employed as electron transporting layer deposited on top of ITO. The active layer considered is a blend of P3HT:PCBM. In between such active region and the Ag top electrode we deposited a hole transporting layer of MoO_3. As schematically shown in figure 2.1, in this cell architecture we allow to vary freely, within a limited range of thicknesses, the ITO, TiO_2-np, active material and MoO_3 layers.

As shown in chapter 1, photon absorption in the active layer can be determined after integrating within the active layer volume the field intensity distribution (cf. Eq. (1.9)).

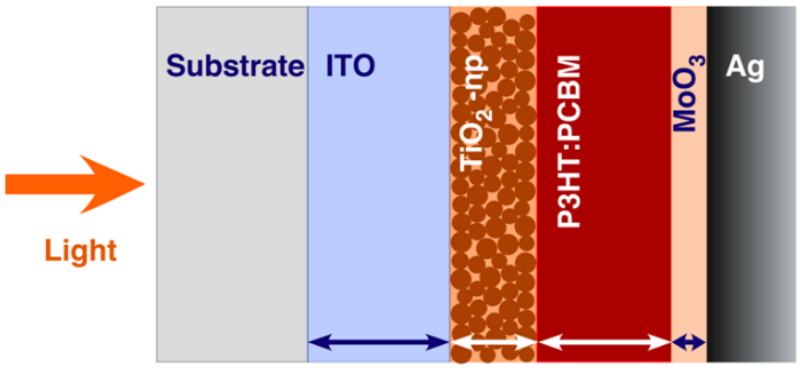

Figure 2.1. Inverted cell architecture. The five layers of the cell are deposited on top of a transparent substrate. ITO corresponds to the cathode, TiO_2-np the electron transporting layer, P3HT:PCBM the bulk hetero-junction active layer, MoO_3 the hole transporting layer, and Ag the anode. When numerically determining the electric field distribution it is assumed that the *z*-direction is perpendicular to all interfaces.

The parameters such as n and k were determined by ellipsometry in the 400 – 800 nm range for all layers except for the Ag layer, whose n and k dispersion curves were taken from the literature [53]. When all such parameters are known, the integration of equation (1.9) can be performed numerically as in

$$Abs_{AL} = \frac{2\pi c n_{AL} k_{AL} \epsilon_o}{\lambda} \sum_i |E_{AL}(z)|^2 \Delta z_i A \tag{2.1}$$

where Δz_i is the integration interval in the z-direction, z_i the center value for z within that interval, A the surface on a plane perpendicular to the z-axis (cf. figure 2.1 caption) for the volume of integration enclosing the active layer. The result of this summation is used to compute the absorption within the active layer. Given the linearity of the field equations, the total number of sun photons absorbed can be computed by Fourier transforming the electric field and then adding the contribution at each wavelength weighted by the sun photon distribution. In an organic solar cell, photons when absorbed are converted to excitons which diffuse within the active layer. As explained in chapter 1, in a bulk hetero-junction, such created excitons would encounter a charge separation interface immediately after being created, which, among other things, has the positive effect of limiting recombination losses. The created charge carriers are separated by the electric field near the cathode [54]. In other words, the length excitons must diffuse is minimized in such bulk hetero-junction cells. Then, it is reasonable to take the photon to charge conversion efficiency as a dispersionless parameter. This constant should be multiplied by the dispersionless parameter ϕ introduced in chapter 1, which is proportional to the exciton diffusion, charge carrier separation, transport and collection efficiencies [55]. This constant value, ranging between 0 and 1, is determined empirically after many experimental measurements of the EQE. Thus the EQE can be computed, according to Eq. (1.1), as the product of such ϕ and the result of the integration of equation (1.9). Finally, we may use Eqs. (2.1) and (1.10) to calculate J_{sc}. Figure 2.2(a) shows the J_{sc} values obtained after varying the thicknesses of the TiO_2-np, MoO_3 and active layer. In agreement with the experimental measurement of the EQE, the ϕ used in here and in the rest of the

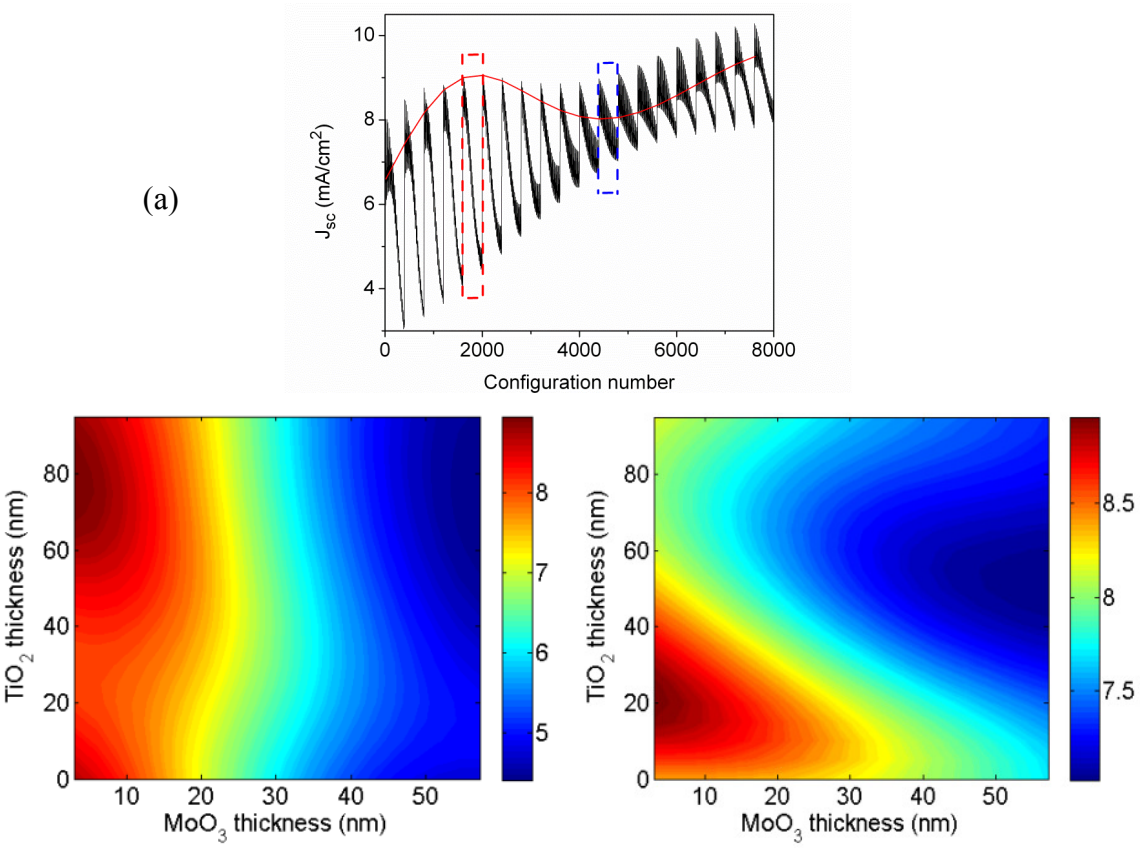

Figure 2.2 (a) Numerically calculated J_{sc} for 8000 different combinations of the TiO_2, P3HT:PCBM and MoO_3 layer thicknesses. The P3HT:PCBM layer thickness varies from 60 to 220nm (left to right in the x-axis) and is fixed in each segment (for instance the areas marked in red and blue). When the TiO_2 and MoO_3 are fixed to 80 and 3 nm respectively, the J_{sc} corresponds to the red solid line. (b) The area marked in red in (a) is shown here in a 2D plot and corresponds to the J_{sc} dependence on TiO_2 and MoO_3 thicknesses when the P3HT:PCBM layer was chosen to be 91 nm. (c) Same as figure 2.2(b) but when the P3HT:PCBM was chosen to be 151 nm, corresponding to the area marked in blue in (a).

numerical calculations throughout this chapter was 0.65. In the numerical calculations, the active layer thickness ranges from 60 to 220nm. For a given active layer thickness a total of 400 cell configurations are considered by varying the TiO_2 layer between 0

and 100 nm and the MoO_3 between 0 and 60 nm. The expected J_{sc} when these two layers are varied and the active layer thickness is kept fixed to 91nm, dotted region in figure 2.2(a), is shown in detail in figure 2.2(b). We observe that the largest J_{sc} is obtained when the MoO_3 layer is kept under 10 nm and the TiO_2 layer thickness in the 70-85 nm range. We also considered the cell performance dependence on ITO thickness (not shown in figure 2.2) and found that for any kind of layer combination the optimal ITO thickness was approximately 100 nm.

When the thicknesses of ITO, TiO_2-np and MoO_3 are fixed to 100, 80 and 3 nm, respectively, the J_{sc} dependence to the active layer thickness is shown in figure 2.2(a). Note that such combination of layer thicknesses leads to an optimal performance for cells whose active layer thickness is around 100 nm (corresponding to a configuration number in figure 2.2(a) close to 2000). As can be seen from figure 2.2(c), optimization of cells whose active layer thickness were to be close to 151 nm (configuration number around 4000) would require to adjust the TiO_2 thickness to 20 nm.

2.2 EQE and IQE analysis

As indicated, we fabricated the inverted structure ITO/TiO_2-np/P3HT:PCBM/MoO_3/Ag to experimentally study the active layer thickness dependence shown in figure 2.2(a) while the ITO, TiO_2 and MoO_3 layers thicknesses were kept fixed at 100, 77 and 3 nm, respectively. All layer thicknesses were accurately measured using an atomic force microscope (AFM) in tapping mode after scratching the layers. The dependence of the J_{sc} on the blend thickness shown in figure 2.3(a) exhibits a very good agreement with the model prediction obtained using eqs. (1.10) and (2.1). The relative maximum and minimum for the J_{sc} are a clear indication that optical interference is responsible for a field redistribution to enhance absorption within the active layer and to subsequently improve the performance of the solar cell. Photovoltaic parameters for all the fabricated P3HT:PCBM cells are given in Table 2.1. As expected, while there is a correlation between the J_{sc} and active layer

Table 2.1. Device characteristic parameters

Active layer thickness [nm]	J_{sc} [mA/cm^2]	V_{oc} [mV]	PCE [%]	FF [%]
69	-7.9	598	2.8	61
84	-8.7	571	3.1	63
91	-8.9	570	3.1	61
102	-9.0	594	3.3	62
110	-8.6	589	3.0	59
128	-8.5	583	2.9	61
142	-8.1	585	3.0	65
151	-8.3	579	2.8	59

thickness, no such correlation can be found between such layer thickness and the V_{oc} or *FF*. As seen in figure 2.2(b), the model predicts a weak dependence of the J_{sc} with the thickness of the electron transporting layer of TiO_2-np. When the hole transportinglayer is fixed to a thickness of 3 nm, the J_{sc} exhibits an oscillatory pattern, which is shown in figure 2.3(b) for three different active layer thicknesses. In the same figure 2.3(b), we observe that the position of maxima and minima for such oscillation move as the thickness of the active layer is changed. Experimental measurements of the J_{sc} for different thickness of the TiO_2-np layer, shown in figure 2.3(b), indicate that to some extent, the experimental measurements follow the trend predicted by the theoretical model. More precise measurements are difficult to achieve in this case provided that the average size of the nano- particles is 6±3 nm. We also measured the J_{sc} dependence with the thickness of the hole transporting layer of MoO_3. As seen in figure 2.3(c), we observe that, as predicted by the theoretical model, when the thickness of such layer increases, the J_{sc} diminishes.

Representative J-V curves for the region of the local minimum (active layer thickness around 150 nm), the region of the local maximum (active layer thickness around 100 nm) and the region of very thin active layers (active layer thickness less than 80 nm)

(a)

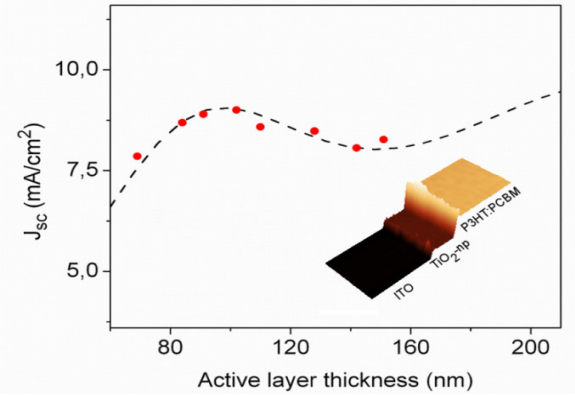

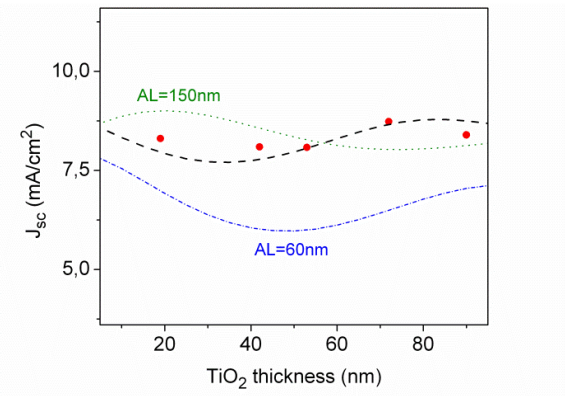

(b)

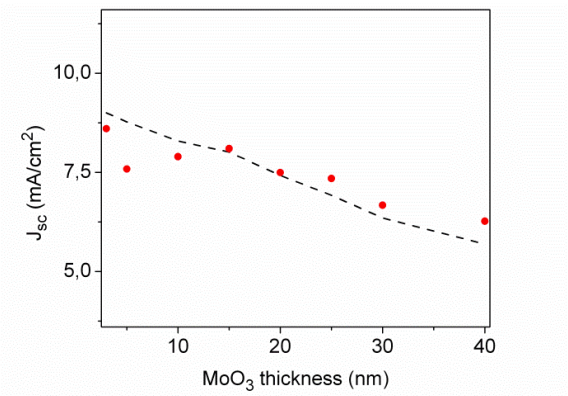

(c)

Figure 2.3 (a) Calculated J_{sc} as a function of the active layer thickness (dashed line) and experimentally determined J_{sc} for 8 different cells when the TiO_2-np and MoO_3 layer thicknesses are fixed to 77 nm and 3 nm, respectively. Inset: Example of an AFM image used to accurately determine all layer thicknesses. (b) Calculated J_{sc} as a function of the TiO_2-np layer thickness (dashed black line) and experimentally determined J_{sc} for 5 different cells when the active and MoO_3 layer thicknesses are fixed to 81 nm and 3 nm, respectively. The dotted and dot-dashed lines show the changes in the J_{sc} pattern when the thickness of the active layer (AL) is modified. (c) Calculated J_{sc} as a function of the MoO_3 layer thickness (dashed line) and experimentally determined J_{sc} for 8 different cells when the active layer thickness ranges from 80 nm to 110 nm and the TiO_2-np layer thickness is fixed to 95 nm.

are shown in figure 2.4. The experimentally measured and numerically calculated

EQEs for three different layer thicknesses corresponding to the three regions of interest are shown in figure 2.5(a). We observe that when the active layer thickness equals 91 nm, the EQE approaches the IQE predicted by the model, also shown in figure 2.5(a). Note also that the experimentally measured EQE agrees remarkably well with the numerically predicted one. In the wavelength range of 450-625 nm, where the majority of excitons are created, the EQE amounts to 91 % of the IQE. This is in accordance to the better performance of the device expected from inspection of figures 2.3(a) or 2.4, which show a maximum J_{sc} when the active layer thickness is close to 100 nm. When the active layer is 151 nm, corresponding to the relative minimum in J_{sc} seen in figure 2.3(a), the numerically predicted EQE in the same wavelength range considered above amounts to only 72% of the IQE. Such large differences in the EQE among the two cases considered can be attributed to significant differences in the reflectivities from both devices. As shown in figure 2.5(b), for the 91 nm active layer thickness case, the optical interference is such that reflectivity is minimized for the range where the majority of excitons are created. In fact, reflectivity is very close to just the reflectivity of the first substrate interface in the 450-550 nm range; the same

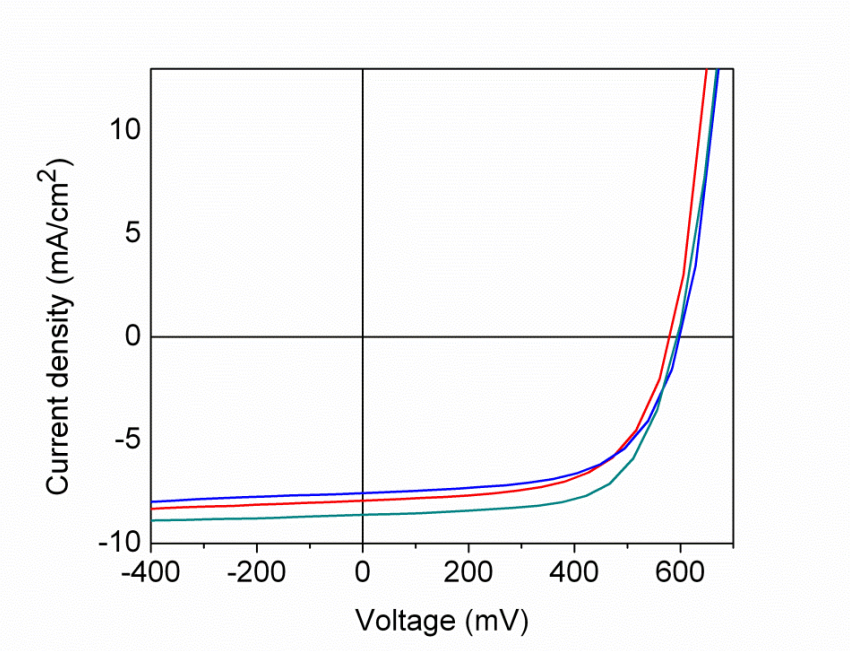

Figure 2.4 J-V curves for different active layer thicknesses: 69 nm (blue), 102 nm (dark cyan) and 151 nm (red).

range where the EQE almost perfectly matches the IQE. On the contrary, for the 151 nm case, the layer combination considered does not provide an adequate optical interference optimization and, as seen in figure 2.5(b), reflectivity does not approach zero at any wavelength of interest. However, as it can be inferred from figure 2.2(c), an optical based optimization, which would essentially require to change the TiO_2 layer thickness, is possible for such later cell. In that event, the 151 nm active layer cell would exhibit a similar performance as the 91 nm active layer one. In other words, the appropriate optical interference may lead to cells whose active layer thickness is 60% of the thicker one but without any loss in efficiency. When the active layer thickness is 69 nm, as seen in figure 2.5(a), the behavior of the EQE relative to the IQE follows the increase in reflectivity relative to the 91 nm active layer case. Here, again, there is a very good agreement between the calculated and experimental EQEs.

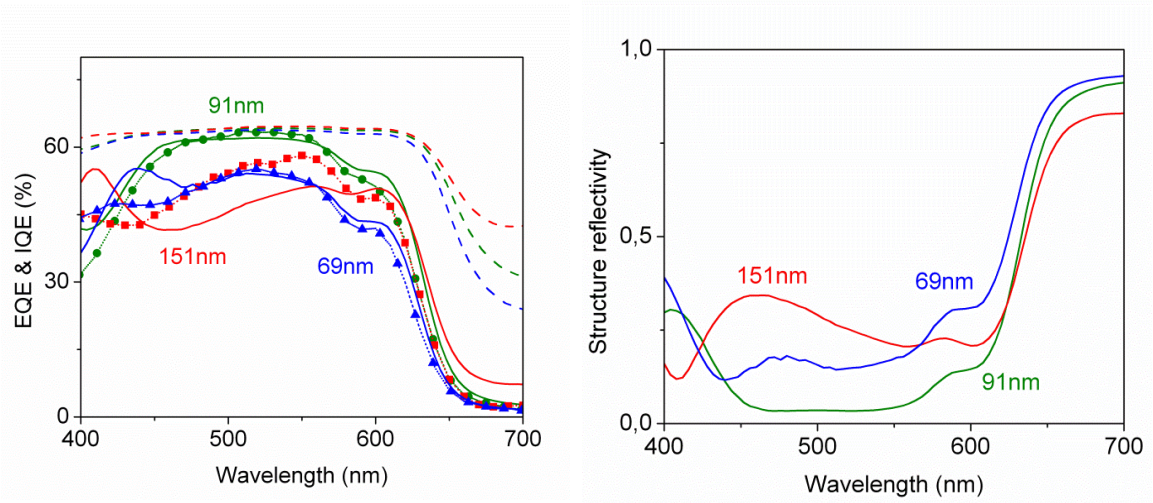

(a) (b)

Figure 2.5 (a) EQE numerically determined (solid lines), experimentally measured (dotted lines plus symbol) and IQE numerically determined (dashed lines) for a 69 nm (blue), 91 nm (green) and 151 nm (red) active layer thick cells. The dotted lines connecting the experimental data points are only a guide for the eye. (b) Numerically determined reflectivities for a 69 nm (blue solid line), a 91 nm (green solid line) and a 151 nm (red solid line) active layer thick cells.

The trend is that when the active layer is thinner, deviations of the theoretical prediction from the experimentally measured EQEs are limited to the high energy range below 475 nm. As the active layer is made thicker such deviation extends to the long wavelength region.

2.3 Conclusions

In this chapter we have shown that the multilayered structure of an organic solar cell can be tuned for optimizing the photon management into the active layer, that is, for enhancing the photon absorption which drives to a photoconversion efficiency enhancement.

We confirmed, theoretically and experimentally, that optical interference plays a very relevant role to enhance the overall performance of organic photovoltaic devices. We showed that a simultaneous adjustment of all the layers in the device may lead to an EQE that matches the IQE for a large wavelength range. Such matching is achieved for the wavelength range where the absorption of the active material is larger. Provided that in such range the IQE is very close to its maximum value, no further gain should be expected by the inclusion of elements, such as metal nano-particles, meant to enhance photon absorption and diffusion. On the other hand, when such elements are properly tailored, a larger gain should be possible for the long wavelength range where absorption is significantly lower. In addition, for the specific cell configuration considered here, we demonstrate that by adjusting the optical interference, a given device can perform equivalently to a device whose active layer thickness is 1.7 times larger. As it will be seen in chapter 2, the possibility to have an optimal light harvesting using thin active layers is particularly relevant when polymers exhibit a weak short-range molecular order [43] such as Poly [[9-(1-octylnonyl)-9H-carbazole-2,7-diyl] -2,5-thiophenediyl -2,1,3-benzothiadiazole -4,7-diyl-2,5- thiophenediyl] (PCDTBT) [56–58] or Poly [[4,8-bis[(2-ethylhexyl)oxy] benzo[1,2-b:4,5-b'] dithiophene-2,6-diyl] [3-fluoro-2- [(2-ethylhexyl)carbonyl] thieno[3,4-b]

thiophenediyl]] (PTB7) [15].

Chapter 3

The optical role of the non-active layers in an OPV cell

As seen in Eq. (1.10), current generation is explicitly dependent on the n and k of the active layer. However, the n, k and thickness of the remaining layers in an OPV cell (HTL, ETL and electrodes) may also play a determining role in the final light harvesting efficiency. Indeed, an implicit dependence of the J_{sc} on all such parameters is hidden in the electrical field distribution under the volume integral in Eq. (1.10). In this chapter, we consider such optical dependence by analyzing three separate cases. In the first case, a bathocuproine (BCP) layer is employed for replacing calcium as electron transporting layer in a PBDTTT:$PC_{71}BM$ OPV device. The almost null extinction coefficient of the BCP allows minimizing almost to zero the parasitic absorption otherwise induced by the calcium layer. Additionally the possibility of having layers of BCP as thin as 3.5 nm slightly increase the device performance compared to a thicker BCP. At the end, a 7.5% PCE was achieved for the BCP-based device compared to the 6.3% PCE corresponding to the calcium-based device. In the second case, nickel oxide (NiO) was employed for replacing Poly(3,4-ethylenedioxythiophene) poly(styrenesulfonate) (PEDOT:PSS) as hole transporting layer in a P3HT:PCBM OPV device. The inclusion of the NiO enabled to use a thinner HTL which was beneficial for localizing the sunlight inside the active layer. Finally, a

semi-transparent bilayer made of copper-nickel was used for replacing the ITO electrode. With this new electrode, the P3HT:PCBM active material was embedded in between two metal electrodes and an optical cavity effect is demonstrated.

3.1 Optical role of the electron transporting layer

As indicated in chapter 1, in bulk hetero-junction devices with a direct architecture, the work function of ITO and the metal electrode are tuned by a hole transporting layer (HTL) and an electron transporting layer (ETL), respectively. For a common BHJ direct cell, the ITO electrode is modified with PEDOT:PSS, p-type semiconductors such as NiO, or high work function metal oxides such as MoO_3, while the typical ETL is a thin calcium layer modifying a back thick aluminum or silver electrode. In this chapter, we performed a numerical calculation of the optimal light harvesting which demonstrated that a reduced extinction coefficient (k) for the ETL is essential to achieve the largest light absorption by the active layer. In accordance, in the device architecture of figure 3.1, we replaced the typical thin 10-20 nm Ca ETL by a few nanometer thick BCP [59] which is a widely used exciton blocking layer in organic devices such as OLEDs and small molecule solar cells [60,61], but its use in polymer

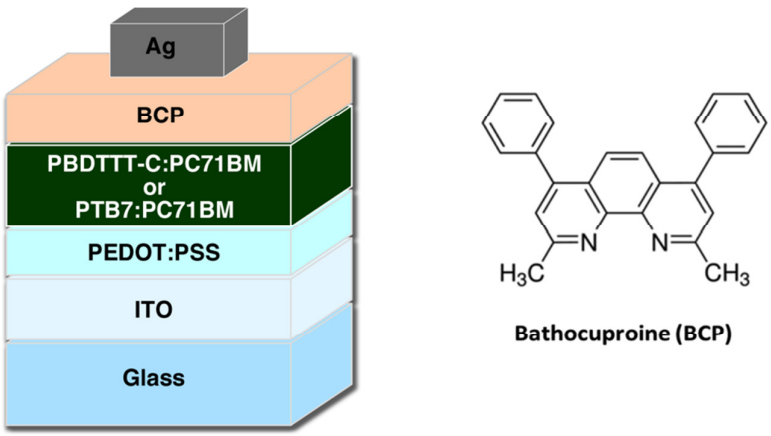

Figure 3.1. Schematic illustration of the device architecture employed and chemical structure of the BCP.

solar cells has been reported in very few occasions [62–64]. A wide band gap of 4.7eV makes it a transparent layer while its low lying LUMO energy level would suggest a large barrier for electrons to reach the cathode. However, electron transport occurs through damage-induced trap states created by the evaporation of hot metal atoms onto the BCP surface [22]. Its wide band gap determines a k value that is close to zero for a broad range of wavelengths [41].

A detailed study of the proposed optically enhanced architecture was performed when using PBBTTT-C as active material which was synthetized in our lab following the procedures described elsewhere [40]. Later, we confirmed the general character of such optical enhancement applying it to cells fabricated using PTB7 as donor material. We fabricated solar cells by blending PBDTTT-C with $PC_{71}BM$ ([6,6]-phenyl-C71-butyric acid methyl ester) at a 1:1.5 ratio (10 mg/mL of polymer) and dissolved in a mixed solvent system composed of 1,2-dichlorobenzene (DCB) and 1,8-diiodooctane (DIO) (97:3 v/v%). DIO has been reported to improve the morphology of the blend by

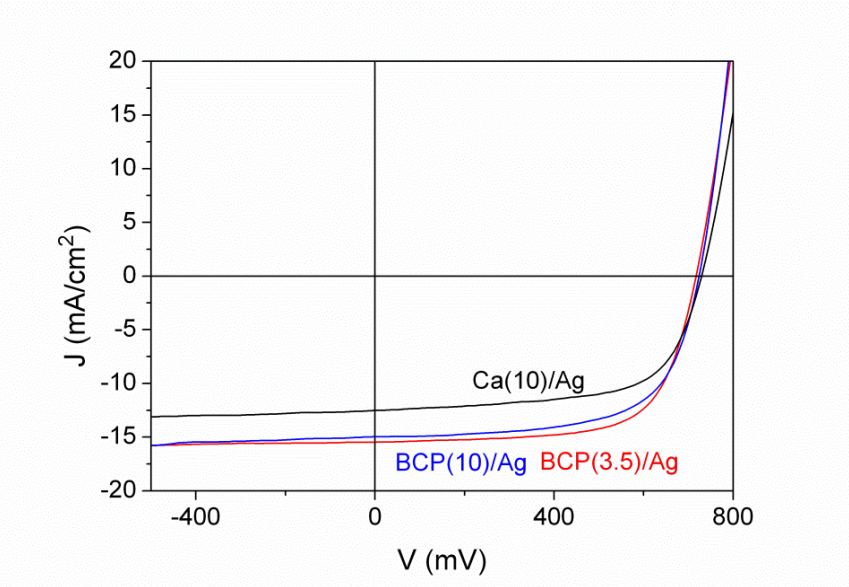

Figure 3.2. J-V curves for devices based on PBDTTT-C blends with different top electrodes: 3.5 nm of BCP and Ag (red solid line), 10 nm of BCP and Ag (blue dashed line) and 10 nm of Ca and Ag (black dotted line).

avoiding segregation of the fullerenes, allowing their intercalation into the polymer domains [65]. This blend was then spin coated over the ITO/PEDOT:PSS anode at different conditions under controlled atmosphere in a globe box. The cathode composed of Ca/Ag or BCP/Ag was thermally evaporated through a mask (0.09 cm^2) after the drying of the blend in an evaporator. In figure 3.2 we show the current density-voltage (J-V) curves of the best PCE solar cell devices studied with three different cathode structures. Two different thicknesses of BCP were chosen for the BCP/Ag top electrode devices, one with a BCP layer of 3.5 nm and the other with a BCP layer of 10 nm. The third device consisted of 10 nm Ca and 90 nm Ag as top electrode. All J-V measurements were performed under the illumination of AM1.5G, 100 mW/cm^2 and results are shown in table 3.1. When the BCP buffer layer was 3.5 nm we achieved a PCE of 7.5% with a short circuit current density (J_{SC}) of 15.5 mA/cm^2, an open circuit voltage (V_{OC}) of 0.717 V, and a FF of 0.68. When the BCP layer thickness is increased up to 10 nm the efficiency dropped to 7%, with a J_{sc} of 15.0 mA/cm^2, a V_{OC} of 0.724 V, and a FF of 0.65. Meanwhile, for the most common structure using Ca/Ag as top electrode the J_{SC}, V_{OC} and FF obtained were 14.6 mA/cm^2, 0.728 V and 0.60 respectively, which resulted in a PCE of 6.3%. As we will see from the discussion below, the efficiencies reported in table 3.1 correspond to devices that were optimized not through a statistical approach but from a proper fine selection of the cell parameters.

Table 3.1. Device characteristic parameters of the PBDTTT-C:$PC_{71}BM$ optimized solar cell devices with different ETL. Numerically predicted short-circuit current density is indicated as J_{sc} theory.

	J_{sc} theory (mA/cm^2)	J_{sc} experimental (mA/cm^2)	V_{oc} (mV)	FF (%)	PCE (%)
Ca(10nm)/Ag	14.64	14.4	728	60.3	6.3
BCP(10nm)/Ag	15.07	15.1	723	64.1	7.0
BCP(3.5nm)/Ag	15.28	15.5	717	67.9	7.5
Ca(10nm)/Al [66]	-	14.7	700	64.1	6.6

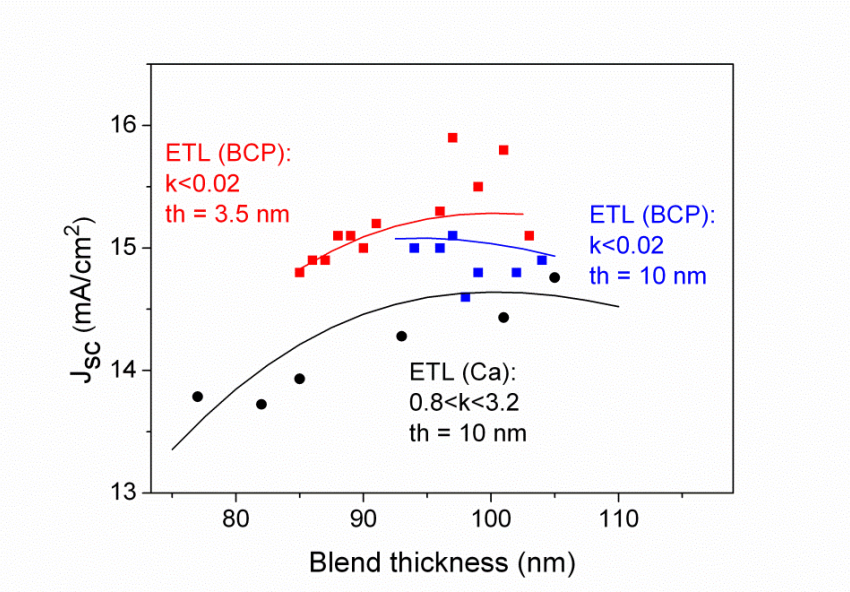

Figure 3.3. Calculated J_{sc} as a function of the PBDTTT-C:$PC_{71}BM$ blend thickness (solid lines) and experimentally determined J_{sc} for devices with top electrode composed of: 3.5 nm of BCP and 90 nm of Ag (red squares), 10 nm of BCP and 90 nm of Ag (blue squares) and 10 nm of Ca and 90 nm of Ag (black dots). The range in extinction coefficient (k) values when the wavelength changes from 300 to 900 nm is indicated by the corresponding data points; th indicates the thickness of the ETL.

When we compare the performance of such optimized BCP devices to other fabricated devices we observe that there is a strong correlation between the combined thickness of the blend and ETL of a given device and its J_{sc} as shown in figure 3.3. The thickness of such layers for each single cell was accurately measured using an atomic force microscope (AFM) in semi-contact mode. In order to perform such measurement a scratch was done on the surface of the polymer. The scratching could be done using a sharp needle [19] or using the AFM measurement tip [67]. This destructive technique, far more accurate than a profilometer, allows for the measurement of different layers in the same device due to the different adhesion properties of those layers (figure 3.4). After the deposition of the top electrode all devices were removed from the globe box for its electrical characterization under the solar simulator, external quantum efficiency (EQE) measurements, and layer thickness AFM characterization at last.

The J_{sc} in terms of the thicknesses of all the layers in a given device can be numerically computed in the same way that was employed in the previous chapter using the transfer matrix method developed in chapter 1 to determine the forward and backward electric field within each layer. Once the electric field distribution inside the cell is known, we computed the EQE by multiplying the photon absorption in the active layer with the wavelength independent photon to charge collection efficiency (see Eq. (1.1)) that for the fabricated cells was determined experimentally to be 0.77. using Eq. (1.1) one may obtain the generated short-circuit current density. The numerically predicted J_{sc} for the three types of cells considered here is also shown in figure 3.3.

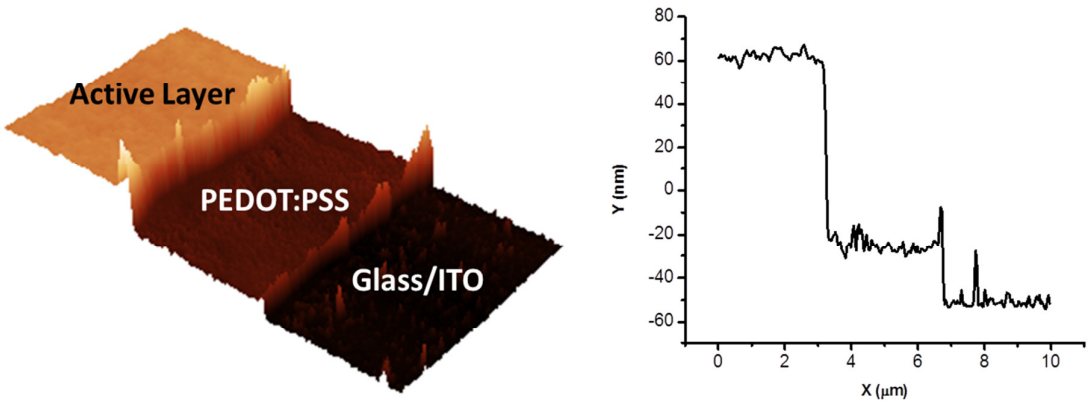

Figure 3.4. 3D AFM image of a scratched area where different layers could be seen. Corresponding profile where the thicknesses of the PEDOT:PSS layer and PBDTTT-C:PC_{71}BM blend layer can be measured.

After lowering the extinction coefficient of the layer next to the cathode, which in our case corresponds to the ETL, the J_{sc} increases as seen in figure 3.3. This can be easily understood if one considers the reflectivity, shown in figure 3.5, of the ETL and back metal combination. For instance, at 600 nm, the reflectivity of the Ca(20nm)/Ag layer is 83% that of the BCP(3.5nm)/Ag layer. Such decrease in reflectivity is detrimental for a stronger light localization within the active layer, and consequently the J_{sc} is reduced significantly. From figure 3.3 it is clear that the experimentally measured J_{sc} dependence on the buffer layer thickness corroborates the model prediction that

optimal cells should be obtained when the extinction coefficient k is reduced significantly. In the case studied here, the reduction in extinction coefficient when changing from Ca to BCP is, for the majority of wavelengths, larger than two orders of magnitude. The experimental data in figure 3.3 indicates that when a 3.5 nm layer of BCP is used the best performance with maximized current density is obtained at active layer thickness of 99 nm. From that cell we measured a PCE of 7.5% with a J_{sc} of 15.5 mA/cm^2, a V_{OC} of 0.717 V and a FF of 0.68. When the ETL is changed from BCP to Ca, as predicted by the theoretical model, a significant decrease in the current density is obtained. The best experimental value obtained for the Ca cell was a PCE of 6.4% with a J_{sc} of 13.7 mA/cm^2, a Voc of 0.729 V and a FF of 0.64 for a blend thickness of 82 nm. The maximum value for the J_{sc} in this later case was obtained for blend thickness of 105 nm. In that case, the numerical computation predicted a J_{sc} of 14.6 mA/cm^2 while the experimentally measured J_{sc} was 14.8 mA/cm^2. In all such cases the J_{sc} measured were lower than all the values measured for the cells with a BCP buffer layer of 3.5 nm.

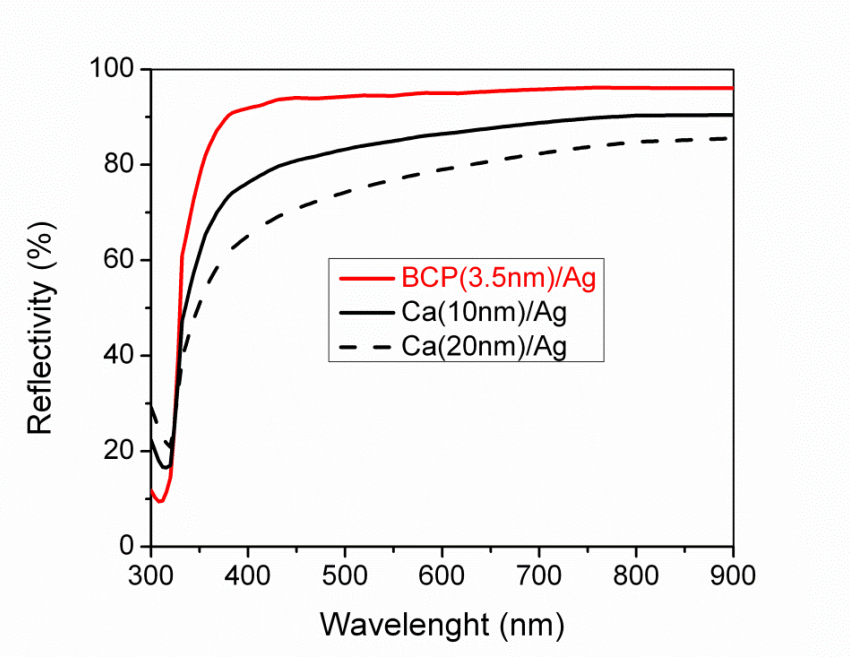

Figure 3.5. Calculated reflectivity of the electrodes Ca(20nm)/Ag(100nm) (black dashed line), Ca(10nm)/Ag(100nm) (black solid line) and BCP(3.5nm)/Ag(100nm) (red solid line) on top of fused silica.

A closer look into the numerical prediction and experimental data shown in figure 3.3 indicates that the combined thickness of the active layer and buffer layer also plays a determining role in the final performance of the organic photovoltaic (OPV) device. A contour plot of the J_{sc} in terms of the BCP and active layer thicknesses is shown in figure 3.6. We observe that ideally the best cell performance would be obtained for an infinitesimal thickness for the BCP layer while the thickness of the active layer should be roughly between 95 and 110 nm. As the thickness of the BCP layer is increased one must reduce the thickness of the active layer. This behavior is confirmed experimentally with the results reported in figure 3.3. For a BCP layer of 3.5 nm, when the active layer changes from 85 to 105 nm, the J_{sc} increases. A maximum value is obtained close to 100 nm and beyond that thickness J_{sc} decreases. On the contrary, when the BCP layer is 10 nm, and the active layer increases from 90 nm to 105 nm, the J_{sc} exhibits a slight tendency to decrease. Such changes in the behavior of the J_{sc} when the buffer layer has a different thickness can be correlated to redistribution of the

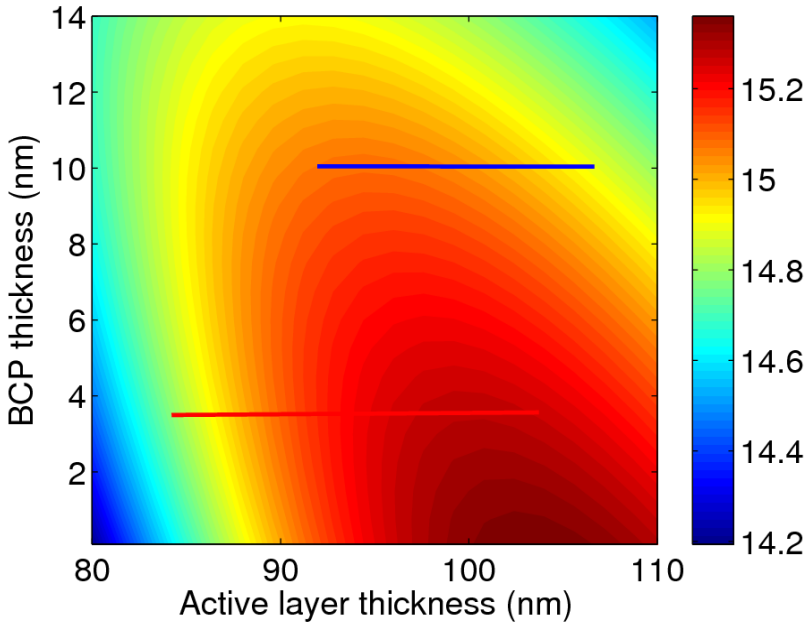

Figure 3.6. Contour plot of the numerically calculated J_{sc} as a function of the BCP and active layer thicknesses. The red and blue lines indicate the regions of the curve that have been tested experimentally (red and blue squares in figure 3.3).

energy absorption as a function of the wavelength. Indeed, in the numerically computed EQEs, shown in figure 3.7, we clearly see such redistribution of the energy absorption which can be linked in that case to the real part of the refractive index through the optical thickness and not to the extinction coefficient. The experimentally measured external quantum efficiencies for the same devices are shown in figure 3.7. As can be seen, similar EQEs around 65% are obtained in the region between 550 and 700 nm. The main difference between a BCP layer of 3.5 nm or 10 nm is seen in the region between 380 nm and 550 nm, where at 520 nm a maximum of 69% EQE is achieved when employing 3.5 nm of BCP. The EQE difference in that region can be accurately reproduced by the numerical model, confirming that the optical material properties, as well as, the optical thickness of the buffer layer plays a determining role in the final shape of the EQE. Note that the integration of the EQE spectra under the AM1.5G solar spectrum yields J_{sc} values that are consistent with the ones obtained from the J-V measurements reported in table 3.1.

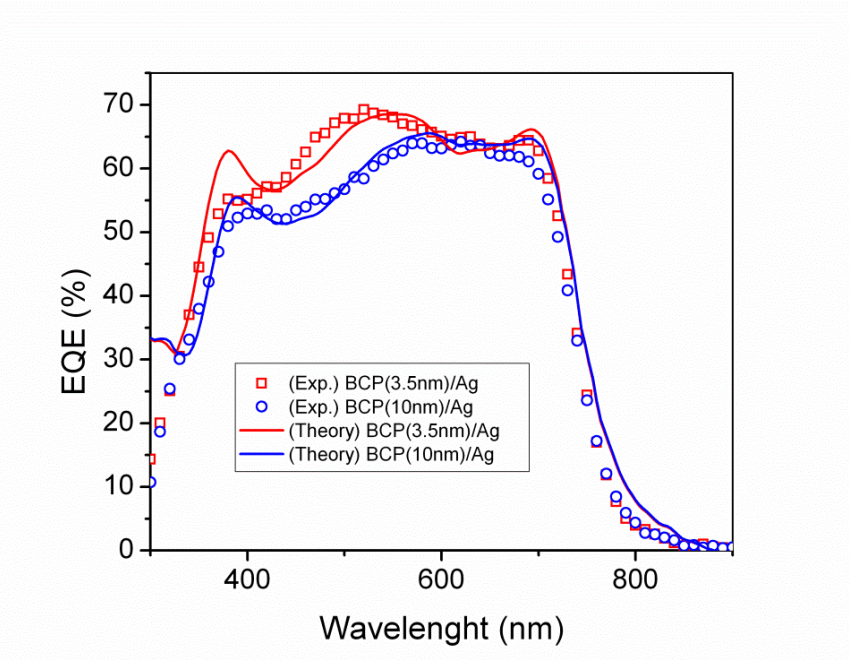

Figure 3.7. Experimentally measured (squares and dots) and numerically computed (solid lines) external quantum efficiencies for the BCP/Ag devices showed in figure 3.2. Showing in red the values for a BCP thickness of 3.5 nm and in blue for a BCP thickness of 10 nm.

It is apparent from table 3.1 and when comparing the previously reported Ca/Al [66] relative to the BCP/Ag cell parameters, that for the PBDTTT-C case, the incorporation of the BCP layer not only brings an optical improvement but also an electrical improvement providing a more balanced charge transport in the cell. Similar improvements in the electrical behavior of the cell were reported by Zhicai He *et al.* when they simultaneously increased V_{OC}, J_{sc} and FF in polymer solar cells by introducing poly [(9,9-bis(3´-(N , N - dimethylamino) propyl)-2,7-fluorene)- alt -2,7-(9,9–dioctylfl uorene)] (PFN) as a novel ETL interlayer in BHJ solar cells [14]. For the parameters that are not be directly linked to light harvesting efficiency, in the case of the BCP/Ag device studied here, the V_{OC} increased 2.4% while the FF increased 5.9% relative to previously reported results of Ca/Al cells. The sum of all improvements leads to a top PCE of 7.5% that represents approximately a 17% increase with respect to average 6.4% PCE reported in previous works that also used PBDTTT-C direct cells [66,68,69].

To confirm the general character of such optically enhanced construction, we fabricated devices comprising a blend containing PTB7 as the donor material. An ITO/PEDOT:PSS/PTB7:PC_{71}BM/BCP(3.5nm)/Ag device yielded a PCE of 8.1% (figure 3.8). As reported in table 3.2, when compared to the reported values (see reference [15]) a 7% gain in short-circuit current density and a 9% gain in PCE was achieved. We measured the extinction coefficient and refractive index for the PTB7:PC_{71}BM blend to numerically compute the expected EQE and J_{sc}. As shown in table 3.2, the predicted enhancement in J_{sc}, when using an ETL layer of 3.5 nm of BCP instead of Ca, agrees well with the experimentally measured improvement in J_{sc}. On the other hand, the improvement of the parameters not directly linked to light harvesting was 1% for the V_{OC} and 2% for the FF. This indicates that the optical optimization can be applied for different polymer blends, and that an enhanced light harvesting is also responsible for the larger part of the gain in PCE.

Table 3.2. Device characteristic parameters of the PTB7:$PC_{71}BM$ optimized solar device employing BCP as ETL. Numerically predicted short-circuit current density is indicated as J_{sc} theory.

	J_{sc} theory (mA/cm^2)	J_{sc} experimental (mA/cm^2)	V_{oc} (mV)	FF (%)	PCE (%)
BCP(3.5nm)/Ag	15.2	15.5	748	69.9	8.1
Ca(10nm)/Al [15,70]	-	14.5	740	68.9	7.4

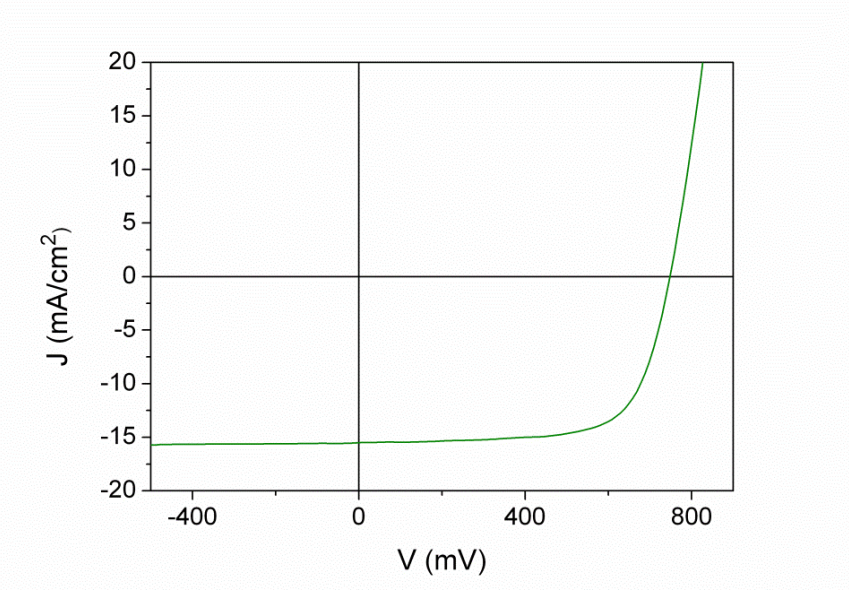

Figure 3.8. J-V curve for the best device based on a PTB7:$PC_{71}BM$ blend.

3.2 Optical role of the hole transporting layer

Here we consider a P3HT:PCBM BHJ solar cell to study the optical behavior of the the HTL. The commonly used PEDOT:PSS layer is replaced by a 5 nm thick layer of NiO as hole transporting layer. Recently, it was shown that NiO deposited by pulse laser deposition could be used effectively to replace the PEDOT:PSS layer [20]. The performance of an encapsulated NiO cell was shown to be very good in comparison to the PEDOT:PSS one. A good performance has also been achieved when the NiO is sputtered in an oxygen atmosphere [71]. Despite the fact that the stoichiometry of the

original NiO target may not be as well preserved in a sputtering deposition under an Ar:O_2 flow, here we show that the cells fabricated with the NiO layer sputtered in such conditions outperform the PEDOT:PSS layer cell in all the photovoltaic characteristic parameters except for the V_{oc}. All the fabrication steps that involve the processing of the organic materials were performed in ambient air.

The structure we studied was ITO/HTL/P3HT:PCBM/$LiCoO_2$/Al where the hole transporting layer (HTL) was either a PEDOT:PSS or NiO layer. The initial numerical analysis showed important optical differences between both devices as seen in figure 3.9. For the most effective photon harvesting, in both cases the predicted optimal thickness for the HTL was as infinitesimal thickness irrespective of the active layer thickness. However, experimentally this is strongly limited for the PEDOT:PSS layer which must be always thicker than 30 nm in order to keep good electrical properties [72]. For NiO layer this limitation is weaker and the layer can be as thin as 5 nm.

As mentioned before, the architecture of the two types of OSC devices we fabricated was only differing in the hole transporting layer which we used, either a PEDOT:PSS or a NiO layer deposited on top of the ITO electrode layer. The entire device handling

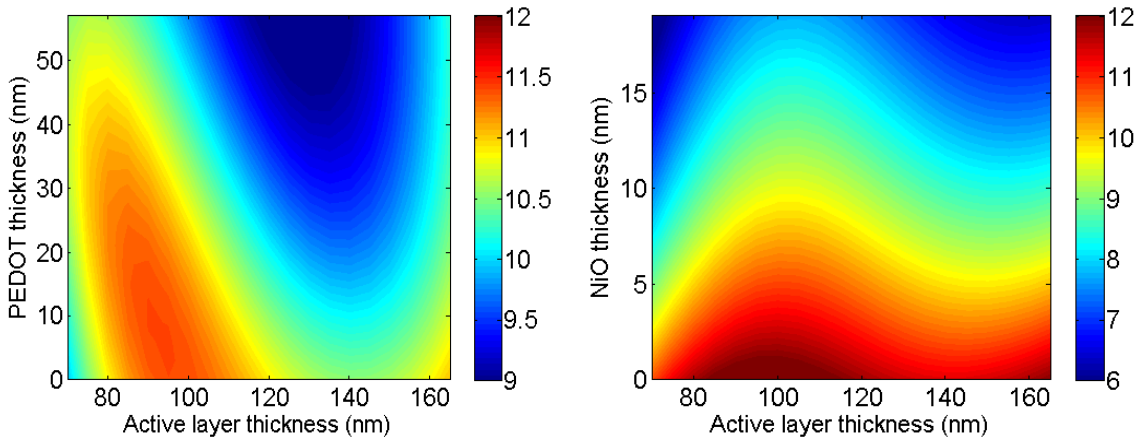

(a) (b)

Figure 3.9. Short-circuit current density contours as function of the thickness of the active layer and (a) PEDOT:PSS layer or (b) NiO layer.

(during fabrication) and deposition of all organics for both photovoltaic devices was performed in ambient air conditions. The first step of such fabrication was cleaning the ITO substrates in a sonication bath using several organic solvents, followed by an annealing to dry out solvents residues and UV/Ozone bath to eliminate any remaining organic residues. The measured sheet resistance was 20.69 Ω/sq. In the PEDOT:PSS cell, a 40 nm PEDOT:PSS layer was deposited by spin coating from a water-based solution. This thickness was the minimum we achieved with the spinner at its maximum rotation speed. Afterwards the sample was annealed at 120°C in air to eliminate the remaining water.

For the NiO cell, a 5 nm NiO layer was deposited by reactive sputtering. As mentioned above, the use of NiO as hole transporting layer was recently explored using pulsed laser deposition [20]. In the current work, we employed a sputtering process which would be more easily applicable in a large scale production of the organic photovoltaic devices [73,74]. To compensate for the presence of Ar which is necessary to maintain

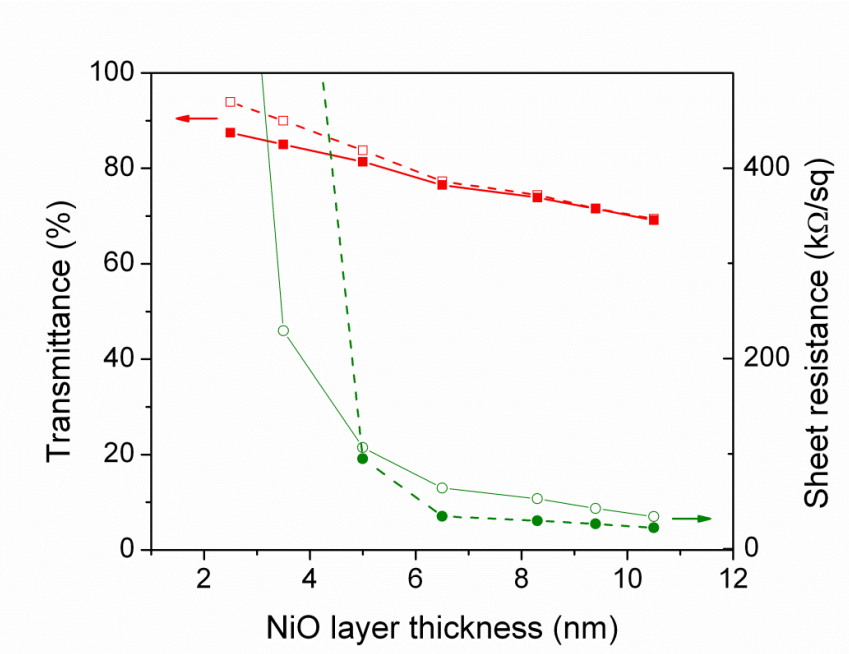

Figure 3.10. NiO Sheet resistance (circles) and average transmission (400-650 nm) (squares) as a function of the layer thickness. Solid lines correspond to pristine NiO and dashed lines correspond to the same layers after the plasma biasing and thermal annealing processes.

the plasma but may modify the stoichiometry of the NiO lattice, we sputtered the NiO layer under the presence of O_2 in an Ar:O_2 flow ratio of 20:10 (units in sccm). Additionally, it was also shown in reference [20] that the p-semiconducting character of the NiO is enhanced when the layer has a more polycrystalline character rather than a monocrystalline one. This is more easily achieved when the sputtering deposition is performed at room temperature [75]. Under the conditions described above, we grew different layers whose thicknesses ranged from 2.5 to 10 nm. Finally, an O_2 plasma bias treatment was applied to all the NiO layers grown in order to increase its optical transmittance and decrease its sheet resistance. In figure 3.10(a), it is seen that the average transmission value in the range from 400 to 650 nm decreases as the NiO layers thickness is increased. Such average transmission did not show any important differences after applying the plasma biasing or thermal annealing procedure. When the NiO layer thickness was under 4 nm, the sheet resistance, also shown in figure 3.10(a), was seen to exhibit a dramatic increase that went up to 900 kΩ/sq for the thinnest sample measured. For NiO layers which thickness was larger than 5 nm the sheet resistance was seen to be less than 100 kΩ/sq.

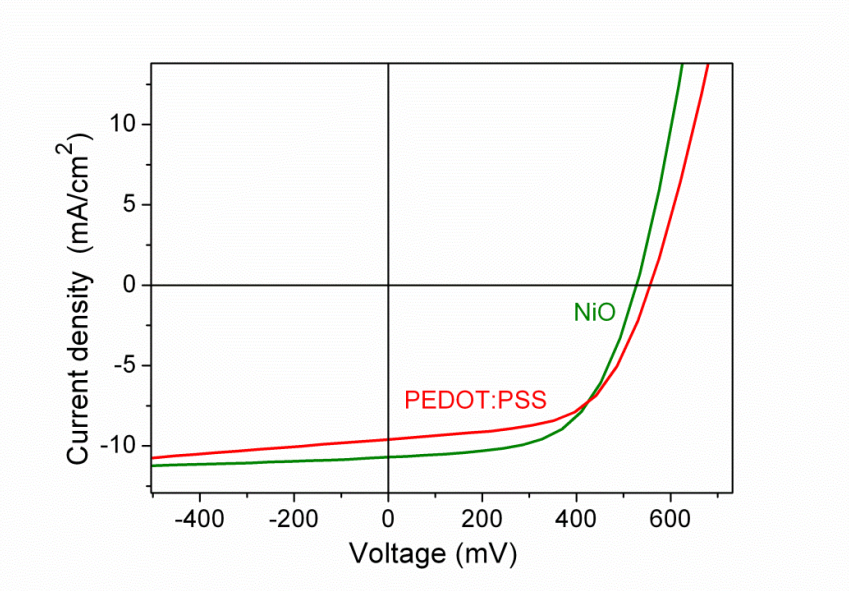

Figure 3.11. Current density–voltage curves after fabricated for ITO/HTL/P3HT:PCBM/$LiCoO_2$/Al where the HTL corresponds to NiO (green line) or PEDOT:PSS (red line).

An electrical characterization of the fabricated devices was performed under AM1.5G illumination. The J-V curve of a device fabricated with a layer of 5 nm of NiO is shown in figure 3.11. As seen, PCE of 3.3% was obtained in a highly reproducible procedure which, as already mentioned, was performed in ambient air. For comparison, the J-V curve corresponding to the best PEDOT:PSS device fabricated in the same conditions is also shown in figure 3.11. All the device parameters obtained from the J-V curves are summarized in table 3.3. As it can be seen in table 3.3, when the measurement is performed right after the last step of the fabrication, the NiO device already outperforms the PEDOT:PSS device in all parameters except for the V_{oc}.

Table 3.3. Electrical data for NiO and PEDOT:PSS devices

	J_{sc} (mA/cm^2)	V_{oc} (mV)	FF (%)	PCE (%)	Rs (Ω/cm^2)	Rsh (Ω/cm^2)
NiO	-10,62	520	59	3.31	84.4	8943
PEDOT:PSS	-9.56	556	57	3.14	322.1	9147

3.3 Optical metal cavity in the OPV architecture

As the last configuration in this chapter, we consider the replacement of the ITO electrode for a thin metal electrode that forms an optical cavity with the back metal electrode. As mentioned in the first chapter, an organic solar cell is formed by placing an active layer in between two electrodes. One of these electrodes must be semi-transparent for allowing the sunlight to enter the device and be absorbed in the active layer. This semi-transparent electrode is usually ITO and in this section it is replaced with a Cu-Ni bilayer metal electrode. Therefore the device is formed by an active layer sandwiched in between a metal cavity composed of the Cu-Ni bilayer and an aluminum electrode. The final characteristic photovoltaic parameters of the cell fabricated with the metal electrode are similar to those of the device fabricated with the Indium tin oxide (ITO). Despite the fact that the metal electrode exhibits a

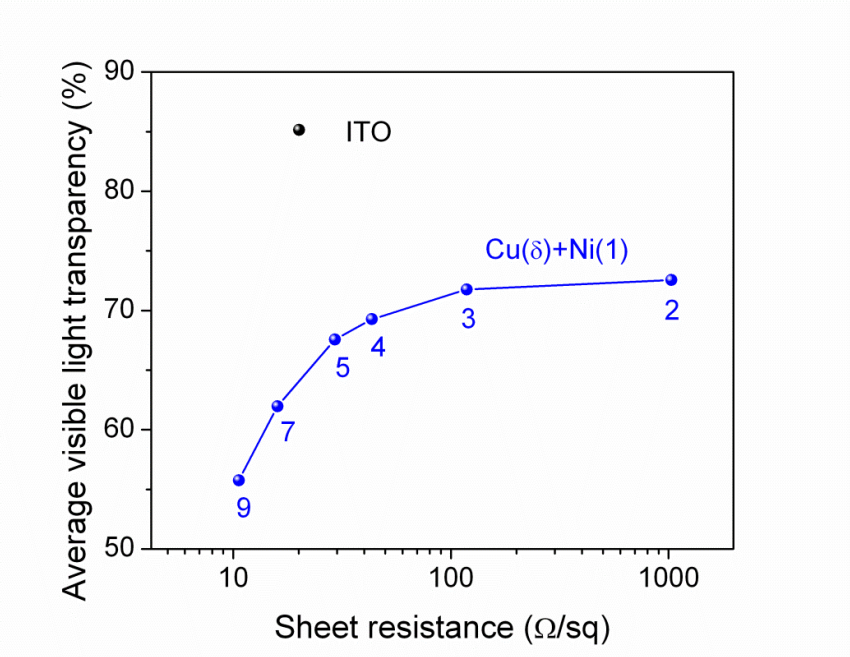

Figure 3.12. (a) Comparison of visible optical transparency of Cu(δ)+Ni(1) with ITO [76].

transparency that is 65% of the ITO electrode, the short circuit current for the metallic anode cell is 77% of the ITO cell, indicating that photon absorption could be enhanced by the optical cavity formed between the Cu-Ni and Al electrodes. The overall photo conversion efficiency for the metallic electrode cell is 76% of the ITO based one, which was measured to be 3.3%. The obtained performances of ultrathin metals when included in the cell architecture used here, combined with their low cost, high compatibility with other materials, and mechanical flexibility, confirm their potentials for OPV.

As indicated above, the materials selected for developing the metallic bilayer were copper and nickel. These materials were chosen to take into account the high electrical conductivity of the cupper and the high workfunction provided by the nickel layer considering that this is conceived as replacement for the ITO in the basic organic photovoltaic architecture. Therefore, in figure 3.12 the transparency and sheet resistance of Cu(δ)+Ni(1) bilayers are compared with the ITO films. It can be seen that the 1 nm Ni capping layer reduces the transmission by about 10 % without any

significant change in sheet resistance. This behavior can be explained in terms of refractive index matching and extinction coefficient difference of Ni and Cu. The Ni capping layer acts as a functional layer, which provides stability of the Cu films, which would otherwise easily oxidize, and a work function higher than that of the Cu film which suits the use for replacing ITO. We first optimized the deposition conditions to achieve the lowest sheet resistance for a given optical transparency. After that we have deposited films with different thickness of Cu. It is observed that the electrical properties are basically given by the underlying Cu ultrathin layer, provided it is continuous. The percolation threshold, i.e. the thickness corresponding to which the film becomes continuous, is found to be between 5.5 nm and 6.5 nm [77].

The organic solar devices were developed using the structure: Cu/Ni/NiO/P3HT:PCBM/$LiCOO_2$/Al where a 5 nm NiO layer was employed as hole transporting layer and a 0.45 nm $LiCoO_2$ layer as electron transporting layer. The J-V curves for the OPV devices incorporating Cu(δ)+Ni(1) and ITO electrodes are shown in figure 3.13 and the corresponding electrical characterization data are summarized in

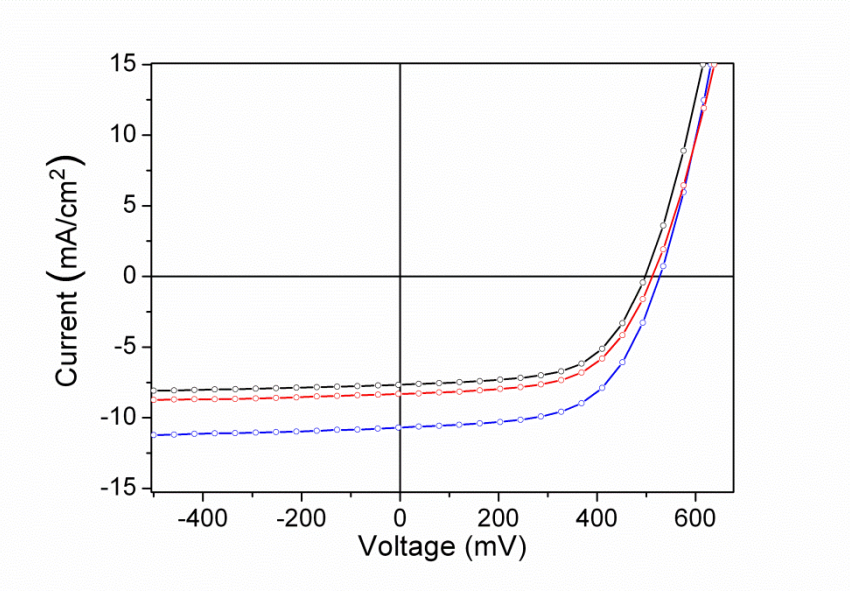

Figure 3.13. Current density–voltage plots for the OPV cells incorporating the Cu(9)+Ni(1) (●), Cu(9)+Ni(1) (●),and ITO (●). Schematic drawing of the device structure (inset).

Table 3.4. Electrical characterization data for the OPV device

	J_{sc} (mA/cm^2)	V_{oc} (mV)	FF (%)	PCE (%)	AVT (%)	Sheet resistance (Ω/sq)
Cu(7)+Ni(1)	-8.26±0.06	505±4	59±1	2.51±0.04	57	16
Cu(7)+Ni(1)	-7.60±0.05	500±2	59±1	2.28±0.04	51	11
ITO	-10.62±0.08	520±15	59±1	3.31±0.04	86	21

table 3.4. In all the devices, the values for open circuit voltage (V_{oc}) and fill factor (FF) are practically the same. The differences between the devices are related to changes in short-circuit current density (J_{sc}) which determines directly the efficiency of the final devices. The higher reflectance of the metallic bilayer shown in figure 3.14 gives rise to an enhanced photon absorption due to the formation of an optical microcavity between the Cu-Ni anode and the Al electrode [78,79] thus improving the optical efficiency of the device. Indeed, despite the fact that for the Cu(7)+Ni(1) bilayer the

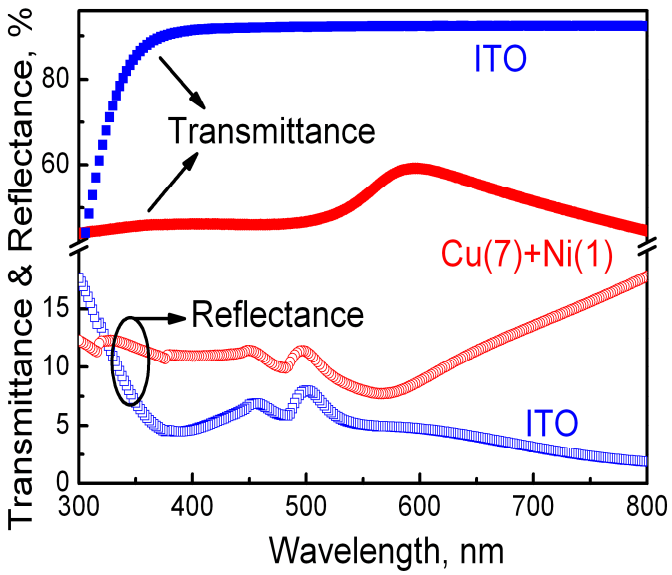

Figure 3.14 Comparison of transmittance and reflectance of Cu(7)+Ni(1) with ITO.

transmission is only 69% that of the ITO, the J_{sc} measured for such cell is 77.2% that of the ITO cell. A similar behavior is seen for the Cu(9)+Ni(1) case where the transmission of the electrode is 59% relative to ITO while its J_{sc} is 73.5%

3.4 Conclusions

In this chapter we have analyzed in detail the role played by the non-active layers of an OPV cell in optically controlling the final device short-circuit current. We considered separately the effect played by the ETl, HTL and semi-transparent electrode. Such study was developed by considering three different types of cells where the optical performance of each layer is analyzed by changing their optical constants and/or thicknesses.

We demonstrate that by a proper selection of the imaginary and real parts of the refractive index of the ETL, light harvesting can be largely enhanced. We performed a numerical calculation of the light harvesting efficiency which demonstrated that a reduced extinction coefficient (k) for the ETL is essential to achieve a cell architecture that exhibits an optimal light absorption by the active layer. In accordance, we replaced the commonly used back electrode composed of a thin 10-20 nm Ca layer and a thicker Al layer by a few nanometer thick bathocuproine layer and a thick Ag layer. This enhanced the reflectivity of the buffer layer/electrode back contact which resulted in an increase of the short circuit current. Light harvesting could be further improved by adjusting simultaneously the thickness of both the BCP and the active layer to achieve an optimal optical interference. Such tuning of k combined with an effective tuning of the optical path associated to the real part of the refractive index n, through a thickness change, implied up to an 8% increase in short circuit current. In addition, we observed that when using the BCP/Ag electrode, the photovoltaic parameters of the cell not directly related to photon harvesting such as the V_{OC} and FF also improved. Taking advantage of the optical optimization and the slight improvement in the electrical properties, we were able to fabricate cells of PBDTTT-C with PCEs of 7.5%

and PTB7 cells with PCEs of 8.1% which confirmed that the optical properties of the ETL adequately combined with the optical characteristics of the active layer are essential to achieve high performance thin film OPV devices. We demonstrated the general character of the optically enhanced architecture we studied by applying it to two different kinds of low band gap light absorbing materials. Indeed, such optical enhancement is based on the basic material and structural parameters that control light propagation within thin film cells and should be applicable to other kinds of thin film electrical devices which are meant to sense, detect or generate light.

In the second part of this chapter, we fabricated air-processed organic solar cells by including a sputtered NiO layer to replace PEDOT:PSS as hole transporting layer. In such case, we concluded that irrespective of the thickness of the active layer, the optimal optical interference to enhance the photon absorption is obtained when the thickness of the HTL is reduced to a minimum. The limitations on the thickness reduction are, in general, not optical but determined from the electrical performance of such layers

In the final part of the chapter, low cost ultrathin Ni capped Cu metallic bilayers have been proposed to achieve highly transparent and electrically conductive electrodes. Given the optical microcavity effect seen and provided that the optical to electrical performances of the bulk hetero-junction P3HT:PCBM fabricated cells are similar to those obtained with ITO electrodes, the results obtained confirm that semi-transparent metallic based electrodes are an effective alternative to transparent conductive oxides.

Chapter 4

Photonic control in semi-transparent OPV devices

It has been recognized by many authors that the intrinsic semi-transparency of the active material found in many OPV devices [80–106], opens the door for integration of OPV cells in transparent elements, such as windows in buildings or automobiles. Ideally, such OPV windows should exhibit a transparency close to the transparency of the window without including any PV system. The required transparency strongly depends on the application but, for windows in the south façade of commercial buildings in northern hemisphere countries, the typical visible light transmission that provides the adequate human photo-protection lies in the 20-40% range [107].

In many donor or acceptor organic materials, the low charged carrier mobility prevents, in general, the use of thick active layers that would be needed for a very efficient photon harvesting. However, such low charge mobility and the resulting associated semi-transparency of the active layer may turn out to be the strongest asset for OPVs to compete in the photovoltaic production of electrical energy. In a common OPV device, the active layer semi-transparency cannot be used because such device is capped with a metal layer that, as explained in chapters 2 and 3, serves a double purpose: as one of the electrodes of the cell and, as mirror to reflect back into the device photons that have not been absorbed during the first path. It has not been until recently, that semi-transparent top electrodes have been fabricated with similar

electrical properties as the ones which are deposited directly on the substrate [18,108–113]. To re-harvest infrared or UV photons that are lost in semi-transparent devices requires either additional changes in the cell architecture or the use of materials with an enhanced absorption in the UV and especially in the near IR. A combination of a Bragg reflector and an anti-reflective coating have been used to increase near IR photon harvesting demonstrating that the efficiency of small molecule OPV cells could be increased from 1.3% to 1.7% [114]. An alternative option to re-harvest red light considered the use of cholesteric liquid crystals as wavelength dependent reflectors [115]. Enhancing near IR photons harvesting is also possible by considering donor polymers with an absorption band IR shifted close to 800 nm. Following such strategy a rather significant breakthrough in semi-transparent OPVs was achieved recently when a power conversion efficiency (PCE) above 4% was reported [116,117]. The use of high performance polymers or tandem cells has also been considered in semi-transparent cells [118–120]. In that case, either efficiencies above 5% can be achieved at the expense of a rather limited luminosity, or high transmission in the visible is obtained at the expense of a reduced near IR photon harvesting which eventually limits the overall efficiency of the device. An approach that combines high performance

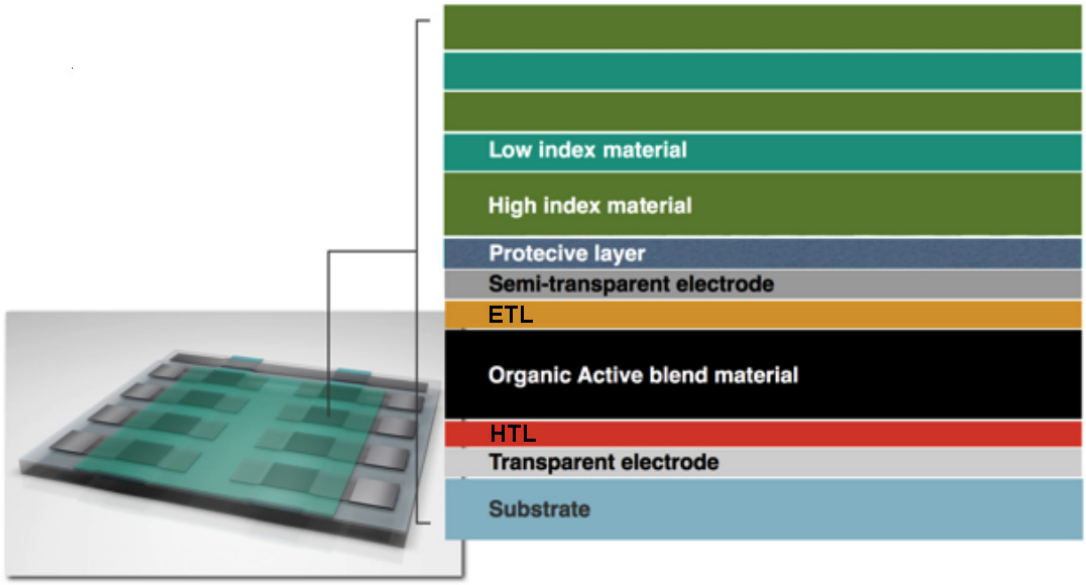

Figure 4.1. Schematic architectures for a semi-transparent cell including the designed photonic structure.

polymer PV materials with a photonic configuration to re–harvest UV and near IR photons when the top electrode is thinned down, is needed to take the PCE of visibly transparent cells to the high limit efficiencies that were recently established based on the Schokley-Queisser theory [121]. When the mirror effect of the back electrode is removed to obtain a semi-transparent cell, a photonic management becomes essential. The simple use of a Bragg reflector to reflect the IR and transmit the visible would not produce the optimal result. A periodic multilayer optimizes the interference to get maximum reflectivity at the wavelength that satisfies Bragg condition. In a photovoltaic device interference must be the optimal one at each wavelength of the portion of the solar spectrum being absorbed by the active material.

4.1 One-dimensional photonic structure integration

In the current chapter, we consider the design and integration of a five layer photonic structure (schematic in figure 4.1) that provides an optimal interference at each wavelength to obtain the largest efficiency, while, at the same time, maintains a very good transparency in most of the visible wavelengths. The goal for such photonic structure is to localize the IR and UV parts of the sunlight spectrum inside the cavity formed around the active layer. The photonic control provided by such photonic structure is also employed for tuning the color transmitted by the semi-transparent organic photovoltaic (STOPV) device. As we will see below, the visible transparency for the STOPV devices under consideration is close to 30 % or higher, which is, as indicated above, well within the range of expected transparencies for south façade windows in commercial buildings.

We consider two types of reference devices, which we name Tk-Ag and Tn-Ag standing for the opaque device using thick silver and the single semi-transparent device using thin silver, respectively. Both references are used for comparison with the STOPV device including the photonic structure which is a multilayer stack of MoO_3 and LiF as shown in figure 4.1. The active material considered in all cases is a 90 nm

thick bulk hetero-junction of a PTB7:$PC_{71}BM$ blend. The architecture of these two cells, shown in figure 4.1, is the same except for the thickness of the top silver electrode and a protective LiF thin layer for the Tn-Ag. For the Tk-Ag the thickness of the evaporated Ag electrode is 100 nm while for the Tn-Ag cell the thickness for the top electrode is 10 nm. As mentioned before, to prevent a rapid degradation of the 10 nm silver layer, the Tn-Ag cell includes 15 nm of LiF, this extends several hours the lifetime for such non-encapsulated device.

In order to enhance the light harvesting efficiency in the Tn-Ag device, without loosing transparency in the visible range, ideally one would like to have a perfect mirror for the near IR and UV and zero reflectivity in the visible. It is well known that photonic crystals offer the possibility to tailor light propagation. However, a large degree of light management by photonic crystals is, typically, only achieved when a two or three dimensional structuration of the refractive index is implemented. Such kind of structuration may be not desirable in solar cells for several reasons. An alternative option, which has proven to be quite efficient, is to consider one-dimensional structures but incorporating an additional degree of freedom by removing

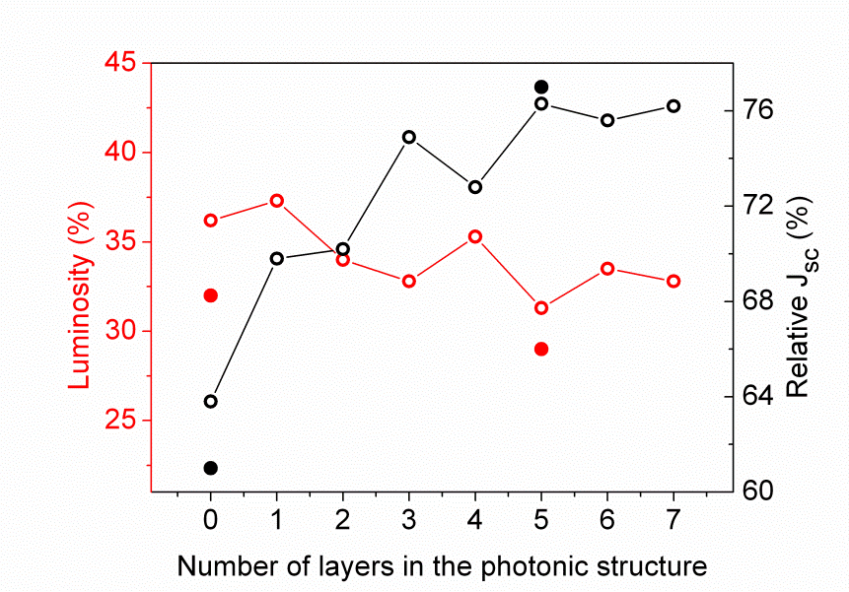

Figure 4.2. Calculated correlation of the relative J_{sc} and luminosity (see appendix B) of the STOPV device with the number of layers in the integrated PC. Experimental data is indicated in solid points.

the periodicity inherent to photonic crystals [123]. The practical implementation of this option, typically, requires the application of inverse integration methods that find the optimal design for the layer structure based on the effect one wants to reach. Given the simplicity of the layer architecture of an OPV cell, the option we have chosen here, is to compute the outcome of all possible solutions within a given range of parameters that may include, number of layers, thickness, index of refraction for all layers and then numerically select the solution that best matches the objective, which is set in terms of one or several variables, such as the short circuit current, average transparency at a given wavelength range, color or luminosity of the devices.

For a STOPV window there are essentially two parameters that will determine its performance. One is the efficiency in converting light to electricity (PCE) and the other is the transmission at wavelengths to which the eye is sensitive, the luminosity. In our numerical calculation we sought for the photonic nano-layer design that maximized the contribution to the J_{sc} for wavelengths below 400 nm and above 650 nm and which luminosity was at least 90% that of the Tn-Ag cell. As can be seen in figure 4.2, the J_{sc} increases rapidly when we increase the number of layers in the

Table 4.1. Predicted effect of photonic structures, employing up to 7 layers, on the Tn-Ag device.

Device	**Photonic structure**							**Relative performance**		
	MoO_3 (nm)	**LiF (nm)**	**MoO_3 (nm)**	**LiF (nm)**	**MoO_3 (nm)**	**LiF (nm)**	**MoO_3 (nm)**	**%J_{sc}**	**%L**	**%AVT**
PC(7)-Tn-Ag	102	136	102	102	102	136	102	76.2	32.8	32.5
PC(6)-Tn-Ag	102	136	102	102	102	34	0	75.6	33.5	32.6
PC(5)-Tn-Ag	136	102	102	136	102	0	0	76.3	31.3	29.9
PC(4)-Tn-Ag	136	68	102	34	0	0	0	72.8	35.3	35.1
PC(3)-Tn-Ag	102	136	102	0	0	0	0	74.9	32.8	32.6
PC(2)-Tn-Ag	102	68	0	0	0	0	0	70.2	34	36.1
PC(1)-Tn-Ag	136	0	0	0	0	0	0	69.8	37.3	36.7
Tn-Ag	0	0	0	0	0	0	0	63.8	36.2	37.1
Tk-Ag	0	0	0	0	0	0	0	100	0	0.1

photonic structure (PC) and it saturates beyond 5 layers. As seen in table 4.1, while the J_{sc} for the Tn-Ag cell is 64% of the Tk-Ag cell, the J_{sc} calculated for the PC(5)-Tn-Ag cell is close to 76% that of the Tk-Ag cell. As it is described below, the PC combines layers of LiF with layers of MoO_3. As shown in figure 4.3(a), when we compare the calculated external quantum efficiency of the PC(5)-Tn-Ag and Tn-Ag cells we observe that contributions to current from the IR as well as UVA photons are clearly enhanced for the PC(5)-Tn-Ag device. For certain IR photons the EQE for the PC-Tn-Ag is enhanced to even match the EQE of the Tk-Ag cell. On the other hand, contribution from visible photons remains similar to the contribution that we obtain from such photons for the Tn-Ag cell.

From the solutions we found that maximize J_{sc} in the specified range, we selected a subset of solutions with a luminosity higher than 90%, the one from the Tn-Ag cell. As can be seen in figure 4.2, the luminosity for the PC-Tn-Ag devices ranges from 36% for the cell with no PC to 32% for the cells that incorporate a PC with five layers or more, which exhibit the highest currents. As shown in figure 4.3(b), the calculated transmission for the Tn-Ag and PC(5)-Tn-Ag cells are in the 30 to 45% range for most of the visible wavelengths. However for the UVA and near IR wavelengths, the predicted transmission is below 10% for the PC-Tn-Ag while it stays above 30% for

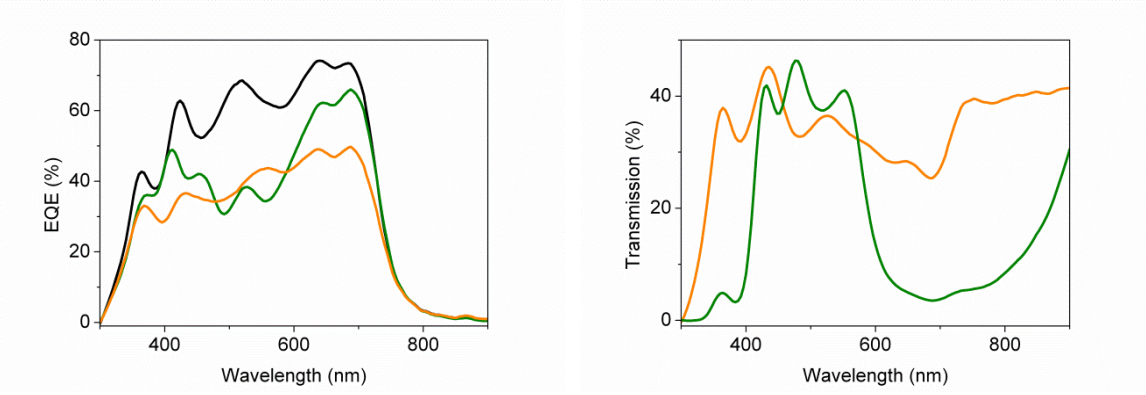

(a) (b)

Figure 4.3. Numerically calculated (a) EQE and (b) transmittance for the Tn-Ag (orange solid line), Tk-Ag (black solid line) and PC(5)-Tn-Ag (green solid line)

the Tn-Ag cell.

The photonic crystal grown on top of the solar cells has to be developed by depositing a combination of two transparent thin film materials with low and high refractive index. The main concern when applying such type of fabrication is the damage that could be infringed to the already deposited layers underneath. Particularly, the Ag transparent electrode and organic films are sensitive to radiation, charging, heating and solvents depending on the deposition method used (magnetron sputtering, thermal evaporation, spin coating, etc…). Taking into account such considerations above, we fabricated a one-dimensional photonic crystal based on MoO_3 (n ~ 2.1) and LiF (n ~ 1.4) (Appendix A) which can provide the necessary index contrast to obtain the desired photonic trapping effect. Both materials were deposited by thermal evaporation. The procedure followed infringed a very limited degradation to the parameters of the cell such as FF and V_{oc} which are weakly dependent on the light harvesting capacity. Indeed, as seen in table 4.2, the V_{oc} went from 724 mV to 716 mV, while the FF dropped from 71% to 68%. We observed that the FF and V_{oc} are significantly better for the PC(5)-Tn-Ag cell when compared to the Tn-Ag cell. This, however, should be attributed to a rapid degradation of the Tn-Ag cell, which is not protected from oxygen or moisture by the photonic structure. The experimentally measured EQEs for the cell including the PC structure are compared to the two

Table 4.2. Electrical and optical characterization parameters for the Tk-Ag, Tn-Ag and PC(5)-Tn-Ag devices.

Device	**Characterization parameters**					**Relative performance (experimental/theoretical)**		
	J_{sc} (mA/cm^2)	J_{sc}-EQE (mA/cm^2)	V_{oc} (mV)	FF (%)	PCE (%)	$\%J_{sc}$	%L	%AVT
Tk-Ag	14.0	14.9	724	71	7.3	100/100	-	-
Tn-Ag	8.5	8.9	688	61	3.6	61/64	32/36	33/37
PC(5)-Tn-Ag	10.7	11.4	716	68	5.2	77/76	29/31	27/30

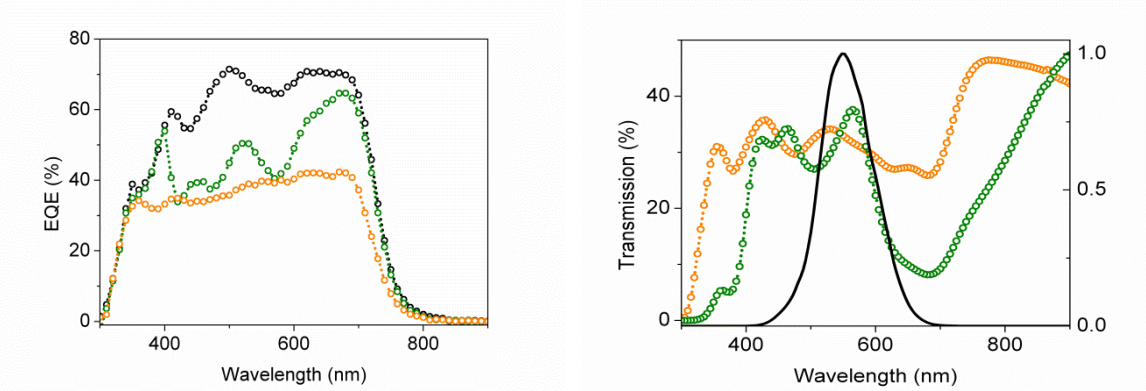

(a) (b)

Figure 4.4. Experimentally measured (a) EQE and (b) transmittance for the Tn-Ag (orange symbols), Tk-Ag (black symbols) and PC(5)-Tn-Ag (green symbols). The product of the Photopic response and the D65 illuminant is plotted (black solid line) for remarking its good fitting with the PC(5)-Tn-Ag transmission spectrum.

reference cells in figure 4.4(a). As seen, the capacityfor the PC to trap IR and UVA light is remarkable and is in very good agreement with the theoretical prediction shown in figure 4.3(a).

The trapping for the UVA is very effective and the J_{sc} resulting from wavelengths in the 300-400 nm range corresponds to 98% of the opaque cells. For the IR wavelengths in the 650-900 nm range the J_{sc} corresponds to 91% of the opaque cell. As indicated, the PC structure is a non-periodic alternation of low and high index of refraction layers which thickness is close to 100 nm. Relative to the Tn-Ag cell, the increase in J_{sc} is close to 26%. This could not have been achieved with a periodic structure consisting of five layers only, demonstrating the relevance of increasing the degrees of freedom to reach a high level for tailoring the external quantum efficiency to the desired result. It is important to note here again, that the optical extinction coefficient or absorption of the active material plays a secondary role in the final form for the EQE. Indeed, all three types of cells use a layer of the same thickness of PTB7:$PC_{71}BM$ while exhibiting EQEs with significantly different features.

4.2 Color tunable organic photovoltaic devices

As shown in figure 4.5, the extinction coefficient for the PTB7:$PC_{71}BM$ blend stays close to 0.2 without exhibiting any pronounced features in the visible range. Consequently, when looking through a 90 nm layer of such blend, one does not perceive any change that would significantly alter the color of any kind of image behind. In fact, the only visual effect of such blend to the image being observed through it is a reduction in the light intensity received by the eye. When combining such fairly flat transmission with the photonic layer structure, we have the possibility to broadly tune the color of the device with a limited effect on the PCE.

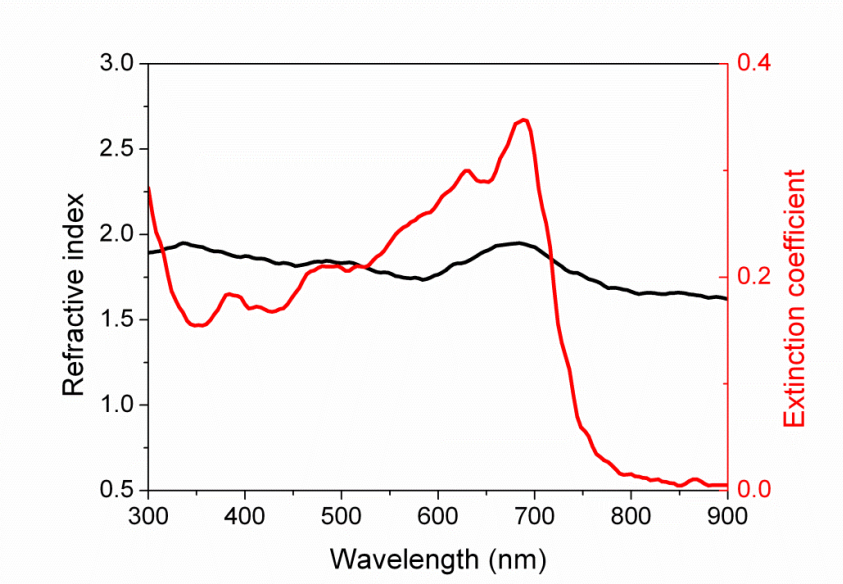

Figure 4.5. Complex refractive index for the PTB7:$PC_{71}BM$ active layer

The procedure followed to tune the color of the device is similar to the one we followed to obtain the best performance devices with the highest luminosity. Here we enlarge the set of possible solutions to include all combinations, within the range of optical parameters specified, that lead to a short circuit current larger than 70% of the Tk-Ag cell and a luminosity larger than 90% that of the Tn-Ag cell. Finally the

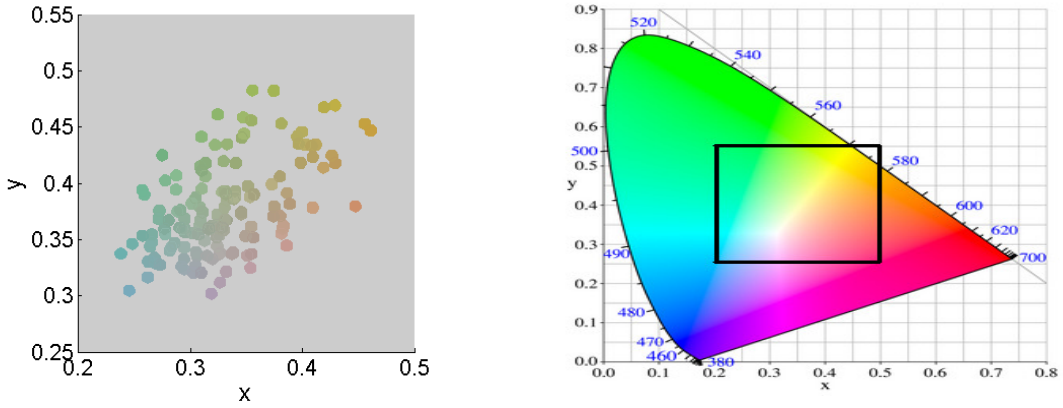

(a) (b)

Figure 4.6. (a) Predicted colors of the devices integrating the 5-layer photonic structure represented in the coordinates of the CIE 1931 x,y chromaticity diagram [126]. (b) The square in a) is shown on top of the complete CIE 1931 x,y chromaticity diagram.

transmitted color is calculated for all the resulting devices according to the process explained in Appendix B. The colors corresponding to the devices considered are arranged and plotted in figure 4.6(a) in terms of the corresponding color parameters of the CIE 1931 chromaticity diagram. Four different devices were selected for implementing experimentally the color tuning. The calculated structures are presented in table 4.3 and the expected transmission spectrum and EQE are shown in figure 4.7.

Table 4.3. STOPV devices architectures integrating a PC targeting specific transmitted colors.

Device	ITO (nm)	PEDOT (nm)	BHJ (nm)	BCP (nm)	Ag (nm)	LiF-Prot (nm)	MoO_3 (nm)	LiF (nm)	MoO_3 (nm)	LiF (nm)	MoO_3 (nm)
Reddish	330	30	90	3.5	10	15	136	34	34	34	102
Grayish	330	30	90	3.5	10	15	136	102	136	68	136
Bluish	330	30	90	3.5	10	15	34	34	68	136	102
Greenish	330	30	90	3.5	10	15	136	102	102	136	102

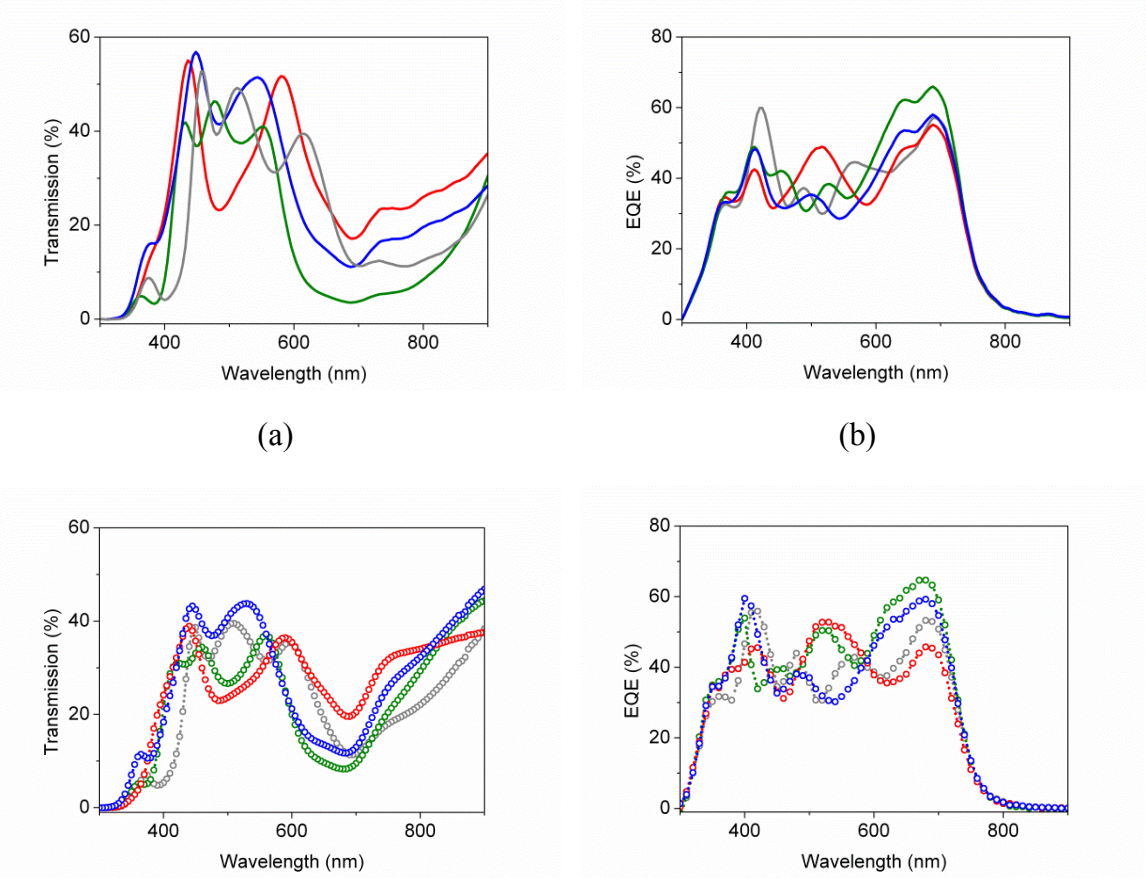

Figure 4.7. Theoretically predicted (a) transmittance and (b) EQE for the selected color tuned-STOPV devices. The corresponding experimental (c) transmission and (d) EQE agreed with the theoretical prediction.

Figure 4.8 is an actual photograph of the fabricated devices. A good correlation with the predicted color was found. As seen in figure 4.7(c), the blue and green devices exhibit similar transmission curves, except that the ratio between short and long wavelengths is slightly larger for the blue device. As seen in table 4.4 we measured the best light harvesting efficiency from these two devices, which is in accordance to an optimal harvesting of the IR and UVA photons, as can be seen in the EQE curves shown in figure 4.7(d). For the red device, transmission for long wavelengths increases which results in a less effective trapping for the IR photons. As expected, the EQE for the gray device is the one that shows the weakest wavelength dependence in the visible and IR intervals. To maintain the PCE above 4.5% for the grey device, the resulting

transmission, shown in figure 4.7(c), is significantly red shifted.

Figure 4.8. Experimental STOPV devices with color tuned transmission

Table 4.4. Electrical and optical characterization parameters for the color tuned STOPV devices.

Device	**Characterization parameters**					**Relative performance (experimental/theoretical)**		
	J_{sc} (mA/cm^2)	J_{sc}-EQE (mA/cm^2)	V_{oc} (mV)	FF (%)	PCE (%)	$\%J_{sc}$	%L	%AVT
Red	9.3	9.7	712	69	4.6	67/69	30/39	30/37
Gray	9.6	9.8	707	68	4.6	69/71	34/38	30/35
Blue	9.6	10.3	722	68	4.7	69/68	34/42	32/39
Green	10.7	11.4	716	68	5.2	77/76	29/31	27/30

4.3 Conclusions

In organic transparent cells, light harvesting diminishes because the reflectivity of the top layer is reduced and the device looses its capacity for photon trapping. Although

the capacity for photon trapping in any thin film solar device would always be limited, we have opened a path for light harvesting recovery when thinning down the top electrode. For the type of devices considered here, a semi-transparent top electrode implies that the light harvesting capacity is only 61% that of the corresponding opaque device. We demonstrate that the photon management provided by a one dimensional structure of five nano layers is sufficient to bring back the light harvesting capacity of the device to 77% that of the opaque cell. When such photon trapping was applied to high performance bulk hetero-junctions of organic PV materials, we fabricated close to 30% transparent cells with efficiencies above 5.6%. Breaking the 5% efficiency barrier with a high luminosity constitutes a major step towards the development of a semi-transparent PV technology. In a recent study of the theoretical efficiency limits of transparent cells it was determined that cells with a 30% luminosity have the potential to exhibit a PCE close to 88% that of the opaque cell.[42] Combining the photonic control proposed here with the use of red shifted absorption low band gap polymers we expect that the performance of semi-transparent cells may get very close such theoretical prediction. Finally, the results reported, which are essentially based on a photonic effect, have interest well beyond the photonics community. They open the door to design and fabrication of new types of PV modules with a large capacity to be incorporated in buildings as windows leading to a very good integration of electrical power generation sources in highly populated urban areas.

Conclusions

In the thesis we have applied different strategies to optimize photon localization inside OPV devices and, eventually, improve the performance of such cells. In chapter 2 we confirmed theoretically and experimentally that optical interference plays a very relevant role to enhance the overall performance of organic photovoltaic devices. We showed that a simultaneous adjustment of all the layers in an OPV device may lead to an EQE that matches the IQE for a large wavelength range. Such matching was achieved for the wavelength range where the absorption of the active material is larger. In addition, for the specific cell configuration considered in chapter 2, we demonstrated that by adjusting the optical interference, a given device could perform equivalently to a device whose active layer thickness was 1.7 times larger. From the results reported in chapter 3 we concluded that the optical constants of the cell charge blocking layers play a determining role in the final performance of the cell. Specifically, in donor-acceptor conjugated polymer cells, calcium was replaced by BCP as electron transporting layer. The parasitic absorption associated to the calcium layer was eliminated when using a thin layer of BCP whose extinction coefficient is practically zero for the entire visible and near IR spectrum. In a P3HT device, the most commonly used hole transporting layer, PEDOT, was replaced by a 5 nm NiO layer. Such thin NiO layer enabled a better localization of the field inside the active layer, helping to overcome one of the major limitations of the PEDOT which is that it cannot be made thinner than 30 nm preventing an optimal field localization in the active layer. Finally, in the same chapter we concluded that an optimal balance must be found between the transmission and reflectivity of the semi-transparent electrode. Metallic semi-transparent electrodes were used forma a cavity with the back electrode helping to localize the field in the active material.

In the last chapter of this thesis we applied the concepts which we considered in chapters 1, 2 and 3 to achieve a very effective photon management for semi-transparent cells. In such type of cells we achieved a maximum light transmission for the visible wavelengths combined with a maximum light localization for the near IR and UVA wavelengths. We demonstrated that this could be achieved integrating in the cell a one-dimensional multilayer photonic structure. While enhancing photon absorption in specific regions of the absorption spectrum of the active material, such photonic structure enabled the transmission at different colors without modifying the properties of the active material.

In summary, all the above-mentioned strategies led to a better photon harvesting resulting in an enhancement in the performance of OPV devices and demonstrating the key role played by optics to complement materials science-based research to achieve high performance organic solar cells.

Appendix A

Materials and methods

This chapter summarizes most of the materials and deposition methods used during the present thesis. Several different materials were evaluated in applied to organic solar devices which include organic active materials, buffer layers (semiconducting hole and electron transporting films) and electrodes including not just metals but transparent conductive oxides.

A.1 Deposition methods

Three basic deposition methods were employed depending on the materials characteristics; those were spincoating, magnetron sputtering (both RF and DC) and thermal evaporation.

The basic process for depositing organic and nanoparticle layers was spincoating in which a substrate is rotated while a liquid solution spread in its surface. The speed diagram of such process is shown in figure A.1(a). The second most employed deposition method was thermal evaporation often used for developing layer of metals such as aluminium, silver, gold, calcium or exciton blocking layers such as Lithium fluoride (LiF) or Molybdenum oxide (MoO_3). In this process a metal boat is heated in

high vacuum conditions and the process diagram is presented in figure A.1(b). For some organic layers such as Bathocuproine (BCP) the evaporation control was done by

(a)

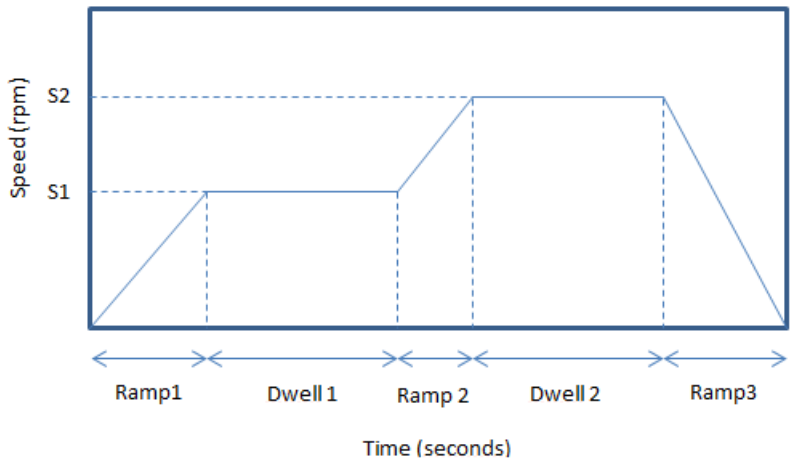

(b)

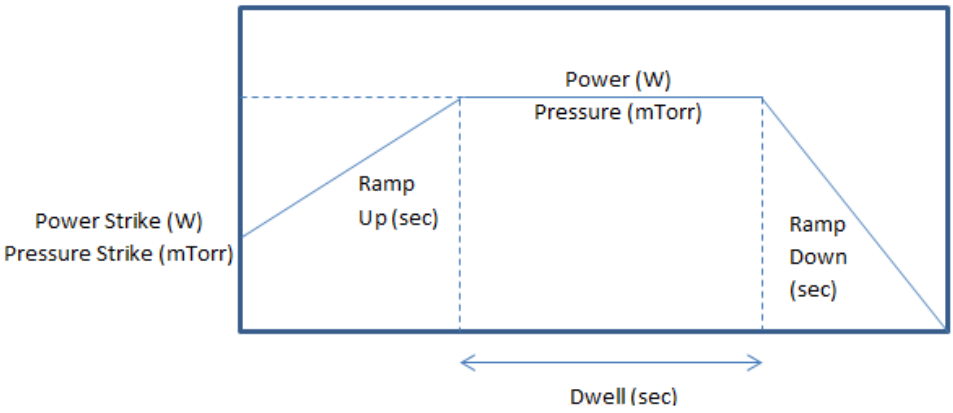

(c)

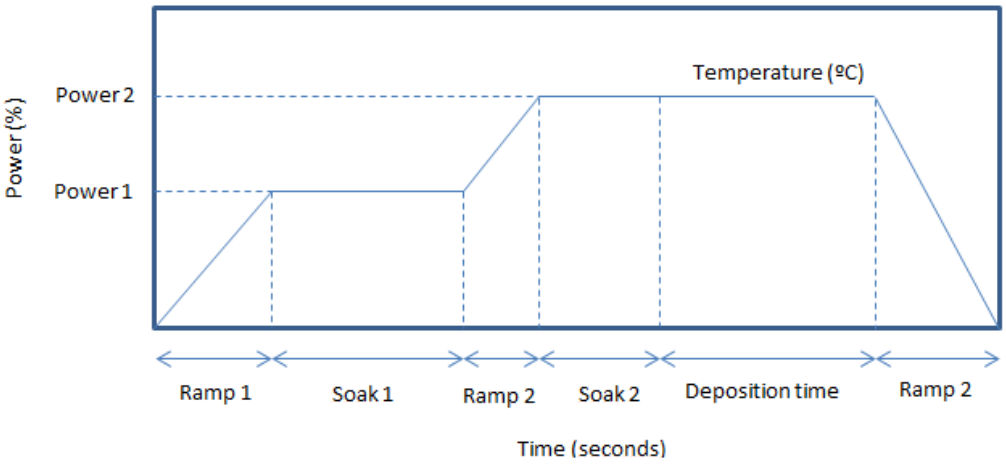

Figure A.1. Deposition methods diagrams employed (a) spincoating, (b) sputtering and (c) thermal evaporation

temperature instead of power. Finally, sputtering is a method based on the bombardment of a target for depositing thin layers. Using this method several layers were deposited which include oxides (SiO_2, TiO_2, NiO) or transparent conductive oxides (TCO) such as Indium tin oxide (ITO). The process involves a strike step were the plasma is started and a deposition step. Both steps are summarized in the figure A.1(c).

A.2 Materials

This session presents the materials employed in this thesis. The chemical structure is shown and also the optical properties (complex refractive index) of the thin films. Additionally some comments on the deposition method and recipes used are shown.

A.2.1 Active materials

The active layer in an organic photovoltaic device is based in two basic organic materials named donor and acceptor. This active layer can be structured as a planar (bilayer) or as a bulk (blend) heterojunction. The donor is the material that mainly absorbs light and where excitons are generated. Probably the most used one is poly(3-hexylthiophene) (P3HT). When excitons are created, they diffuse until reaching an interface with the acceptor material where they split into separeated charges. The most typically used acceptor material is phenyl-C61-butyric acid methyl ester (PCBM) which is a fullerene derivative. These Polymers were deposited by spincoating and next tables present the materials employed during the development of the current thesis.

Single donor layer: Poly(3-hexylthiophene) (P3HT)

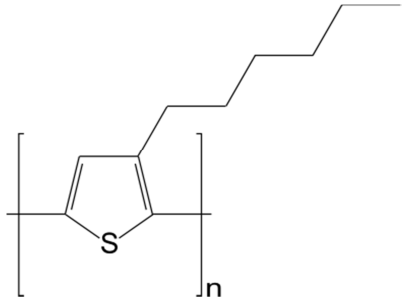

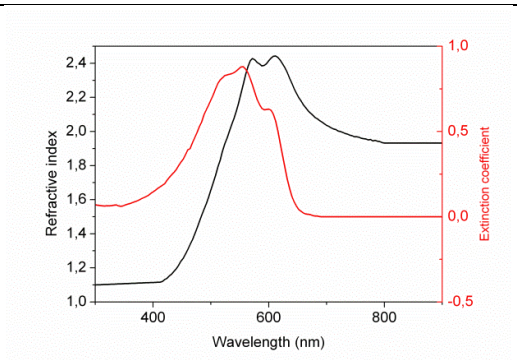

Deposition method: Spincoating

Deposition details: Chemical solution prepared a day before in Chlorobenzene or Dichlorobenzene and left stirring overnight under N_2 atmosphere with concentrations ranging from 5 to 30 mg/mL.

Recipe guide:

Ramp 1 (sec)	0
Speed 1 (rpm)	550
Dwell 1 (sec)	60
Ramp 2 (sec)	10
Speed 2 (rpm)	1000
Dwell 2 (sec)	70
Ramp 3 (sec)	0

For this P3HT single layer the thickness depends on the concentration according to T(nm)=6.5[P3HT]-20 where the [P3HT] is given in mg/mL

Single acceptor layer: Phenyl-C61-butyric acid methyl ester ($PC_{61}BM$)

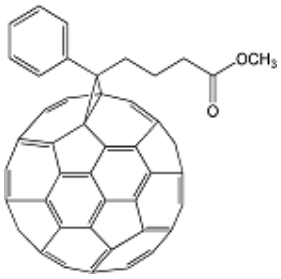

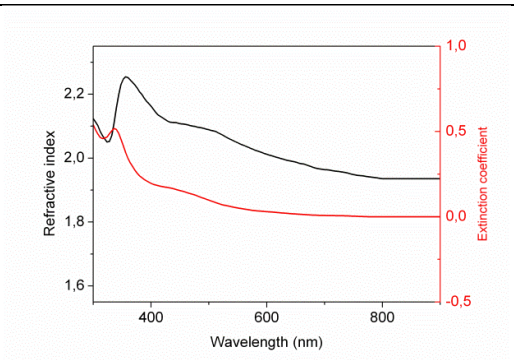

Deposition method: Spincoating

Deposition details: Chemical solution prepared a day before in Dichloromethane and left stirring overnight under N_2 atmosphere with concentrations 5 mg/mL.

Recipe guide:

Ramp 1 (sec)	0
Speed 1 (rpm)	4000
Dwell 1 (sec)	10
Ramp 2 (sec)	0
Speed 2 (rpm)	0
Dwell 2 (sec)	0
Ramp 3 (sec)	0

For this $PC_{61}BM$ single layer the thickness was around 20nm.

Single acceptor layer: Fullerene-C60

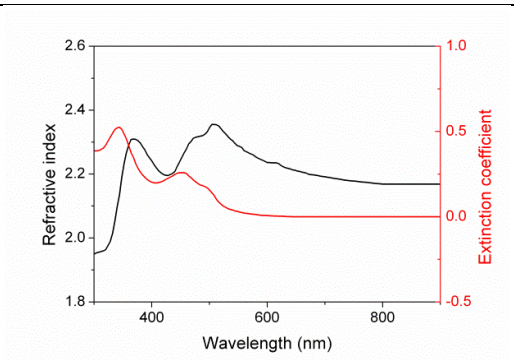

Deposition method: Thermal evaporation

Recipe guide:

Temperature (ºC)	440
Rate (Å/s)	1
Tooling factor (%)	16.2

Where the resulting thickness of the layer on top of was always kept thinner than 10nm.

Bulk-heterojunction:

Poly(3-hexylthiophene) (P3HT) : Phenyl-C61-butyric acid methyl ester ($PC_{61}BM$)

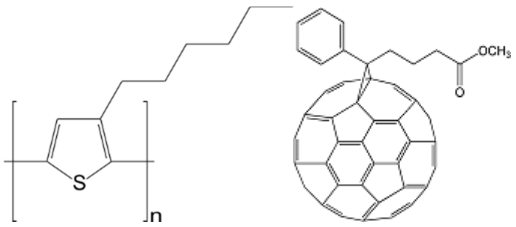

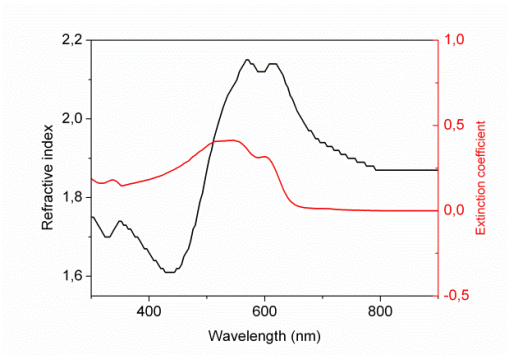

Deposition method: Spincoating

Deposition details: Chemical solution prepared a day before in Chlorobenzene or Dichlorobenzene and left stirring overnight under N_2 atmosphere with proportion 1:1 (wt) and 20 mg/mL of P3HT.

Recipe guide:

Ramp 1	Speed 1	Dwell 1	Ramp 2	Speed 2	Dwell 2	Ramp 3
0	500	60	10	S2	100	0

Ramp 1 (sec)	0
Speed 1 (rpm)	500
Dwell 1 (sec)	60
Ramp 2 (sec)	10
Speed 2 (rpm)	
Dwell 2 (sec)	100
Ramp 3 (sec)	0

Where the resulting thickness of the layer on top of PEDOT was given by

_____ and on top of TiO_2-np was given by _____

The devices including P3HT:$PC_{61}BM$ where treated with post-thermal annealing (150ºC during 1 min) when the devices were finished with aluminum.

Bulk-heterojunction:

Poly(3-hexylthiophene) (P3HT) :Indene-C60 bisadduct (ICBA)

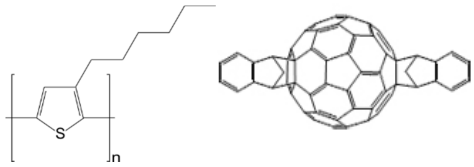

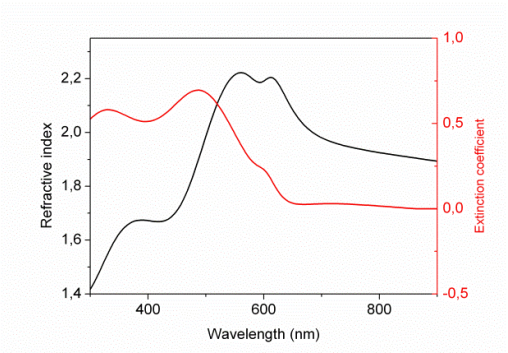

Deposition method: Spincoating

Deposition details: Chemical solution prepared a day before in Dichlorobenzene and left stirring overnight under N_2 atmosphere with proportion 1:1 (wt) and 17 mg/mL of P3HT.

Recipe guide:

Ramp 1 (sec)	0
Speed 1 (rpm)	550
Dwell 1 (sec)	60
Ramp 2 (sec)	10
Speed 2 (rpm)	950
Dwell 2 (sec)	120
Ramp 3 (sec)	0

Where the resulting thickness of the layer on top of TiO_2-np was around 120nm and the layer included a thermal annealing of 150ºC during 10 min in N_2 atmosphere.

Bulk-heterojunction:

Poly[4,8-bis-substituted-benzo[1,2-b:4,5-b0]dithiophene-2,6-diyl-alt-4-substituted-thieno[3, 4-b]thiophene-2,6-diyl] (PBDTTT) : [6,6]-phenyl C71 butyric acid methyl ester ($PC_{71}BM$)

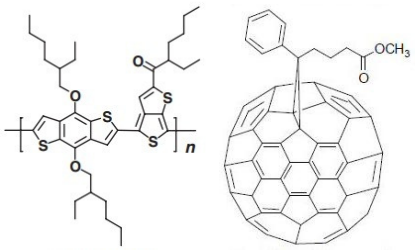

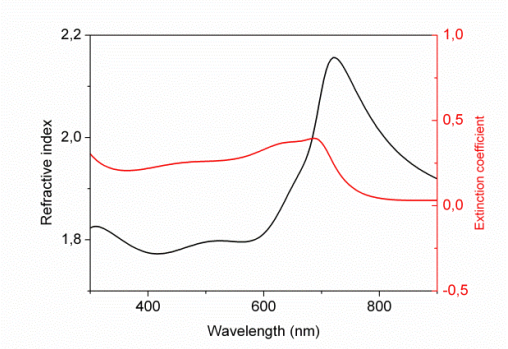

Deposition method: Spincoating

Deposition details: Chemical solution prepared a day before in Dichlorobenzene (97%) + 1,8-Diiodo-octane (3%) and left stirring overnight under N_2 atmosphere with proportion 1:1.5 (wt) and 10 mg/mL of PBDTTT.

Recipe guide:

Ramp 1 (sec)	1
Speed 1 (rpm)	800
Dwell 1 (sec)	120
Ramp 2 (sec)	0
Speed 2 (rpm)	0
Dwell 2 (sec)	0
Ramp 3 (sec)	0

After the spincoating, this layer was left 5 min slow drying, 5 min under soft vacuum and 20 min under high vacuum. Its resulting thickness on top of PEDOT or ZnO was around 100nm.

Bulk-heterojunction:

Poly[[4,8-bis[(2-ethylhexyl)oxy]benzo[1,2-b:4,5-b']dithiophene-2,6-diyl][3-fluoro-2-[(2-ethylhe-xyl)carbonyl]thieno[3,4-b]thiophenediyl]] (PTB7) : [6,6]-phenyl C71 butyric acid methyl ester ($PC_{71}BM$)

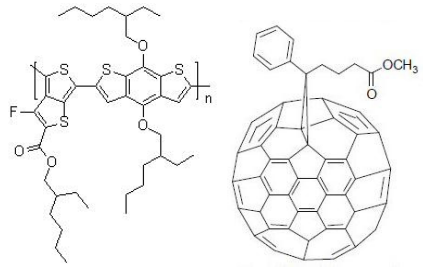

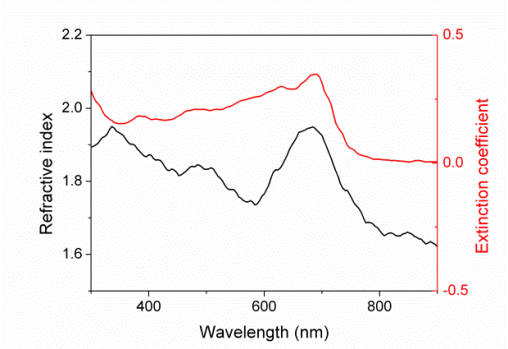

Deposition method: Spincoating

Deposition details: Chemical solution prepared a day before in chlorobenzene (97%) + 1,8-Diiodo-octane (3%) and left stirring overnight at 50ºC under N_2 atmosphere with proportion 1:1.5 (%wt) and 10 mg/mL of PTB7.

Recipe guide:

Ramp 1 (sec)	1
Speed 1 (rpm)	1800
Dwell 1 (sec)	60
Ramp 2 (sec)	0
Speed 2 (rpm)	0
Dwell 2 (sec)	0
Ramp 3 (sec)	0

Where the resulting thickness of the layer on top of PEDOT or ZnO was around 90nm.

A.2.2 Buffer layers

The electron transporting layers (ETLs) and hole transporting layers (HTLs) are placed in the interfaces of the active material and the electrodes in order to block excitons and either holes or electrons, respectively. These materials commonly present a very high energy bandgap and the ones employed in this thesis were:

Electron-transporting layers

<table>
<tr><td colspan="2">Titanium dioxide (TiO_2) (Anatase)</td></tr>
<tr><td>TiO_x</td><td> 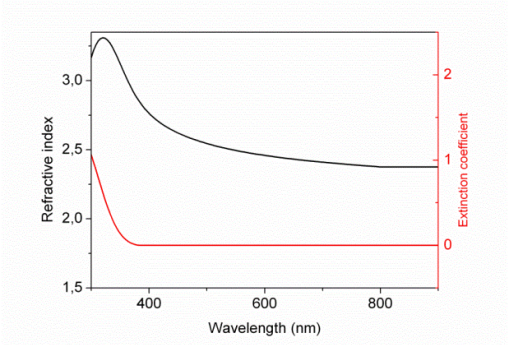
</td></tr>
<tr><td colspan="2">Deposition method: Spincoating (nanoparticles)

Nanoparticles synthesis:
Nanocrystalline TiO_2 particles were synthesized using a procedure previously reported and based on a sol-gel technique followed by growth under hydrothermal conditions[127]. This recipe was slightly modified in order to obtain a really fine particle size suspension (6 nm in average), which allowed forming very uniform TiO_2 films, and which have already been used to build highly reflectance structures in dye solar cells[128]. Concretely, titanium isopropoxide (20 ml, Aldrich 97%) was hydrolyzed after the addition to Milli-Q water (36 ml) and the stirring for 1 hour. Once this stage was completed, the product was filtered using 1.2 μm RTTP Millipore membranes, washed several times with distilled water and placed in a teflon reactor with 3.9 ml of 0.6 M tetramethylammonium hydroxide (~2.8M, Fluka). After homogeneizing the suspension with a stir bar, the reactor was placed in an oven preheated at 120º C, where it was kept for 3 hours. Peptization process took place during the heating in the presence of tetramethylammonium hydroxide. After</td></tr>
</table>

this, a bluish colloidal suspension of titanium oxide crystallites with anatase structure was obtained. Later centrifugation at 14.000 rpm for 10 minutes allowed eliminating some large aggregates from the dispersion.

Deposition details: Aqueous solutions of nanoparticles (~25% wt) were further diluted until concentrations ranging from 2 to 5% (wt) and in a mixture 80:20 of methanol:water (volume). The solution was spincoated in air. The fine particle size allowed to have very flat surfaces and in contrast to sputtered TiO_2, it did not require high temperature processing. This feature allows an optimal deposition on top of ITO and prevents indium diffusion and the consequent ITO degradation.

Recipe guide (3.5% wt):

Ramp 1	Speed 1	Dwell 1	Ramp 2	Speed 2	Dwell 2	Ramp 3
S1/10.000	S1	60	0	0	0	0

Ramp 1 (sec)	$S1/1000$
Speed 1 (rpm)	$S1$
Dwell 1 (sec)	60
Ramp 2 (sec)	0
Speed 2 (rpm)	0
Dwell 2 (sec)	0
Ramp 3 (sec)	0

The layer was treated with thermal annealing in a hotplate in air (125ºC during 10 min) and the resulting thickness of the layer on top of ITO was given by $T(nm) = 97 \cdot e^{\frac{-S1}{16949\,rpm}}$.

Zinc oxide (ZnO)

ZnO_x

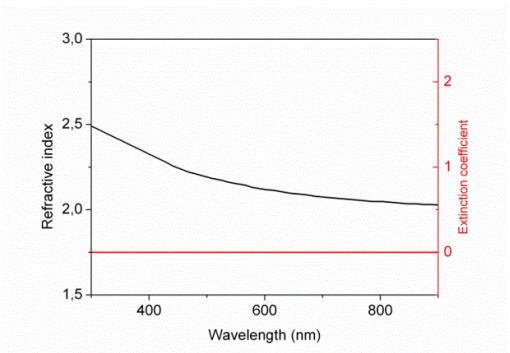

Deposition method: Spincoating (sol-gel)

Solution preparation: The sol-gel precursor was prepared following reference[57]. The solution was left stirring and applied by spincoating in ambient air

Recipe guide:

Ramp 1	Speed 1	Dwell 1	Ramp 2	Speed 2	Dwell 2	Ramp 3
0	6000	60	0	0	0	0

Ramp 1 (sec)	0
Speed 1 (rpm)	6000
Dwell 1 (sec)	60
Ramp 2 (sec)	0
Speed 2 (rpm)	0
Dwell 2 (sec)	0
Ramp 3 (sec)	0

The layer was further thermal annealed at 200ºC during 20 min in air and the resulting thickness of the layer on top of ITO was around 30nm.

Bathocuproine (BCP)

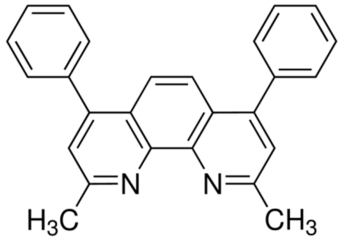

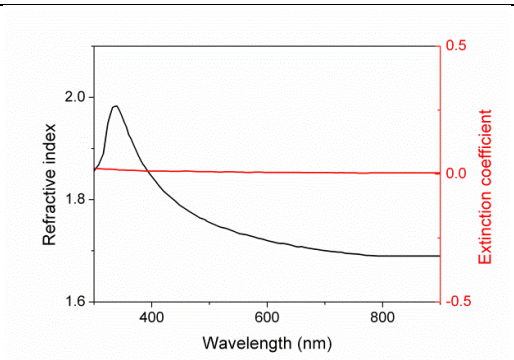

Deposition method: Thermal evaporation

Recipe guide:

Temperature (ºC)	135
Rate (Å/s)	0.5
Tooling factor (%)	12.8

Where the resulting thickness of the layer on top of was always kept thinner than 10nm.

Lithium fluoride (LiF)

LiF

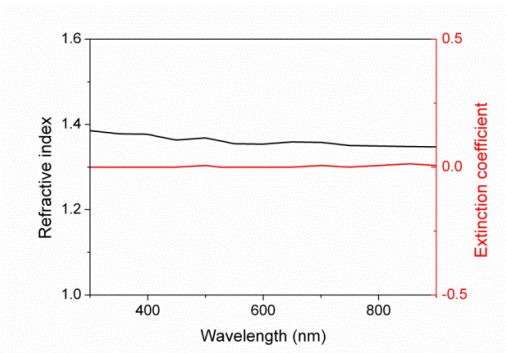

Deposition method: Thermal evaporation

Deposition details: Small pieces (crystals) were evaporated in alumina crucibles

Recipe guide:

Ramp 1 (sec)	140
Power 1 (%)	12
Soak time 1 (sec)	30
Ramp 2 (sec)	1
Power 2 (%)	8
Soak time 2 (sec)	100
Deposition Rate (Å/s)	1
Ramp 3 (sec)	30
Tooling factor (%)	44.5

Where the resulting thickness of the layer on top of was never thicker than 2 nm.

Lithium cobalt oxide ($LiCoO_2$)

Deposition method: Reactive sputtering

Deposition details: This layer was always developed on top of organic layers at room temperature.

Recipe guide:

Power strike (W)	40
Pressure strike (mTorr)	40
Ramp up (sec)	18
Deposition power (W)	70 RF
Deposition Pressure (mTorr)	2.5 [20 Ar : 10 O_2]
Deposition temperature (ºC)	RT
Height (cm)	30
Deposition Rate (Å/s)	0.075
Ramp down (sec)	42

Where the resulting thickness of the layer on top the organic layer was always kept below 1nm.

Hole-transporting layers

Molybdenum oxide (MoO_3)	
MoO_x	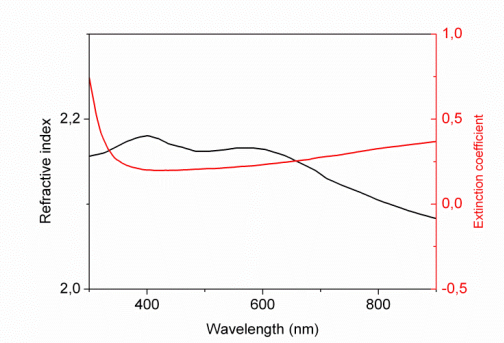

Deposition method: Thermal evaporation

Deposition details: Molybdenum oxide pieces were placed in alumina crucibles and thermally evaporated

Recipe guide:

Ramp 1 (sec)	60
Power 1 (%)	8.3
Soak time 1 (sec)	70
Ramp 2 (sec)	5
Power 2 (%)	6.6
Soak time 2 (sec)	200
Deposition Rate (Å/s)	1
Ramp 3 (sec)	30
Tooling factor (%)	53

Where the deposited thickness layer always ranged between 3 and 40 nm.

Poly(3,4-ethylenedioxythiophene) poly(styrenesulfonate) (PEDOT:PSS)

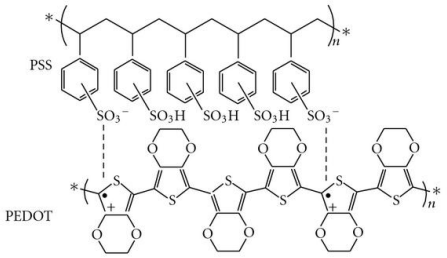

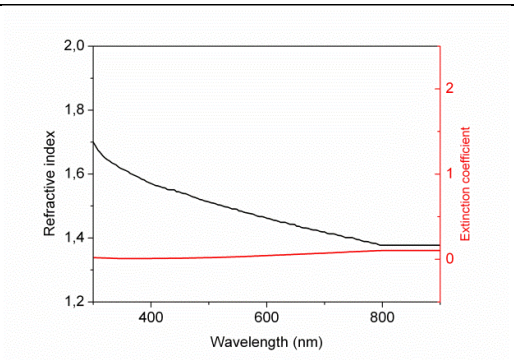

Deposition method: Spincoating

Deposition details: Solutions from Clevios (Al 4083) were filtered before deposition

Recipe guide:

Ramp 1 (sec)	5
Speed 1 (rpm)	$S1$
Dwell 1 (sec)	30
Ramp 2 (sec)	0
Speed 2 (rpm)	0
Dwell 2 (sec)	0
Ramp 3 (sec)	0

The typical thermal annealing was 125ºC during 10 min in a hotplate in air and the resulting thickness of the layer on top of ITO of was given by $T(nm) = 62 \cdot e^{\frac{-S1}{13210\,rpm}}$

Nickel oxide (NiO)

NiO_x

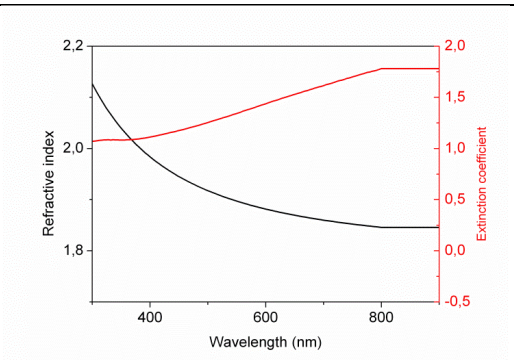

Deposition method: Sputtering

Deposition details: This hole transporting layer was always deposited on top of ITO

Recipe guide:

Power strike (W)	40
Pressure strike (mTorr)	40
Ramp up (sec)	36
Deposition power (W)	100 RF
Deposition Pressure (mTorr)	1.5 [20Ar-10O_2]
Deposition temperature (ºC)	RT
Height (cm)	30
Deposition Rate (Å/s)	0.09
Ramp down (sec)	60

After deposition, a plasma activation step (O_2 plasma) was required for enhancing the final V_{oc} of the devices. The minimum thickness of this layer on top of ITO was found to be 4.5nm.

A.2.3 Electrodes

Two different kinds of materials were used as electrodes, transparent conductive oxides (TCOs) concretely Indium tin oxide (ITO) and Aluminum doped zinc oxide (AZO) and common metal electrodes:

Indium tin oxide (ITO)

ITO

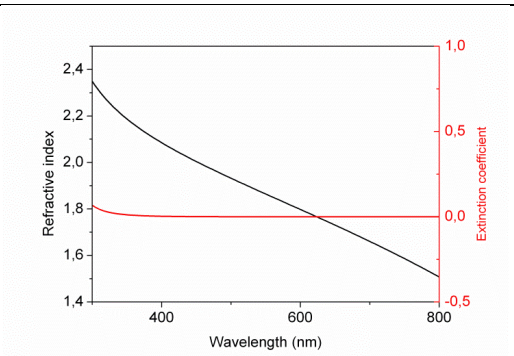

Deposition method: Reactive sputtering

Recipe guide:

Power strike (W)	40
Pressure strike (mTorr)	40
Ramp up (sec)	90
Deposition power (W)	70 DC
Deposition Pressure (mTorr)	2 [20 Ar : 10 O_2]
Deposition temperature (ºC)	100
Height (cm)	30
Deposition Rate (Å/s)	0.8
Ramp down (sec)	210

After the deposition, the ITO layer was thermal annealed at 300ºC in a hotplate in air during 5 min. The minimum thickness in order to have a good conductivity was around 110 nm.

Silver (Ag)

Ag

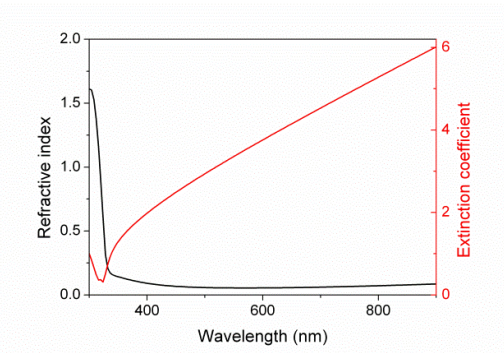

Deposition method: Thermal evaporation

Deposition details: Silver was found to be a very good electrode were no post-thermal annealing for the device was required. As a thin electrode was also very good and involved the use of low temperature substrate (~-5ºC) to avoid diffusion[18].

Recipe guide:

Ramp 1 (sec)	60
Power 1 (%)	12.8
Soak time 1 (sec)	190
Ramp 2 (sec)	33
Power 2 (%)	14.2
Soak time 2 (sec)	75
Deposition Rate (Å/s)	1
Ramp 3 (sec)	30
Tooling factor (%)	28

Aluminum (Al)

Al

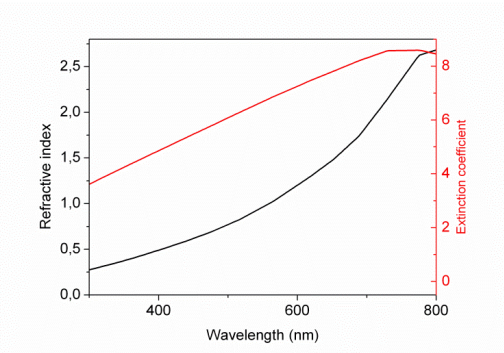

Deposition method: Thermal evaporation

Deposition details: Deposition rate was always kept close to 1Å/s to prevent boat damage.

Recipe guide:

Ramp 1 (sec)	60
Power 1 (%)	10
Soak time 1 (sec)	60
Ramp 2 (sec)	33
Power 2 (%)	13
Soak time 2 (sec)	60
Deposition Rate (Å/s)	1
Ramp 3 (sec)	30
Tooling factor (%)	69

Where the resulting thickness of the layer was typically over 100 nm.

Calcium (Ca)

Ag

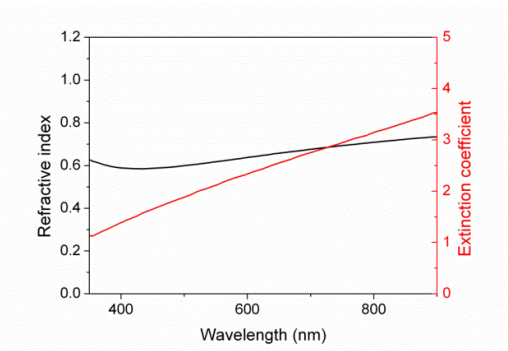

Deposition method: Thermal evaporation

Deposition details: This layer was used as an electrode and was always employed in the electron transporting layer interface in combination with aluminum or silver.

Recipe guide:

Ramp 1 (sec)	240
Power 1 (%)	6.5
Soak time 1 (sec)	160
Ramp 2 (sec)	60
Power 2 (%)	7
Soak time 2 (sec)	60
Deposition Rate (Å/s)	1
Ramp 3 (sec)	60
Tooling factor (%)	60

Where the resulting thickness of the layer on top of the organic was around 20 nm.

Gold (Au)

Au

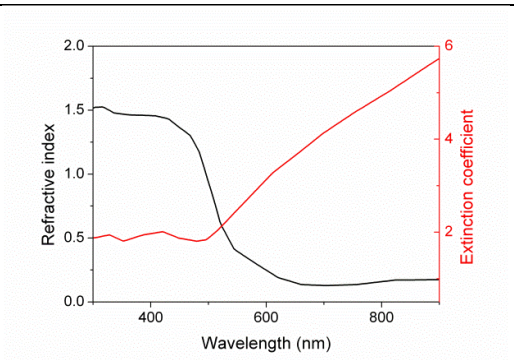

Deposition method: thermal evaporation

Recipe guide:

Ramp 1 (sec)	120
Power 1 (%)	10.5
Soak time 1 (sec)	80
Ramp 2 (sec)	120
Power 2 (%)	15
Soak time 2 (sec)	60
Deposition Rate (Å/s)	1
Ramp 3 (sec)	30
Tooling factor (%)	39

Cupper (Cu)

Cu

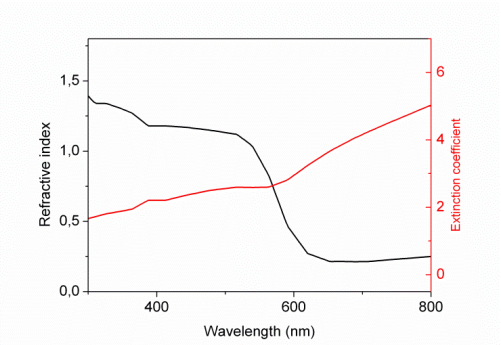

Deposition method: thermal evaporation

Recipe guide:

Power strike (W)	40
Pressure strike (mTorr)	40
Ramp up (sec)	12
Deposition power (W)	20 DC
Deposition Pressure (mTorr)	12
Deposition temperature (ºC)	RT
Height (cm)	30
Deposition Rate (Å/s)	0.131
Ramp down (sec)	12

The percolation limit was found to be around 7nm.

Nickel (Ni)

Ni

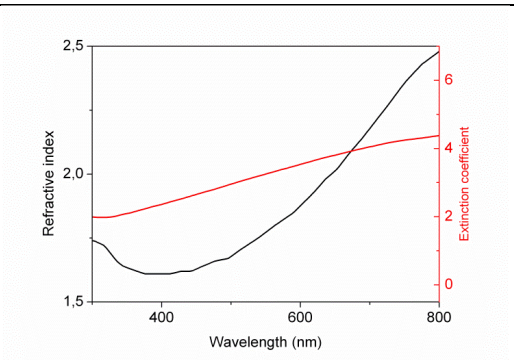

Deposition method: thermal evaporation

Recipe guide:

Power strike (W)	40 DC
Pressure strike (mTorr)	40
Ramp up (sec)	12
Deposition power (W)	20 DC
Deposition Pressure (mTorr)	3
Deposition temperature (ºC)	RT
Height (cm)	30
Deposition Rate (Å/s)	0.108
Ramp down (sec)	12

The percolation limit was found to be around 4 nm.

A.2.4 Other materials

SiO_2 was employed in combination with TiO_2 for growing 1-dimensional photonic crystals of few layers. The properties of TiO_2 and the following table summarizes the ones for SiO_2

Silicon oxide (SiO_2)

SiO_x

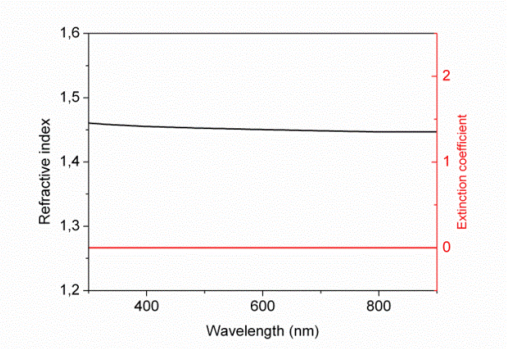

Deposition method: sputtering

Recipe guide:

Power strike (W)	40 RF
Pressure strike (mTorr)	40
Ramp up (sec)	360
Deposition power (W)	100 RF
Deposition Pressure (mTorr)	2
Deposition temperature (ºC)	RT
Height (cm)	30
Deposition Rate (Å/s)	0.14
Ramp down (sec)	360

Appendix B

Transparency and color transmitted by a STOPV device

B.1. Luminosity

The brightness of an object, as perceived by a human observer, is quantified by the luminosity L. It is also called "visible light transmission" (VLT) or "photopic transmission" and corresponds to the integrated transmission spectrum of an object or device $T(\lambda)$ over the whole visible spectrum, weighted by the photopic spectral response of a typical human eye $V(\lambda)$ and the spectrum of the illuminant. For daylight illumination, the CIE $D65(\lambda)$ is used as the illuminant. The spectrum of such illuminant, shown in figure B.1, is very close to black-body radiation with a color temperature of 6500K.

To calculate the luminosity of a solar device which in an application as a transparent window can be thought of as filter, one simply calculates the area under the transmission spectrum curve weighted by the Photopic Curve $V(\lambda)$, shown and the illuminant spectrum $I(\lambda)$ both in figure B.1, and normalize by the area under the

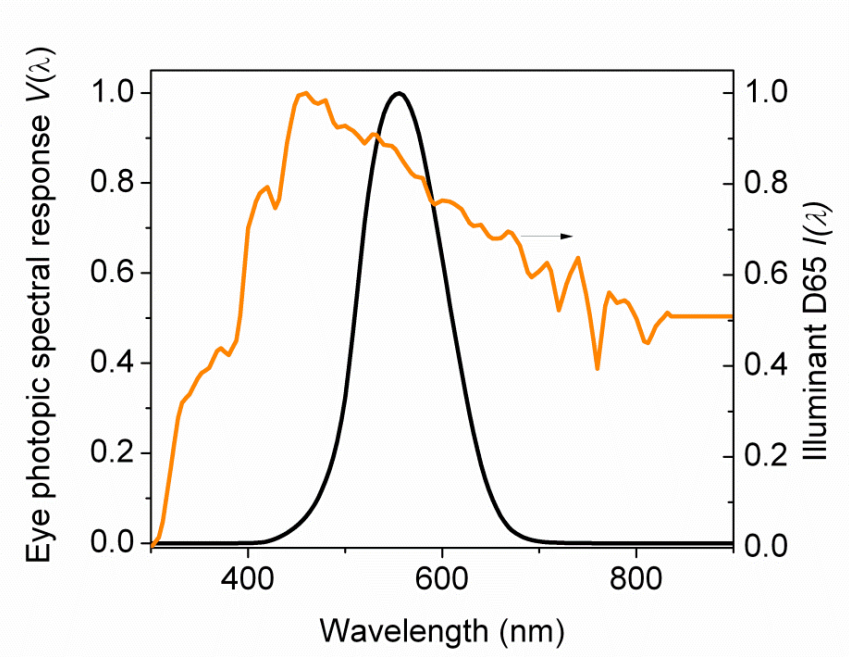

Figure B.1. Human eye and illumination information for the analyzed semi-transparent devices: Illuminant D65 (solid orange line) and human photopic spectral response (black line).

product of photopic curve and illuminant spectrum as in

$$L = \frac{\int T(\lambda)\, V(\lambda) D65(\lambda) d\lambda}{\int V(\lambda) D65(\lambda) d\lambda} \tag{B.1}$$

B.2 Estimation of the transmitted color

In general, the color calculation depends on three basic elements: the object (photovoltaic device in our case), the observer (human eye) and the illuminant (day light). In the numerical determination of the color, as observer and illuminant we used the CIE standards[126] while, the necessary object information is contained in the transmission spectrum $T(\lambda)$, which for the layered structure of our PV devices can be easily calculated using the transfer matrix formalism. From such transmission spectra

is possible to obtain the XYZ tristimulus values [126] according to the equations [126]

$$X = \int_{\lambda} \bar{x}\, T(\lambda) d\lambda \tag{B.2a}$$

$$Y = \int_{\lambda} \bar{y}\, T(\lambda) d\lambda \tag{B.2b}$$

$$Z = \int_{\lambda} \bar{z}\, T(\lambda) d\lambda \tag{B.2c}$$

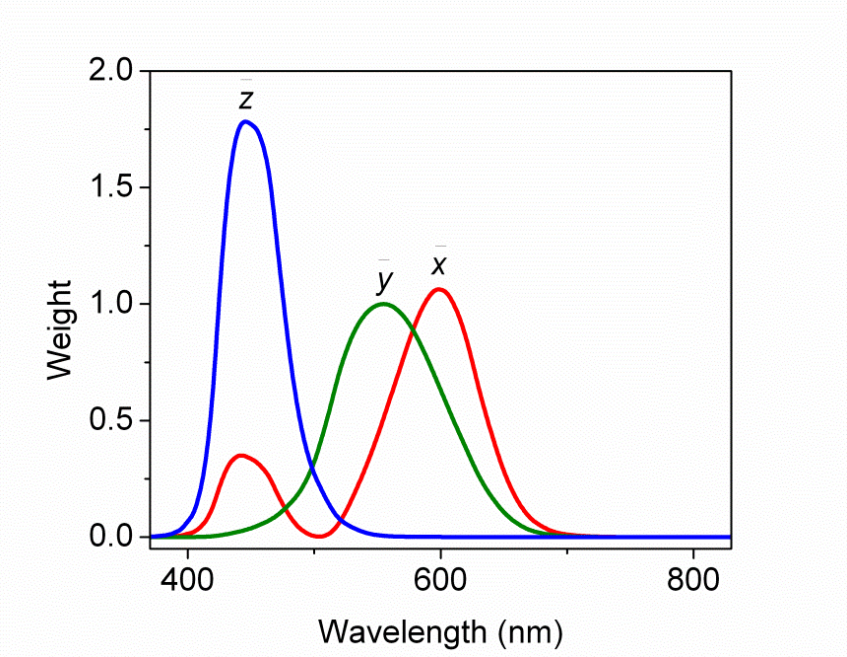

Figure B.2. CIE 1931 2º color matching functions[126].

Where $\bar{x}$, $\bar{y}$ and $\bar{z}$ correspond to the CIE standard observer functions, or the CIE 1931 2-deg color matching functions [126] shown in figure B.2. Then, one may determine the linear (r g b) parameters using

$$\begin{bmatrix} r \\ g \\ b \end{bmatrix} = M^{-1} \begin{bmatrix} X \\ Y \\ Z \end{bmatrix} \tag{B.3}$$

where M^{-1} is a transformation matrix associated to the working color space [126]. For the *Adobe RGB (1998)* color space [126] and when employing as illuminant the CIE-D65[126] this matrix becomes:

$$M^{-1} = \begin{bmatrix} 2.0413690 & -0.5649464 & -0.3446944 \\ -0.9692660 & 1.8760108 & 0.0415560 \\ 0.0134474 & -0.1183897 & 1.0154096 \end{bmatrix}$$

Finally, each coordinate r, g or b is transformed to the sRBG color space through the following compounding process

$$V = \begin{cases} 12.92v, & v \leq 0.0031308 \\ 1.055v^{1/2.4} - 0.055, & v > 0.0031308 \end{cases} \quad \text{(B.4)}$$

where v corresponds to the r, g, or b number obtained from Eq. (B.3). From the calculated $V = (R\ G\ B)$ and using Matlab software we obtained the corresponding color which we plotted in figure B.3 as a function of the calculated luminosity and short circuit current of the given device.

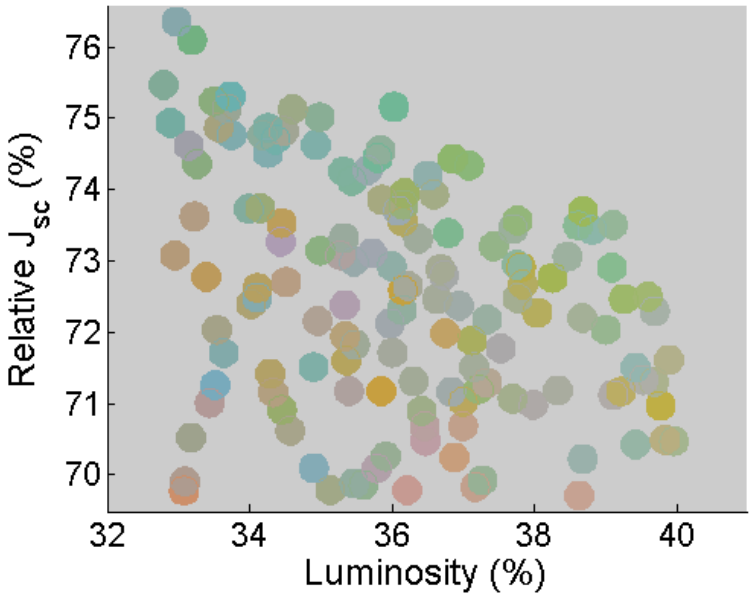

Figure B.3. Calculated transmitted colors of the semi-transparent PTB7:$PC_{71}BM$ PV devices that include a 5-layer photonic structure. The color is modified by changing the relative thicknesses of such five layers.

References

[1] British Petroleum, (2012).

[2] World Watch Institute (2012).

[3] National Renewable Energy Laboratory (2013).

[4] S. Lizin, S. Van Passel, E. De Schepper, L. Vranken, Solar Energy Materials and Solar Cells 103 (2012) 1.

[5] B. Petter Jelle, C. Breivik, H. Drolsum Røkenes, Solar Energy Materials and Solar Cells 100 (2012) 69.

[6] W. Cai, X. Gong, Y. Cao, Solar Energy Materials and Solar Cells 94 (2010) 114.

[7] L. El Chaar, L. a. Lamont, N. El Zein, Renewable and Sustainable Energy Reviews 15 (2011) 2165.

[8] D. Schrag, Scientific American (2008).

[9] M.K. Riede, Universität Konstanz Doctoral Thesis 1 (2006) 228.

[10] K. Petritsch, Technische Universitat Graz Austria Doctoral Thesis 1 (2000) 159.

[11] J.-L. Wu, F.-C. Chen, Y.-S. Hsiao, F.-C. Chien, P. Chen, C.-H. Kuo, M.H. Huang, C.-S. Hsu, ACS Nano 5 (2011) 959.

[12] R.R. Lunt, N.C. Giebink, A. a. Belak, J.B. Benziger, S.R. Forrest, Journal of Applied Physics 105 (2009) 053711.

[13] L. Huo, S. Zhang, X. Guo, F. Xu, Y. Li, J. Hou, Angewandte Chemie (International Ed. in English) 50 (2011) 9697.

[14] Z. He, C. Zhong, X. Huang, W.-Y. Wong, H. Wu, L. Chen, S. Su, Y. Cao, Advanced Materials (Deerfield Beach, Fla.) 23 (2011) 4636.

[15] Y. Liang, Z. Xu, J. Xia, S.-T. Tsai, Y. Wu, G. Li, C. Ray, L. Yu, Advanced Materials 22 (2010) E135.

[16] M. Reyes-reyes, I. Cruz-cruz, D. San, L. Potosı, (2010) 20220.

[17] C. Tao, S. Ruan, G. Xie, X. Kong, L. Shen, F. Meng, C. Liu, X. Zhang, W. Dong, W. Chen, Applied Physics Letters 94 (2009) 043311.

[18] N.P. Sergeant, A. Hadipour, B. Niesen, D. Cheyns, P. Heremans, P. Peumans, B.P. Rand, Advanced Materials 24 (2012) 728.

[19] R. Betancur, A. Martínez-Otero, X. Elias, P. Romero-Gómez, S. Colodrero, H. Miguez, J. Martorell, Solar Energy Materials and Solar Cells 104 (2012) 87.

[20] M.D. Irwin, D.B. Buchholz, A.W. Hains, R.P.H. Chang, T.J. Marks, (2007) 2.

[21] R. Betancur, M. Maymó, X. Elias, L.T. Vuong, J. Martorell, Solar Energy Materials and Solar Cells 95 (2011) 735.

[22] B.E. Lassiter, G. Wei, S. Wang, J.D. Zimmerman, V.V. Diev, M.E. Thompson, S.R. Forrest, Applied Physics Letters 98 (2011) 243307.

[23] C.J. Brabec, S.E. Shaheen, C. Winder, N.S. Sariciftci, P. Denk, Applied Physics Letters 80 (2002) 1288.

[24] K.-S. Liao, S.D. Yambem, A. Haldar, N.J. Alley, S. a. Curran, Energies 3 (2010) 1212.

[25] T.L. Chen, R. Betancur, D.S. Ghosh, J. Martorell, V. Pruneri, Applied Physics Letters 100 (2012) 013310.

[26] D.S. Ghosh, R. Betancur, T.L. Chen, V. Pruneri, J. Martorell, Solar Energy Materials and Solar Cells 95 (2011) 1228.

[27] M.-G. Kang, T. Xu, H.J. Park, X. Luo, L.J. Guo, Advanced Materials (Deerfield Beach, Fla.) 22 (2010) 4378.

[28] M.W. Rowell, M. a. Topinka, M.D. McGehee, H.-J. Prall, G. Dennler, N.S. Sariciftci, L. Hu, G. Gruner, Applied Physics Letters 88 (2006) 233506.

[29] H. Park, J. a Rowehl, K.K. Kim, V. Bulovic, J. Kong, Nanotechnology 21 (2010) 505204.

[30] Y. Yuan, J. Huang, G. Li, S. Energy, E. Monte, Green 1 (2011) 65.

[31] A.J. Medford, M.R. Lilliedal, M. Jørgensen, D. Aarø, H. Pakalski, J. Fyenbo, F.C. Krebs, Optics Express 18 Suppl 3 (2010) A272.

[32] F.C. Krebs, T. Tromholt, M. Jørgensen, Nanoscale 2 (2010) 873.

[33] F.C. Krebs, T.D. Nielsen, J. Fyenbo, M. Wadstrøm, M.S. Pedersen, Energy & Environmental Science 3 (2010) 512.

[34] F.C. Krebs, J. Fyenbo, M. Jørgensen, Journal of Materials Chemistry 20 (2010) 8994.

[35] F.C. Krebs, S. a. Gevorgyan, J. Alstrup, Journal of Materials Chemistry 19 (2009) 5442.

[36] F.C. Krebs, S. a. Gevorgyan, B. Gholamkhass, S. Holdcroft, C. Schlenker, M.E. Thompson, B.C. Thompson, D. Olson, D.S. Ginley, S.E. Shaheen, H.N. Alshareef, J.W. Murphy, W.J. Youngblood, N.C. Heston, J.R. Reynolds, S. Jia, D. Laird, S.M. Tuladhar, J.G. a. Dane, P. Atienzar, J. Nelson, J.M. Kroon, M.M. Wienk, R. a. J. Janssen, K. Tvingstedt, F. Zhang, M. Andersson, O. Inganäs, M. Lira-Cantu, R. de Bettignies, S. Guillerez, T. Aernouts, D. Cheyns, L. Lutsen, B. Zimmermann, U. Würfel, M. Niggemann, H.-F. Schleiermacher, P. Liska, M. Grätzel, P. Lianos, E. a. Katz, W. Lohwasser, B. Jannon, Solar Energy Materials and Solar Cells 93 (2009) 1968.

[37] K. Kawano, R. Pacios, D. Poplavskyy, J. Nelson, D.D.C. Bradley, J.R. Durrant, Solar Energy Materials and Solar Cells 90 (2006) 3520.

[38] K. Norrman, S. a Gevorgyan, F.C. Krebs, ACS Applied Materials & Interfaces 1 (2009) 102.

[39] M. Jørgensen, K. Norrman, F.C. Krebs, Solar Energy Materials and Solar Cells 92 (2008) 686.

[40] J. Hou, H.-Y. Chen, S. Zhang, R.I. Chen, Y. Yang, Y. Wu, G. Li, Journal of the American Chemical Society 131 (2009) 15586.

[41] Z.T. Liu, C.Y. Kwong, C.H. Cheung, a. B. Djurišić, Y. Chan, P.C. Chui, Synthetic Metals 150 (2005) 159.

[42] K.S. Nalwa, J.-M. Park, K.-M. Ho, S. Chaudhary, Advanced Materials 23 (2011) 112.

[43] Z.M. Beiley, E.T. Hoke, R. Noriega, J. Dacuña, G.F. Burkhard, J. a. Bartelt, A. Salleo, M.F. Toney, M.D. McGehee, Advanced Energy Materials 1 (2011) 954.

[44] G.D. Spyropoulos, M. Stylianakis, E. Stratakis, E. Kymakis, Photonics and Nanostructures - Fundamentals and Applications 9 (2011) 184.

[45] D.H. Wang, K.H. Park, J.H. Seo, J. Seifter, J.H. Jeon, J.K. Kim, J.H. Park, O.O. Park, A.J. Heeger, Advanced Energy Materials 1 (2011) 766.

[46] M. Born, E. Wolf, Principles of Optics: Electromagnetic Theory of Propagation, Interference and Diffraction of Light, 1964.

[47] J.D. Jackson, Classical Electrodynamics, 1998.

[48] A.J. Moulé, K. Meerholz, Applied Physics B 86 (2006) 721.

[49] P.D. Andersen, J.C. Skårhøj, J.W. Andreasen, F.C. Krebs, Optical Materials 31 (2009) 1007.

[50] A. Roy, S.H. Park, S. Cowan, M.H. Tong, S. Cho, K. Lee, A.J. Heeger, Applied Physics Letters 95 (2009) 013302.

[51] B.V. Andersson, D.M. Huang, A.J. Moulé, O. Inganäs, Applied Physics Letters 94 (2009) 043302.

[52] A.J. Moulé, J.B. Bonekamp, K. Meerholz, Journal of Applied Physics 100 (2006) 094503.

[53] E.. Taft, Philipp H.R., Physical Review 121 (1961) 1100.

[54] P.P. Boix, J. Ajuria, I. Etxebarria, R. Pacios, G. Garcia-Belmonte, J. Bisquert, The Journal of Physical Chemistry Letters 2 (2011) 407.

[55] A.K. Ghosh, T. Feng, Journal of Applied Physics 49 (1978) 5982.

[56] N. Blouin, a. Michaud, M. Leclerc, Advanced Materials 19 (2007) 2295.

[57] Y. Sun, J.H. Seo, C.J. Takacs, J. Seifter, A.J. Heeger, Advanced Materials (Deerfield Beach, Fla.) 23 (2011) 1679.

[58] M. Helgesen, R. Søndergaard, F.C. Krebs, Journal of Materials Chemistry 20 (2010) 36.

[59] A. Martinez-Otero, X. Elias, R. Betancur, J. Martorell, Adv. Optical Mater 1 (2012) 37.

[60] Z. Chen, F. Ding, F. Hao, Z. Bian, B. Ding, Y. Zhu, F. Chen, C. Huang, Organic Electronics 10 (2009) 939.

[61] C.-J. Huang, J.-C. Ke, W.-R. Chen, T.-H. Meen, C.-F. Yang, Solar Energy Materials and Solar Cells 95 (2011) 3460.

[62] T.-Y. Chu, J. Lu, S. Beaupré, Y. Zhang, J.-R. Pouliot, S. Wakim, J. Zhou, M. Leclerc, Z. Li, J. Ding, Y. Tao, Journal of the American Chemical Society 133 (2011) 4250.

[63] G.H. Jung, K. Hong, W.J. Dong, S. Kim, J.-L. Lee, Advanced Energy Materials 1 (2011) 1023.

[64] T.-Y. Chu, J. Lu, S. Beaupré, Y. Zhang, J.-R. Pouliot, J. Zhou, A. Najari, M. Leclerc, Y. Tao, Advanced Functional Materials 22 (2012) 2345.

[65] S.J. Lou, J.M. Szarko, T. Xu, L. Yu, T.J. Marks, L.X. Chen, Journal of the American Chemical Society 133 (2011) 20661.

[66] H. Chen, J. Hou, S. Zhang, Y. Liang, G. Yang, Nature … 3 (2009) 649.

[67] A. Martínez-Otero, F. Busqué, J. Hernando, D. Ruiz-Molina, Nanoscale 2 (2010) 1781.

[68] Z. Tan, W. Zhang, Z. Zhang, D. Qian, Y. Huang, J. Hou, Y. Li, Advanced Materials (Deerfield Beach, Fla.) 24 (2012) 1476.

[69] Y. Zhou, C. Fuentes-Hernandez, J. Shim, J. Meyer, A.J. Giordano, H. Li, P. Winget, T. Papadopoulos, H. Cheun, J. Kim, M. Fenoll, A. Dindar, W. Haske, E. Najafabadi, T.M. Khan, H. Sojoudi, S. Barlow, S. Graham, J.-L. Brédas, S.R. Marder, A. Kahn, B. Kippelen, Science (New York, N.Y.) 336 (2012) 327.

[70] C.E. Small, S. Chen, J. Subbiah, C.M. Amb, S. Tsang, T. Lai, J.R. Reynolds, F. So, 6 (2011).

[71] S.-Y. Park, H.-R. Kim, Y.-J. Kang, D.-H. Kim, J.-W. Kang, Solar Energy Materials and Solar Cells 94 (2010) 2332.

[72] Y.-M. Chang, L. Wang, W.-F. Su, Organic Electronics 9 (2008) 968.

[73] H.-L. Chen, Y.-M. Lu, W.-S. Hwang, Surface and Coatings Technology 198 (2005) 138.

[74] a. Hakim, J. Hossain, K. a. Khan, Renewable Energy 34 (2009) 2625.

[75] J. Zhou, Indium Tin Oxide (ITO) Depositions, Patterning and Schottky Contact Fabrication,, 2005.

[76] D.S. Ghosh, L. Martinez, S. Giurgola, P. Vergani, V. Pruneri, Optics Letters 34 (2009) 325.

[77] D.S. Ghosh, T.L. Chen, V. Pruneri, Applied Physics Letters 96 (2010) 041109.

[78] B. O'Connor, K.H. An, K.P. Pipe, Y. Zhao, M. Shtein, Applied Physics Letters 89 (2006) 233502.

[79] N. Takada, T. Tsutsui, S. Saito, Applied Physics Letters 63 (1993) 2032.

[80] R.F. Bailey-Salzman, B.P. Rand, S.R. Forrest, Applied Physics Letters 88 (2006) 233502.

[81] G.-M. Ng, E.L. Kietzke, T. Kietzke, L.-W. Tan, P.-K. Liew, F. Zhu, Applied Physics Letters 90 (2007) 103505.

[82] F.-C. Chen, J.-L. Wu, K.-H. Hsieh, W.-C. Chen, S.-W. Lee, Organic Electronics 9 (2008) 1132.

[83] J. Huang, G. Li, Y. Yang, Advanced Materials 20 (2008) 415.

[84] R. Koeppe, D. Hoeglinger, P.A. Troshin, R.N. Lyubovskaya, V.F. Razumov, N.S. Sariciftci, ChemSusChem 2 (2009) 309.

[85] J. Meiss, K. Leo, M.K. Riede, C. Uhrich, W.-M. Gnehr, S. Sonntag, M. Pfeiffer, Applied Physics Letters 95 (2009) 213306.

[86] S. Tanaka, a. a. Zakhidov, R. Ovalle-Robles, Y. Yoshida, I. Hiromitsu, Y. Fujita, K. Yoshino, Synthetic Metals 159 (2009) 2326.

[87] A. (Celik) Bedeloglu, A. Demir, Y. Bozkurt, N.S. Sariciftci, Renewable Energy 35 (2010) 2301.

[88] T. Ameri, G. Dennler, C. Waldauf, H. Azimi, A. Seemann, K. Forberich, J. Hauch, M. Scharber, K. Hingerl, C.J. Brabec, Advanced Functional Materials 20 (2010) 1592.

[89] Q. Dong, Y. Zhou, J. Pei, Z. Liu, Y. Li, S. Yao, J. Zhang, W. Tian, Organic Electronics 11 (2010) 1327.

[90] J.-Y. Lee, S.T. Connor, Y. Cui, P. Peumans, Nano Letters 10 (2010) 1276.

[91] F. Nickel, A. Puetz, M. Reinhard, H. Do, C. Kayser, A. Colsmann, U. Lemmer, Organic Electronics 11 (2010) 535.

[92] A.K. Pandey, I.D.W. Samuel, IEEE Journal of Selected Topics in Quantum Electronics 16 (2010) 1560.

[93] Y. Zhou, H. Cheun, S. Choi, W.J. Potscavage, C. Fuentes-Hernandez, B. Kippelen, Applied Physics Letters 97 (2010) 153304.

[94] A. Colsmann, A. Puetz, A. Bauer, J. Hanisch, E. Ahlswede, U. Lemmer, Advanced Energy Materials 1 (2011) 599.

[95] Y.-Y. Lee, K.-H. Tu, C.-C. Yu, S.-S. Li, J.-Y. Hwang, C.-C. Lin, K.-H. Chen, L.-C. Chen, H.-L. Chen, C.-W. Chen, ACS Nano 5 (2011) 6564.

[96] J.E. Lewis, E. Lafalce, P. Toglia, X. Jiang, Solar Energy Materials and Solar Cells 95 (2011) 2816.

[97] J. Meiss, F. Holzmueller, R. Gresser, K. Leo, M. Riede, Applied Physics Letters 99 (2011) 193307.

[98] R.J. Peh, Y. Lu, F. Zhao, C.-L.K. Lee, W.L. Kwan, Solar Energy Materials and Solar Cells 95 (2011) 3579.

[99] A. Bauer, T. Wahl, J. Hanisch, E. Ahlswede, Applied Physics Letters 100 (2012) 073307.

[100] A. Colsmann, M. Reinhard, T.-H. Kwon, C. Kayser, F. Nickel, J. Czolk, U. Lemmer, N. Clark, J. Jasieniak, A.B. Holmes, D. Jones, Solar Energy Materials and Solar Cells 98 (2012) 118.

[101] J.-W. Kang, Y.-J. Kang, S. Jung, D.S. You, M. Song, C.S. Kim, D.-G. Kim, J.-K. Kim, S.H. Kim, Organic Electronics 13 (2012) 2940.

[102] H. Schmidt, H. Flügge, T. Winkler, T. Bülow, T. Riedl, W. Kowalsky, Applied Physics Letters 94 (2009) 243302.

[103] X. Wang, G.-M. Ng, J.-W. Ho, H.-L. Tam, F. Zhu, IEEE Journal of Selected Topics in Quantum Electronics 16 (2010) 1685.

[104] Y.H. Kim, L. Müller-Meskamp, A. a. Zakhidov, C. Sachse, J. Meiss, J. Bikova, A. Cook, A. a. Zakhidov, K. Leo, Solar Energy Materials and Solar Cells 96 (2012) 244.

[105] Z. Tang, Z. George, Z. Ma, J. Bergqvist, K. Tvingstedt, K. Vandewal, E. Wang, L.M. Andersson, M.R. Andersson, F. Zhang, O. Inganäs, Advanced Energy Materials (2012) n/a.

[106] H.P. Kim, H.J. Lee, A.R.B. Mohd Yusoff, J. Jang, Solar Energy Materials and Solar Cells 108 (2013) 38.

[107] C. Tuchinda, S. Srivannaboon, H.W. Lim, J. Am. Acad. Dermatol. 54 (2006) 845.

[108] L. Shen, Y. Xu, F. Meng, F. Li, S. Ruan, W. Chen, Organic Electronics 12 (2011) 1223.

[109] C. Tao, G. Xie, C. Liu, X. Zhang, W. Dong, F. Meng, X. Kong, L. Shen, S. Ruan, W. Chen, Applied Physics Letters 95 (2009) 053303.

[110] T. Winkler, H. Schmidt, H. Flügge, F. Nikolayzik, I. Baumann, S. Schmale, T. Weimann, P. Hinze, H.-H. Johannes, T. Rabe, S. Hamwi, T. Riedl, W. Kowalsky, Organic Electronics 12 (2011) 1612.

[111] C. Tao, G. Xie, F. Meng, S. Ruan, W. Chen, The Journal of Physical Chemistry C 115 (2011) 12611.

[112] H. Jin, C. Tao, M. Velusamy, M. Aljada, Y. Zhang, M. Hambsch, P.L. Burn, P. Meredith, Advanced Materials 24 (2012) 2572.

[113] Z. Liu, J. Li, Z.-H. Sun, G. Tai, S.-P. Lau, F. Yan, ACS Nano 6 (2012) 810.

[114] R.R. Lunt, V. Bulovic, Applied Physics Letters 98 (2011) 113305.

[115] Y. Galagan, M.G. Debije, P.W.M. Blom, Applied Physics Letters 98 (2011) 043302.

[116] C. Chen, L. Dou, R. Zhu, C. Chung, T. Song, Y.B. Zheng, S. Hawks, G. Li, P. Weiss, Y. Yang, Journal of the American Chemical Society 6 (2012) 7185.

[117] L. Dou, W.-H. Chang, J. Gao, C.-C. Chen, J. You, Y. Yang, Advanced Materials (2012) n/a.

[118] J. Meiss, T. Menke, K. Leo, C. Uhrich, W.-M. Gnehr, S. Sonntag, M. Pfeiffer, M. Riede, Applied Physics Letters 99 (2011) 043301.

[119] K.-S. Chen, J.-F. Salinas, H.-L. Yip, L. Huo, J. Hou, A.K.-Y. Jen, Energy Environ. Sci 5 (2012) 9551.

[120] C.-C. Chueh, S.-C. Chien, H.-L. Yip, J.F. Salinas, C.-Z. Li, K.-S. Chen, F.-C. Chen, W.-C. Chen, A.K.-Y. Jen, Advanced Energy Materials (2012) n/a.

[121] R.R. Lunt, Applied Physics Letters 101 (2012) 043902.

[122] Z. He, C. Zhong, S. Su, M. Xu, H. Wu, Y. Cao, 6 (2012) 591.

[123] P. Bermel, M. Ghebrebrhan, W. Chan, Y.X. Yeng, M. Araghchini, R. Hamam, C.H. Marton, K.F. Jensen, M. Soljačić, J.D. Joannopoulos, S.G. Johnson, I. Celanovic, Optics Express 18 Suppl 3 (2010) A314.

[124] A. Donges, European Journal of Physics 19 (1998) 245.

[125] H. Hoppe, N. Arnold, N.S. Sariciftci, D. Meissner, Solar Energy Materials and Solar Cells 80 (2003) 105.

[126] Commission Internationale De L'eclairaige. (2013).

[127] S.D. Burnside, V. Shklover, C. Barbe, P. Comte, F. Arendse, K. Brooks, M. Gra, 255 (1998) 2419.

[128] S. Colodrero, A. Mihi, L. Häggman, M. Ocaña, G. Boschloo, A. Hagfeldt, H. Míguez, Advanced Materials 21 (2009) 764.